

# Optical analysis of c-Si quantum dots embedded in a silica matrix

For solar cells application

Adele Fusi

Master of Science Thesis



# Optical analysis of c-Si quantum dots embedded in a silica matrix

For solar cells application

MASTER OF SCIENCE THESIS

For the degree of Master of Science in Sustainable Energy Technology  
at Delft University of Technology

Adele Fusi

26 August 2015

Supervisors

Dr. R.A.C.M.M. van Swaaij  
M. van Sebille

Examination Committee

prof. dr. M. Zeman  
Dr. R.A.C.M.M. van Swaaij  
M. van Sebille  
dr. L. van Eijck

Faculty of Applied Science · Delft University of Technology



---

# Abstract

Silicon quantum dot (QD) solar cells are considered a promising innovation, in PV applications, for the reduction of conversion efficiency losses attributed to spectral mismatch. The optical properties of QDs strongly depend on their size, while the density of QDs and their spacing within a layer determine the electrical properties of the material. For these reasons, the accurate control of such characteristics is crucial in the optimization of the QD fabrication process.

In this work the evolution of c-Si QDs embedded in a silica matrix was investigated as a function of different process parameters. By applying a method [1] which separates the contribution of quantum dots (QDs) from the surrounding dielectric matrix in absorption coefficient spectra, it was possible to extract several properties of the QDs. The parameters we analyzed in this work are the density of QDs states, the QDs energy band gap and its standard deviation, which is a measure of the QDs size dispersion. The characterization of our layers was based on the above-mentioned parameters, together with Raman spectroscopy and the absorption coefficient in defect related spectral range. QDs were successfully fabricated by high temperature annealing and subsequent Si precipitation from Si-rich layers of PECVD deposited  $\alpha$ -SiO<sub>x</sub>/SiO<sub>2</sub> superlattice samples. Annealing in a conventional furnace resulted in the growth of a thick thermal oxide top layer. It was possible to avoid it by using a rapid thermal annealing furnace, which also resulted in samples with a lower defect density. An increasing Si content of the Si-rich layers showed to lead to higher crystallinity and lower defect density of the material. The QDs formed in forming gas atmosphere started shrinking after a threshold annealing time. For annealing time longer than 3-3.5 min, in fact, the crystallinity and density of QDs states start decreasing. The QD size distribution broadens and the energy band gap increases. These results indicate a decrease in mean QDs size, a phenomenon for which we proposed two different explanations. We fabricated more stable QDs by using nitrogen gas annealing atmosphere in the same furnace. In this case saturation in crystallinity was reached, after approximately 2 min annealing. During crystallization the QDs energy band gap decreased from 2.4 to 1.85 eV, the standard deviation dropped from 0.21 to about 0.08 eV, showing an increasingly narrower size distribution. These results indicate a strong dependence of QDs evolution on annealing time during the crystallization step. This dependence ceases after saturation is reached. The increase in crystallinity is attributed to

the increase in mean QD size, as the size distribution becomes increasingly narrow, meaning that a larger portion of QDs reaches the maximum size imposed by the structure. Upon crystallization, annealing in forming gas led to a remarkably lower defect related absorption ( $736\text{ cm}^{-1}$  on average, at  $1.5\text{ eV}$ ) than annealing in nitrogen gas ( $1026\text{ cm}^{-1}$ ).

The evolution of QDs properties was also studied for different thicknesses of Si-rich layer (2, 3, 4 and 5 nm), at different annealing temperatures and durations. The crystallization process showed a strong dependence on the Si-rich layer thickness. Thinner layers crystallized at higher temperature, showed longer incubation time and, generally, reached lower crystallinity. At comparable stages of crystallization, larger QD energy band gap (from 1.8 to 2 eV) and decreasing standard deviation (from 0.12 to 0.06 eV) were found for increasingly thinner Si-rich layers.

---

# Table of Contents

|   |           |
|---|-----------|
| <b>Acknowledgements</b>   | <b>xi</b> |
| <b>1 Introduction</b>   | <b>1</b>  |
| 1.1 Solar energy . . . . .  | 1         |
| 1.2 Photovoltaic technologies . . . . .                           | 2         |
| 1.3 Motivation . . . . .  | 4         |
| 1.4 Research goals & objectives . . . . .                         | 6         |
| 1.5 Outline of MSc Thesis . . . . .                               | 7         |
| <b>2 Theoretical background</b>                                   | <b>9</b>  |
| 2.1 Basics of quantum mechanics and quantum confinement . . . . . | 9         |
| 2.1.1 Infinite potential well . . . . .                           | 10        |
| 2.1.2 Potential barrier . . . . .                                 | 12        |
| 2.1.3 Quantum confinement in QDs superlattices . . . . .          | 12        |
| 2.1.4 Quantum confinement & Phase separation . . . . .            | 14        |
| 2.2 Crystallization theory . . . . .                              | 15        |
| 2.2.1 Annealing induced defects . . . . .                         | 16        |
| <b>3 Experimental procedures and setups</b>                       | <b>19</b> |
| 3.1 Sample fabrication . . . . .                                  | 19        |
| 3.1.1 Substrate cleaning . . . . .                                | 19        |
| 3.1.2 Film Deposition . . . . .                                   | 20        |
| 3.1.3 Annealing . . . . .   | 23        |
| 3.2 Sample characterization . . . . .                             | 27        |
| 3.2.1 Spectroscopic Ellipsimotry . . . . .                        | 27        |
| 3.2.2 Raman Spectroscopy . . . . .                                | 30        |
| 3.2.3 Photothermal Deflection Spectroscopy . . . . .              | 33        |
| 3.2.4 X-Ray Photoelectron Spectroscopy . . . . .                  | 39        |

---

|          |  |           |
|----------|--|-----------|
| <b>4</b> | <b>Results &amp; Discussion</b>                | <b>41</b> |
| 4.1      | Carbolite furnace annealing . . . . .          | 42        |
| 4.2      | Rapid thermal annealing furnace . . . . .      | 45        |
| 4.2.1    | Influence of annealing atmosphere . . . . .    | 45        |
| 4.2.2    | Influence of silicon content . . . . .         | 48        |
| 4.2.3    | Influence of annealing temperature . . . . .   | 54        |
| 4.2.4    | Influence of annealing time . . . . .          | 57        |
| 4.2.5    | Influence of Si-rich layer thickness . . . . . | 72        |
| <b>5</b> | <b>Conclusions &amp; Recommendations</b>       | <b>81</b> |
| 5.1      | Conclusions . . . . .                          | 81        |
| 5.2      | Recommendations . . . . .                      | 84        |
| <b>A</b> | <b>Appendix A</b>                              | <b>85</b> |
| <b>B</b> | <b>Appendix B</b>                              | <b>87</b> |
| B.1      | PDS measurement fitting procedure . . . . .    | 87        |

---

# List of Figures

|  |    |
|--|----|
| 1.1 PV manufacturing capacity of different regions of the world between 2005 and 2013. Data reported by International Energy Agency [2] . . . . .  | 2  |
| 1.2 Efficiency of solar cell generations as a function of module cost per square meter [3].  | 4  |
| 1.3 Fraction of AM1.5 spectrum which can be converted into electricity by a single junction crystalline silicon solar cell. Spectral mismatch losses are divided into thermalization loss (top left part) and non-absorption losses (bottom right part) [4].               | 4  |
| 2.1 Schematic representation of the potential function of a quantum well . . . . .   | 11 |
| 2.2 Schematic representation of the first four solutions of Schrödinger's equation for a one-dimension quantum well, for two different widths of the well. . . . .   | 11 |
| 2.3 Schematic representation of the potential function of a potential barrier . . . . .  | 12 |
| 2.4 Schematic representation of the band offset between c-Si QDs and different matrices [5]. For c-Si, the reported value corresponds to the bulk material. For crystals subjected to QC effects this value will increase, according to equation 2.8. . . . .              | 13 |
| 2.5 Representation of the dependence of QDs energy band gap on QDs size [6]. . . . .   | 14 |
| 2.6 Crystallization trend of a-Si:H as a function of time and temperature [7] . . . . .  | 16 |
| 3.1 The schematic representation of a RF PECVD deposition system [8] . . . . .   | 21 |
| 3.2 Schematic representation of Stokes and anti-Stokes Raman scattering phenomena  | 31 |
| 3.3 Schematic representation of a-SiO <sub>x</sub> DOS . . . . .   | 34 |
| 3.4 Schematic representation of c-Si QDs DOS . . . . .   | 36 |
| 3.5 Absorption coefficient $\alpha(\lambda)$ spectra of an hydrogen-free a-SiO <sub>x</sub> film and a crystallized film . . . . .   | 37 |
| 4.1 Energy band gap <b>(a)</b> and relative hydrogen content <b>(b)</b> of samples as-deposited and annealed from 400 to 500 °C for 30 min. . . . .  | 42 |
| 4.2 Raman spectra of samples as-deposited and annealed for 30 min at 450 and 500 °C  | 43 |
| 4.3 Raman spectra comparison: LSM and HSM peak fitting and relative hydrogen content of samples annealed in different atmospheres. <b>(a)</b> As deposited. Annealed at 500 °C for 3 min <b>(b)</b> in N <sub>2</sub> (sample 2). and <b>(c)</b> in FG (sample 1). . . . . | 46 |

|      |   |    |
|------|---|----|
| 4.4  | Comparison of $\alpha(\lambda)$ spectra of an as-deposited sample, sample 1 ( $t_{Annealing}=6$ min) and sample 2 ( $t_{Annealing}=3$ min) at 500 °C. . . . .   | 46 |
| 4.5  | Comparison of $\alpha(\lambda)$ spectra of sample 3 (annealed in FG) and sample 4 (annealed in N <sub>2</sub> at 1000 °C for 3 min. . . . .   | 47 |
| 4.6  | Comparison of Raman spectra of samples annealed at 1000 °C for 3 min in N <sub>2</sub> and in FG. . . . .   | 47 |
| 4.7  | LSM and HSM peak fitting and relative hydrogen content of samples with different Si content. <b>(a)</b> , <b>(d)</b> , <b>(g)</b> As deposited. <b>(b)</b> , <b>(e)</b> , <b>(h)</b> Annealed at 500 °C for 3 min in FG, <b>(c)</b> , <b>(f)</b> , <b>(i)</b> Annealed at 500 °C for 6 min in FG. . . . .   | 50 |
| 4.8  | <b>(a)</b> Absorption coefficient $\alpha(\lambda)$ and <b>(b)</b> $\alpha$ at 1.5 eV for samples 1, 2 and 3, as-deposited and annealed at 500 °C for 6 min. . . . .  | 50 |
| 4.9  | Comparison of $\alpha(\lambda)$ spectra: samples 1, 2 and 3 annealed at 1000 °C for 3 min in FG . . . . .   | 51 |
| 4.10 | Integrated QDs DOS (right axis) and crystallinity (left axis) as a function of silicon content in the as-deposited samples, after annealing at 1000 °C for 3 min in FG atmosphere. . . . .  | 52 |
| 4.11 | QD energy band gap as a function of silicon content in the as-deposited samples, after annealing at 1000 °C for 3 min in FG atmosphere. . . . .   | 52 |
| 4.12 | Crystallinity (left axis) and integrated QD DOS (right axis) of samples annealed from 900 to 1040 °C for 3 min in FG atmosphere. . . . .  | 54 |
| 4.13 | QDs energy band gap (left axis) and standard deviation of QDs DOS distribution (right axis) of samples annealed from 950 to 1040 °C for 3 min in FG atmosphere. . . . .   | 55 |
| 4.14 | Absorption coefficient $\alpha$ at 1.5 eV of samples annealed from 900 to 1040 °C for 3 min in FG atmosphere. Note that the $x$ -axis step size is <b>not</b> constant. . . . .   | 55 |
| 4.15 | Crystallinity of samples annealed at 980, 1000 and 1020 °C for 0.5 min to 5 min <b>(a)</b> in FG atmosphere and in <b>(b)</b> N <sub>2</sub> atmosphere. . . . .  | 57 |
| 4.16 | Integrated QD DOS of samples annealed at 980, 1000 and 1020 °C for 0.5 min to 5 min <b>(a)</b> in FG atmosphere and in <b>(b)</b> N <sub>2</sub> atmosphere. . . . .  | 59 |
| 4.17 | QDs energy band gap of samples annealed at 980, 1000 and 1020 °C for 0.3 min to 5 min <b>(a)</b> in FG atmosphere and in <b>(b)</b> N <sub>2</sub> atmosphere. . . . .  | 59 |
| 4.18 | QD DOS standard deviation of samples annealed at 980, 1000 and 1020 °C for 0.3 min to 5 min <b>(a)</b> in FG atmosphere and in <b>(b)</b> N <sub>2</sub> atmosphere. . . . .  | 60 |
| 4.19 | Sub-band gap absorption at 1.5 eV of samples as-deposited, upon hydrogen effusion and annealed at 980, 1000 and 1020 °C for 0.5 min to 5 min. <b>(a)</b> in FG atmosphere and in <b>(b)</b> N <sub>2</sub> atmosphere. Note that the $x$ -axis step size is <b>not</b> constant in this figure. . . . .   | 61 |
| 4.20 | <b>(a-1)</b> Crystallinity and <b>(a-2)</b> $E_{QD}^{gap}$ as a function of $I_{QD}$ for increasing annealing time in FG atmosphere. <b>(b-1)</b> Crystallinity and <b>(b-2)</b> $E_{QD}^{gap}$ as a function of $I_{QD}$ for increasing annealing time in N <sub>2</sub> atmosphere. . . . .   | 61 |
| 4.21 | <b>(a-1)</b> QDs energy band gap and <b>(a-2)</b> Integrated QD DOS as a function of the QDs' DOS standard deviation for increasing annealing time in FG atmosphere. <b>(b-1)</b> QDs energy band gap and <b>(b-2)</b> Integrated QD DOS as a function of the QDs' DOS standard deviation for increasing annealing time in N <sub>2</sub> atmosphere. . . . . | 62 |
| 4.22 | Imaginary part $\varepsilon_2(\lambda)$ of the dielectric function of boron-doped crystalline silicon wafers as a function of plasma annealing time [9]. . . . .  | 63 |

|      |  |    |
|------|--|----|
| 4.23 | Schematic representation of <b>(a)</b> nucleation a-Si dots and H <sub>2</sub> splitting in atomic hydrogen H <b>(b)</b> crystallization of a-Si into c-Si dots and H diffusion through the film, <b>(c)</b> H diffusion to the QDs interface, formation of an a-Si shell and consequent shrinkage of c-Si QDs . . . . .                                   | 67 |
| 4.24 | Steps of hydrogen enhanced oxygen diffusion through silicon crystals [10]. . . . .   | 68 |
| 4.25 | Ideal Si(111)/SiO <sub>2</sub> interface [11]. Silicon and oxygen atoms are represented by open and closed circles, respectively. . . . .  | 69 |
| 4.26 | Si(111)/SiO <sub>2</sub> interface with sub-oxide bonding in a transition region [11] . . . . .  | 69 |
| 4.27 | Schematic representation of <b>(a)</b> nucleation a-Si dots and H <sub>2</sub> splitting in atomic hydrogen H <b>(b)</b> crystallization of a-Si into c-Si dots and diffusion of H through the film, <b>(c)</b> H enhanced migration of O atoms into the c-Si dots, formation of an a-SiO <sub>x</sub> shell and consequent shrinkage of c-Si QDs. . . . . | 70 |
| 4.28 | Crystallinity of samples with different thicknesses (2, 3, 4 and 5 nm) annealed in N <sub>2</sub> at different temperatures (980, 1000 and 1020 °C) for <b>(a)</b> 3 min <b>(b)</b> 3.5 min <b>(c)</b> 4 min. . . . .  | 73 |
| 4.29 | Integrated QD DOS of samples with different thicknesses (2, 3, 4 and 5 nm) annealed in N <sub>2</sub> at different temperatures (980, 1000 and 1020 °C) for <b>(a)</b> 3 min <b>(b)</b> 3.5 min <b>(c)</b> 4 min. . . . .  | 74 |
| 4.30 | QD energy band gap of samples with different thicknesses (2, 3, 4 and 5 nm) annealed in N <sub>2</sub> at different temperatures (980, 1000 and 1020 °C) for <b>(a)</b> 3 min <b>(b)</b> 3.5 min <b>(c)</b> 4 min. . . . .   | 74 |
| 4.31 | QD DOS standard deviation of samples with different thicknesses (2, 3, 4 and 5 nm) annealed in N <sub>2</sub> at different temperatures (980, 1000 and 1020 °C) for <b>(a)</b> 3 min <b>(b)</b> 3.5 min <b>(c)</b> 4 min. . . . .  | 75 |
| 4.32 | QD energy band gap and QD DOS standard deviation as a function of QD size (2, 3, 4 and 5 nm Si-rich layer thickness) annealed in N <sub>2</sub> at 1020 °C) for 4 min. . . . .   | 76 |
| 4.33 | Crystallinity and integrated QD DOS as a function of QD size (2, 3, 4 and 5 nm Si-rich layer thickness) annealed in N <sub>2</sub> at 1020 °C) for 4 min. . . . .  | 76 |
| 4.34 | $E_{gap}^{QD}$ as a function of $\sigma_{QD}$ for samples with different Si-rich layer thicknesses (2, 3, 4 and 5 nm) annealed in N <sub>2</sub> at different temperatures (980, 1000 and 1020 °C) for different durations <b>(a)</b> 3 min, <b>(b)</b> 3.5 min, <b>(c)</b> 4 min. . . . .   | 77 |
| 4.35 | $I_{QD}$ as a function of $\sigma_{QD}$ of samples with different thicknesses (2, 3, 4 and 5 nm) annealed in N <sub>2</sub> at different temperatures (980, 1000 and 1020 °C) for different durations <b>(a)</b> 3 min, <b>(b)</b> 3.5 min, <b>(c)</b> 4 min. . . . .  | 78 |
| 4.36 | Si layer thickness dependent crystallization behaviour of Si/SiO <sub>2</sub> superlattices according to Zacharias et al. [12]. The solid line represents the trend described by equation 4.7. . . . .   | 79 |
| A.1  | Comparison of $\alpha(\lambda)$ spectra of a laser annealed sample, a sample exposed to hydrogen plasma for 1 h, with a gas flow of 200 sccm, a temperature of 525 °C and an RF power of 5 W and a sample annealed in the same conditions but with no power. . . . .   | 85 |
| A.2  | Comparison of $\alpha(\lambda)$ spectra of a laser annealed sample, a sample exposed to hydrogen plasma for 1 h, with a gas flow of 200 sccm, a temperature of 525 °C and an RF power of 5 W and a sample annealed in the same conditions but with an RF power of 40 W. . . . .  | 86 |

- 
- A.3 Comparison of  $\alpha(\lambda)$  spectra of a laser annealed sample, a sample exposed to hydrogen plasma for 1 h, with a gas flow of 200 sccm, a temperature of 525 °C and an RF power of 5 W and a sample annealed in the same conditions but at a temperature of 425 °C . . . . . 86
- A.4 Comparison of  $\alpha(\lambda)$  spectra of a laser annealed sample, a sample exposed to hydrogen plasma for 1 h, with a gas flow of 200 sccm, a temperature of 525 °C and an RF power of 5 W and a sample annealed in the same conditions but for an annealing time of 2 h. . . . . 86

---

## List of Tables

|     |   |    |
|-----|---|----|
| 3.1 | Deposition gas flow rates and measured silicon content for silicon rich layers . . .  | 23 |
| 3.2 | Deposition gas flow rates and measured oxygen content of silicon dioxide layers .   | 23 |
| 3.3 | Raman Spectroscopy measurements: specifications . . . . .   | 31 |
| 4.1 | Gas flow rates for the deposition of Si-rich and SiO <sub>2</sub> layers. . . . .   | 42 |
| 4.2 | Absorption coefficient at 1.5 eV of as-deposited and dehydrogenated samples with different Si-rich layer thickness. . . . . | 43 |
| 4.3 | Annealing conditions for chapter 4.2.1. . . . .   | 45 |
| 4.4 | QDs characteristics evolution as a function of annealing atmosphere. . . . .  | 48 |
| 4.5 | Deposition conditions for silicon-rich layers and relative silicon content . . . . .  | 49 |
| 4.6 | <b>(b)</b> . . . . .  | 50 |
| 4.7 | Crystallinity of samples 1, 2 and 3 after annealing in FG at 1000 °C for 3 min. . .   | 51 |
| 4.8 | QDs evolution as a function of silicon content . . . . .  | 52 |
| 4.9 | Gas flow rates for the deposition of Si-rich and near stoichiometric silicon oxide layers. . . . .                          | 72 |



---

# Acknowledgements

I would like to spend now some words to acknowledge the numerous people who supported and endured me during these months of my Master Thesis project. First of all I want to express my gratitude to my daily supervisor Martijn van Sebille. Thank you for your continuous presence in my everyday work, for your advices, for your patience and for never abandoning me, especially when things were not easy. Moreover, I would like to include in my acknowledgements dr. René van Swaaij who was the first, during the course PV Technology, to capture my interest and curiosity in this field. Thank you for precious guidance and feedback during our weekly meetings. A special thank goes also to Tiny Verhoeven, who was very helpful in allowing us to carry out some measurements at his department at TU Eindhoven.

I would like now to express my gratitude to some of my friends.

Grazie Isabella, sei stata la persona che mi è stata più vicina in questi mesi. La tua amicizia è stata e sarà insostituibile, chissà che fine avrei fatto senza di te.

*Ευχαριστω το Βασ για τις συζητησεις σχετικα με την ανυπαρξια των κβαντικων τελειων. Και οχι μονο.*

Last but obviously not least, I will never be grateful enough to my family.

Grazie mamma, papà e sorella per l'enorme, incondizionato e infinito supporto che mi avete dato, non solo durante questi mesi di lavoro, ma per tutta la durata dei miei studi. Mi fate sentire fortunata ogni giorno.

Delft, University of Technology  
26 August 2015

Adele Fusi



---

# Chapter 1

---

## Introduction

The biggest challenge humanity will have to face, in the coming 50 years, is the satisfaction of energy demand [13]. The development of efficient and fossil fuel independent energy technologies is being made necessary by the combination of increasing energy demand and decreasing availability of traditional energy sources. In fact, even if fossil fuels are expected to dominate the energy market for the next few decades, their quick depletion is threatening both the lifestyle of developed countries and the growth of developing countries [14]. The global energy consumption is growing faster each year, according to statistical surveys [15]. This is due not only to higher living standards, but also to population growth which, by 2075, is foreseen to peak around 9.2 billions [16]. An overall investment of about 48 trillion dollars is being earmarked, by the government throughout the world, in order to cover the 56% increase in energy demand which has been foreseen by 2040 [14]. CO<sub>2</sub> emissions correlated to the wide use of fossil fuels for energy generation are proven to be harmful to the environment. The recent increase in awareness of environmental issues is pushing governments to promote and support the implementation of renewable energy sources. Moreover, not only they can contribute to a cleaner environment, but also to a higher security in energy supply and in the creation of new employment opportunities [17]. Several renewable energy technologies which can contribute in this transition to the future energy mix, are solar energy, wind energy, hydroelectricity, energy from biomass and geothermal energy [18]. These technologies are also more suitable than traditional energy technologies for small off-grid applications. This makes them extremely appealing for the delivery of electricity to the 1.5 billion people that still, nowadays, have no access to the grid [19].

Among the renewable energy sources listed above, the technology which is expected to give the largest contribution is solar energy [20]. This is reasonable when considering that the sun delivers a power which largely exceeds our needs [20].

### 1.1 Solar energy

The energy yearly consumed by humans is exceeded by a factor of about 6200 by the energy delivered on the Earth's surface by the Sun, which is  $855 \times 10^6$  TWh [2]. This makes solar

energy the most abundant energy source available on our planet. For this reason, the harnessing of solar energy and its conversion into electricity is considered to be the most appealing renewable energy technology and it is expected, within 50 years, to become a major energy source [2]. In the past years a lot of effort was made, in research, to obtain an abatement of the cost of photovoltaic (PV) technologies together with an increase in their performances. Between 2008 and 2012 selling price of PV modules dropped of a factor 5 [2]. This was achieved by a combination of an improvement in the technology itself and the increasing scale of the manufacturing. A key role was also played by the introduction in the market of Chinese low cost PV modules.

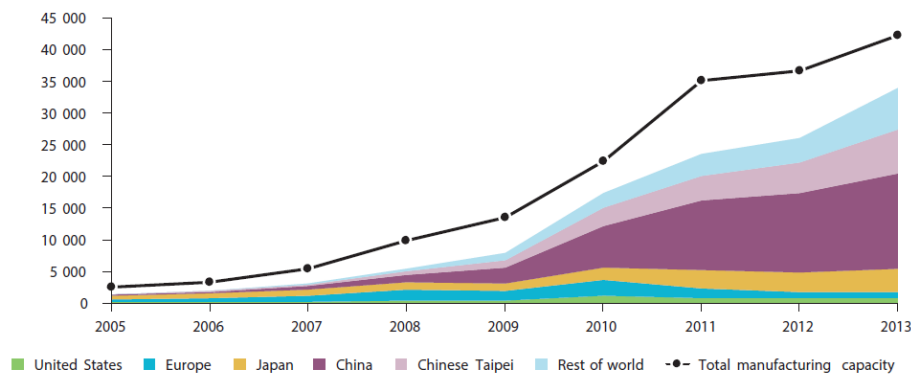


**Figure 1.1:** PV manufacturing capacity of different regions of the world between 2005 and 2013. Data reported by International Energy Agency [2]

In figure 1.1 is shown the trend, as a function of time, of the global PV manufacturing capacity divided by regions [2]. Between 2005 and 2013 the trend is growing, the steeper increase is visible between 2009 and 2011.

## 1.2 Photovoltaic technologies

The working principle of PV modules is the photovoltaic effect [17]. It is a phenomenon which occurs when a semiconductor material is exposed to illumination and it is based on the generation of charge carriers. Electrons in a semiconductor can be found in two different conditions. When they are in the valence band they are strongly bound to the atom, while when they are excited to the conduction band, the bond with the atom weakens and they are free to travel within the material. In semiconductor materials a forbidden band is present between the valence and the conduction bands, no electron can be found in this gap. In addition to thermal-equilibrium concentrations of electrons in the conduction band, an external excitation can provide the electrons with the energy necessary to overcome the forbidden gap. The transition from valence to conduction band can occur if a photon carrying an energy larger than the forbidden band is absorbed by the electron. Upon excitation to the conduction band the electron leaves in the valence band a positively charged "empty" position called hole. Similarly to the electron, a hole can be regarded as a particle free to move within the material. What, spontaneously, follows the charge carriers generation, is their recombination. As electrons tend to reach the lowest and stable energy level, they spontaneously fall

back into the valence band, recombining with the hole. What allows the direct generation of electricity upon photon absorption, in semiconductor based devices, is the separation of the carriers, followed by their collection at opposite sides of the device. Solar cells are devices which directly convert solar radiation into electricity, and their functioning is based on the photovoltaic effect. Different PV technologies were initially classified into first, second and third generation solar cells [1.2]. This division was made depending on the material used and the operation of the device [3]. A recent and drastic shift of the PV modules origin of production (see figure 1.1) caused the price of first generation solar cells to significantly drop. This mined the financial competitiveness of second generation solar cells and the scenario in which they will progressively enter the market and replace first generation solar cells faded [2]. The classification introduced by Conibeer et al., though, may still be used to underline the features of different PV technologies.

The first generation of solar cells includes devices made of crystalline material, mainly mono and multi-crystalline silicon. They currently take up to 80-90 % of the market and they are therefore the dominant PV technology [21]. For this PV generation, the maximum theoretically achievable efficiency is subjected to the so called Shockley-Queisser limit, which is 29.43 % [17]. The maximum efficiencies reached by mono and multi crystalline solar cells are 25.6 % and 25.0 %, respectively [22, 23]. A relevant drawback of first generation solar cells is the relatively thick layer of absorber material needed for their functioning (300-500  $\mu\text{m}$ ) and the high temperature conditions needed for their fabrication process [21].

The second generation of solar cells consists of thin-film devices. The materials used in this category are mainly amorphous silicon (a-Si), Cadmium Telluride and Copper Indium Selenide. These materials, due to a higher absorption coefficient compared to crystalline silicon, allow the use of much thinner absorber layer (300-500 nm) [21]. Also, the fabrication of these layers requires relevantly lower process temperatures. A major limitation of thin-film solar cells is raised by the fact that the amorphous structure of the absorber layers is richer in defects than the ordered crystalline structure. This leads to higher recombination losses and lower conversion efficiency of sunlight into electricity [8]. Typical commercial thin-film module efficiencies span between 5 and 10 % and the share of market occupied by this category is about 10 % [21].

The third generation of solar cells is based on novel materials and emerging technologies, not yet established in the PV market. This category includes dye synthesized solar cells, polymer solar cells, multi-junction/tandem solar cells and quantum dot (QD) solar cells [21].

The goal of third generation solar cells is to increase the conversion efficiency, overcoming the Shockley-Queisser limit, while maintaining the advantage of low-cost manufacturing of thin-film modules.

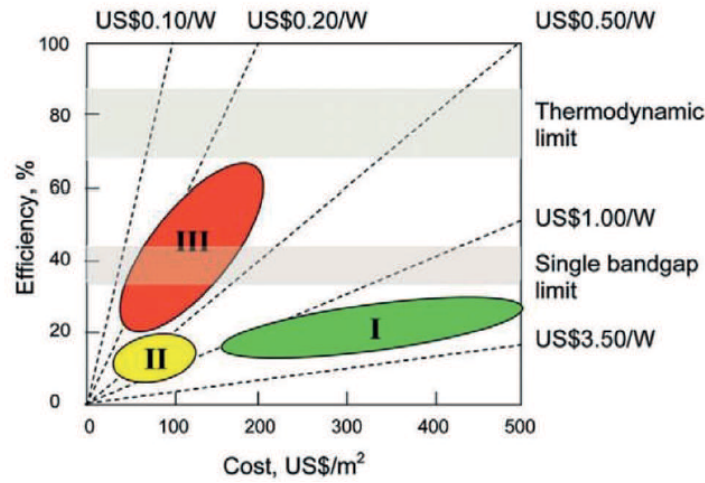


**Figure 1.2:** Efficiency of solar cell generations as a function of module cost per square meter [3].

### 1.3 Motivation

Each PV technology suffers from spectral mismatch. In figure 1.3 is shown the mismatch between the available spectrum AM 1.5 and the fraction that a single junction crystalline silicon solar cell exploits. All the photons that carry a larger energy than the band gap are absorbed, but the excess energy is released as heat, this type of losses is regarded as thermalization losses. Photons which carry too low energy are not absorbed, this type of loss is called non-absorption loss. The sum of these two contributions constitutes the so-called spectral mismatch losses [4].

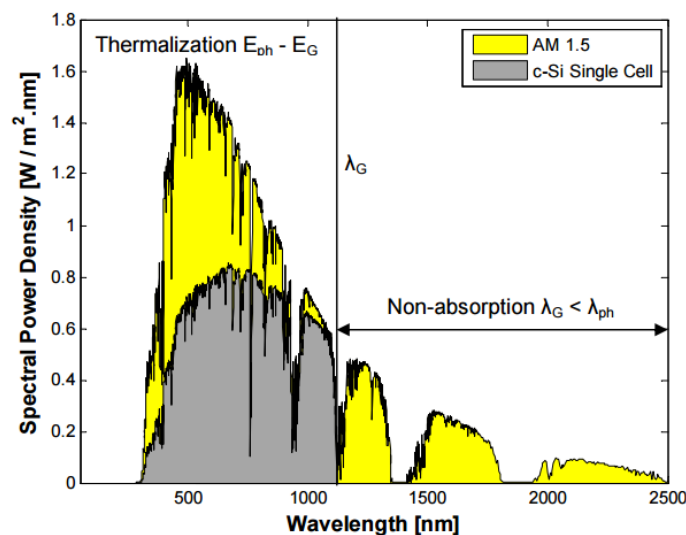


**Figure 1.3:** Fraction of AM1.5 spectrum which can be converted into electricity by a single junction crystalline silicon solar cell. Spectral mismatch losses are divided into thermalization loss (top left part) and non-absorption losses (bottom right part) [4].

A new concept of 'all-silicon' tandem solar cells was introduced as a way of tackling the theoretical conversion efficiency which affects first generation solar cells [5]. According to this concept, each layer of the stack should be optimized in order to absorb different ranges of the solar spectrum [5]. The goal is therefore the improvement of conversion efficiency by means of a reduction of spectral mismatch losses [5]. For three-cell tandem stack, a theoretical efficiency of 47.5% has been calculated [24]. This concept is also interesting since silicon is one of the most abundant materials on the earth's crust, it is low-cost and non-toxic [8].

The use of QDs in PV applications is made appealing by the fact that, when reducing the size of the crystals to a very small scale (2-10 nm), the optical and electrical properties of the material become dependent on the size of the particles (see section 2.5). Given this peculiarity, crystalline silicon QDs embedded in a silicon-based dielectric matrix are a promising candidate as top cell in 'all-silicon' solar cells. Different materials such as  $\text{SiO}_2$ ,  $\text{Si}_3\text{N}_4$  and  $\text{SiC}$  have been studied as host matrices. Numerous studies have been done, already, on the material fabrication and in the development of working devices in relation to QD containing films [25]. The fabrication of QD containing film is divided in two main steps: the deposition of the film and a post-deposition thermal treatment. The deposition can be done in two typical approaches: (a) the deposition of a single layer of silicon rich material (b) the deposition of a superlattice of alternating silicon rich and insulating layers. Various deposition methods have proven to be suitable for QDs fabrication. The most widely used are chemical vapour deposition, magnetron sputtering, evaporation and ion implantation [25]. The deposition conditions determine the silicon content of the layer and so the final QDs size and the spacing between adjacent QDs, which in turn determine the electrical properties of the material [12]. The post-deposition annealing aims to the phase separation of the excess silicon and its crystallization [25]. It can be done either by rapid thermal annealing (RTA) or in conventional tube furnace [26, 27]. However, the high annealing temperatures (typically from 1000 to 1100 °C) imply a high thermal budget which might result in too high fabrication costs as well as in poor performance of the device [27, 28]. The annealing step is crucial as it determines the extent of phase separation and the crystallization degree of the film [29, 30, 31]. Even though RTA treatments can lead to higher crystallinity [26] and are a quick and cost effective tool, the fast temperature ramping causes residual stress in the film due to thermal shock [32, 33]. This, in combination with hydrogen effusion and consequent increase in defect density, results in poor electrical conductivity of the films [34].

Another fabrication method was reported, which does not include post-deposition annealing step [35]. According this procedure Basa et al. were able to obtain the fabrication of crystalline silicon QDs in a one step deposition.

c-Si QDs have already been incorporated in functioning solar cells in different configurations [36, 37, 38]. The highest conversion efficiency (13.4%), was obtained by a p-type c-Si QDs/n-type c-Si heterojunction device. However, all of them have shown low short-circuit current density, which has been attributed to the poor carrier transport properties of QDs containing layers [25]. Also, the open circuit voltage obtained from these devices is lower than what expected from an absorber layer material with a higher band gap than bulk c-Si [25]. Internal quantum efficiency measurements of QDs solar cells have shown a higher blue response with respect than that of single junction c-Si solar cells. This phenomenon was attributed to the absorption from QDs [39]. Since silicon QDs solar cells are fabricated on c-Si wafers, another challenge is the quantification of the contribution of QDs from that of the substrate [25]. To further improve c-Si QDs solar cells performance research is focusing especially on two aspects [25]. First is the development of efficient methods for the synthesis of size and

density-controlled c-Si QDs. The second is the fabrication of a material with good conductive properties, meaning low defect density and QDs spacing. From these premises starts the motivation of our work. As it will be thoroughly explained in the next chapters, the aim of this project is the investigation of the influence different process parameters have on the optical properties of c-Si QDs embedded in a silica matrix and possibly gain control on the QDs size and properties.

## 1.4 Research goals & objectives

As previously mentioned, QDs all-silicon solar cells belong to the third generation of solar cells. This technology is a very appealing research topic, as it can potentially allow the fabrication of PV modules made of abundant and non-toxic material and to overcome the theoretical limits of first generation solar cells. On the other hand, more research is still needed to study optimize the fabrication of layers of c-Si QDs embedded in a dielectric matrix for solar cell applications. In fact, the most widely used technique for the fabrication of such layers includes high temperature treatments, which deteriorate the electrical properties of the material for PV applications. The aim of this work is to assess the influence of different process parameters on the properties of the material. For this purpose different experiments are carried out, in each of which a parameter is varied and the results are analyzed:

- *Annealing procedure*  
Two different annealing setups are investigated: a nitrogen purged carbolite furnace and a rapid thermal annealing furnace, operated in nitrogen and in forming gas. Thanks to this series of experiments it was possible to assess which annealing technique was more suitable for the aim of this work (in terms of annealing setup and atmosphere).
- *Material composition*  
The degree of crystallinity of a film is a measure of the density and spacing of the embedded QDs. The smaller the spacing, the better the electrical properties of the film. The effect of increasing silicon content on the evolution of c-Si QDs is investigated in section 4.2.2, in order to find a material .
- *Effect of annealing time and temperature*  
Another set of experiments is carried out in order to assess the effect increasing annealing time and annealing temperature have on the evolution of QDs optical properties.
- *Effect of different QDs mean size on their optical properties*  
The last experiments deal with the investigation of the effect of different Si-rich layer thickness (and, as a consequence, different mean QDs size) on the QDs optical properties.

## 1.5 Outline of MSc Thesis

In order to give the reader the possibility of better understanding the content of this report, chapter 2 is dedicated to a brief introduction of theoretical matters and it is divided into three parts. The first deals with some fundamentals about quantum mechanics. Quantum confinement effect is introduced and the cases which are interesting and relevant for this work are examined in more detail. The fabrication of our samples consists in two main parts: the deposition and the annealing. In the second part of this chapter an introduction is given on the influence all the fabrication parameters have on the final material. The characterization of the QDs is achieved thanks to an optical model which was previously developed [1]. The third part is dedicated to the explanation of the principles this model is based on.

Chapter 3 gives detailed information about the experimental procedures followed throughout each step of this work in terms of both fabrication and characterization of the samples. An introduction is given also about the setups that were used throughout this work and about the physical principles behind their operation.

In chapter 4 the results of our experiments are extensively presented, commented and discussed.

Finally, chapter 5 is divided in two parts. In the first, on the base of the results obtained, the conclusions of this work are drawn and summarized, while in the second some recommendations for possible future work are proposed.



# Theoretical background

In this chapter a theoretical background is given about what the reader is going to deal with in this report. In section 2.1 the basic principles about quantum mechanics are explored in order to introduce aspects which are more closely related with our work. In section 2.1.1 and 2.1.2 two solutions of Schrödinger's equation, which are of particular interest for this work, are explained. These cases are the potential well and potential barrier, respectively. How the theory so far introduced applies to our work is then discussed in section 2.1.3, together with an introduction to quantum confinement effect and electronic allowed energy states in quantum dot superlattice structures. In the following sections some theoretical considerations regarding the fabrication of quantum dots superlattices are explained. Section 2.1.4 deals with some rudiments about phase separation theory. Follows then, in section 2.2 a discussion about crystallization theories and how they can be applied to our work. In the last part of this chapter, section 2.2.1, the consequences of annealing at different temperatures on hydrogenated amorphous silicon are presented.

## 2.1 Basics of quantum mechanics and quantum confinement

Since during this work we are going to deal with c-Si quantum dots (QD), it is worth mentioning some basic principles that determine the behaviour of such small particles. According to the wave-particle duality, a momentum is attributed to a photon as:  $p = \frac{h}{\lambda}$ , where  $h$  is Planck's constant and  $\lambda$  is the wavelength of the particle [40]. The uncertainty principle, postulated by Heisenberg, applies for very small particles and it states that it is impossible to accurately describe a relationship between conjugate variables. According to the first statement of the principle it is impossible to simultaneously describe the position and the momentum of a particle. The first uncertainty principle is quantitatively described as:  $\Delta p \Delta x \geq \hbar$  [40]. Where  $\Delta p$  is the uncertainty in the momentum,  $\Delta x$  is the uncertainty in the position and  $\hbar = \frac{h}{2\pi}$  is the modified Planck's constant. According to the second statement of the principle it is impossible to precisely describe the energy of a particle and the instant of time it has this energy. Being  $\Delta E$  and  $\Delta t$  the uncertainty in energy and in time, respectively, the second

statement of the uncertainty principle is quantitatively expressed as [40]  $\Delta E \Delta t \geq \hbar$ . What is implied in these statements is that the simultaneous measurement of momentum and position and of energy and time are subjected to an error. Since the modified Planck's constant is very small, the uncertainty principle becomes relevant only for very small particles, such as electrons and subatomic particles. The consequence is that the only way of describing the position or the energy of an electron is to do it in terms of probability. This is done through a probability density function developed by Schrödinger. The motion of electrons within a crystal is described through the wave equation [40]:

$$\frac{-\hbar^2}{2m} * \frac{\delta^2 \Psi(x, t)}{\delta x^2} + V(x) \Psi(x, t) = j \hbar \frac{\delta \Psi(x, t)}{\delta t} \quad (2.1)$$

Where  $m$  is the effective mass of the particle,  $\Psi(x, t)$  is the wave function,  $V(x)$  is the potential function experienced by the particle (independent of time) and  $j$  is the imaginary constant. The wave function expresses therefore the probability of finding a particle in a delimited space at a certain time.  $\Psi(x, t)$  can be written as the product of two functions  $\psi(x)$  and  $\phi(t)$  respectively dependent only on space and time as:  $\Psi(x, t) = \psi(x)\phi(t)$ . Using separation of variables it is possible to obtain the time-independent Schrödinger's wave equation:

$$\frac{\delta^2 \psi(x)}{\delta x^2} + \frac{2m}{\hbar^2} [E - V(x)\psi(x)] = 0 \quad (2.2)$$

Depending on the boundary conditions and on the values of the potential  $V(x)$ , Schrödinger's equation is solved in different ways, describing the motion of electrons in different contexts. For the purpose of this project, the cases of interest are the infinite potential well and the potential barrier.

### 2.1.1 Infinite potential well

In this case the potential function  $V$  is a function of position  $x$ . The space can be divided in three regions, two of them (*I* and *III*) have a potential  $V(x) \rightarrow \infty$ , while in region *II*  $V(x) = 0$  (see figure 2.1). Since a particle cannot penetrate the infinite barrier  $V(x)$ , the probability of finding an electron in regions *I* and *III* is zero, meaning  $\psi(x) = 0$ . The time independent Schrödinger's wave equation, in region *II*, becomes:

$$\frac{\delta^2 \psi(x)}{\delta x^2} + \frac{2m}{\hbar^2} \psi(x) = 0 \quad (2.3)$$

The general solution of this differential equation is [40]:

$$\psi(x) = A_1 \cos(Kx) + A_2 \sin(Kx) \quad (2.4)$$

The normalized solution of equation 2.3 is  $\psi(x) = \sqrt{\frac{2}{a}} \sin\left(\frac{n\pi x}{a}\right)$ . The wave function is therefore a sinusoidal function dependent on the quantum number  $n$  ( $=1, 2, 3, \dots$ ) and on the well width  $a$ . From the boundary conditions, it is also found that  $K = \frac{2mE}{\hbar^2} = \frac{n^2 \pi^2}{a^2}$ , providing an expression for the particle energy states [40]:

$$E = \frac{\hbar^2 n^2 \pi^2}{2ma^2} \quad (2.5)$$

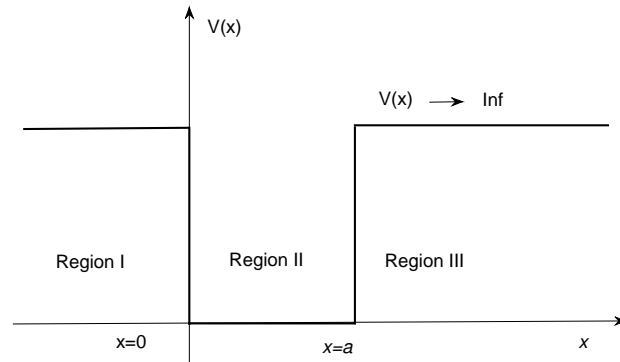


**Figure 2.1:** Schematic representation of the potential function of a quantum well

$E$  shows a strong quadratic dependence on both the width  $a$  of the well and the quantum number  $n$ . Meaning that confining the dimension of the system has a dramatic effect on the energy of allowed states.

In figure 2.2 the schematic representation of the solution of Schrödinger's equation for a mono-dimensional particle confined in a well and its correspondent energy levels are shown. The quantum number  $n$  is varied from 1 to 4. Two different widths are considered,  $a$  (represented by black solid lines) and  $\frac{a}{2}$  (represented by red dashed lines). As can be noticed from the figure, when the width of the well is halved, the frequency of the sine wave is doubled, and the distance between adjacent energy levels is quadrupled. This indicates how crucial the width of the well is in determining the particle allowed energy levels.

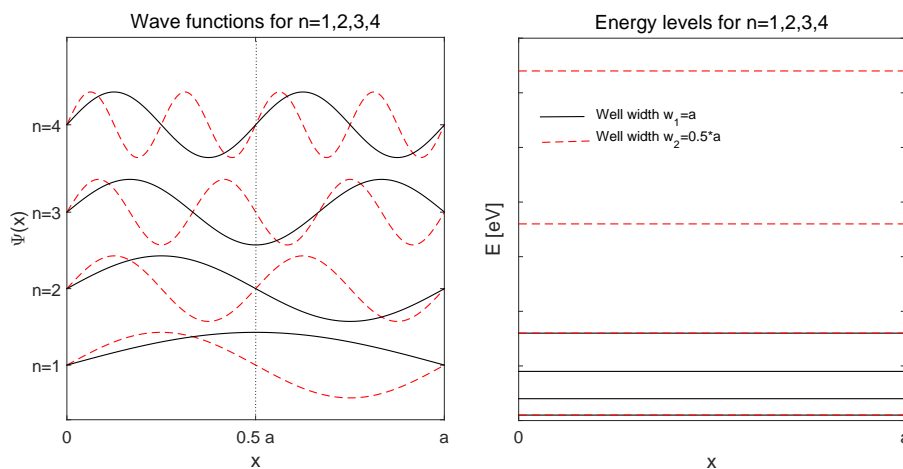


**Figure 2.2:** Schematic representation of the first four solutions of Schrödinger's equation for a one-dimension quantum well, for two different widths of the well.

### 2.1.2 Potential barrier

Another relevant case is found when the total energy of the particle is  $E < V_0$ .

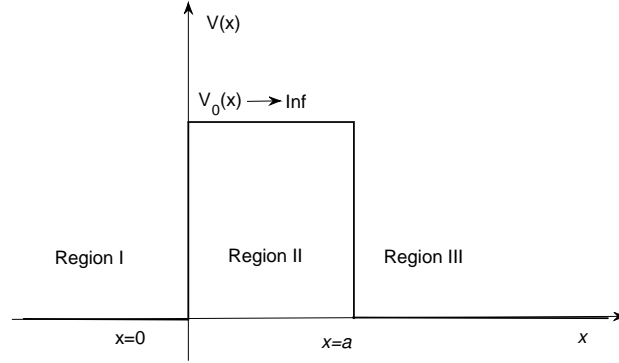


**Figure 2.3:** Schematic representation of the potential function of a potential barrier

When considering a flux of particles traveling in the  $x$  direction, it would be impossible, according to classical mechanics, for it to overcome the potential barrier. However, the probabilistic nature of quantum mechanics leads to a finite probability, for a particle, to surmount the barrier and exist beyond it. This phenomenon is called tunneling effect. So, the ratio between the transmitted flux in region *III* and the incident flux coming from region *I* expresses the probability of a particle to cross the potential barrier. This parameter is defined as the transmission coefficient [40]. It is found by solving Schrödinger's equation for the three regions shown in figure 2.3 and calculating the ratio  $\psi(III)/\psi(I)$ .

$$T \approx 16 \left( \frac{E}{V_0} \right) \left( 1 - \frac{E}{V_0} \right) \exp(-2K_2a) = 16 \left( \frac{E}{V_0} \right) \exp \left( -\sqrt{\frac{8a^2m(V_0 - E)}{\hbar^2}} \right) \quad (2.6)$$

This result indicates that there is a finite probability of finding a particle in region *III*, even when the total energy carried by the particle is much lower than the potential barrier. The tunneling probability shows to be exponentially proportional to the difference between the energy of the electron and the potential barrier, the width of the well and effective mass of the electron.

### 2.1.3 Quantum confinement in QDs superlattices

The phenomena explained in the previous sections show up in the electrical properties of QDs embedded in a dielectric matrix. Depending on the number of dimensions in which the particle is confined, different quantum confinement regimes establish:

- 1D confinement: nanowires

- 2D confinement: quantum wells
- 3D confinement: quantum dots

The strongest quantum confinement is observed for dots constrained in three dimensions [40]. QDs can be thought of as more complex three-dimensional quantum wells and the host matrix as the barrier by which they are surrounded, while the electrons correspond to the confined particles. The allowed energy states of the electrons are therefore discretized and determined by equation 2.5 which adapted for 3D confinement becomes [40]:

$$E_{n,m,l} = \frac{\hbar^2 \pi^2}{2m} \left( \frac{n^2}{a_x^2} + \frac{m^2}{a_y^2} + \frac{l^2}{a_z^2} \right) \quad (2.7)$$

Where  $a_x$ ,  $a_y$ ,  $a_z$  are the three confined dimensions and  $n$ ,  $m$  and  $l$  are the three correspondent quantum numbers. 3D confinement introduces additional energy states with respect to 1D confinement. Quantum confinement occurs, more specifically, when the radius of the QD is smaller than the free exciton Bohr radius which, for silicon, is approximately 5 nm [41]. The density of allowed QDs energy states will be further dealt with in section 3.2.3.

For what concerns the transmission coefficient  $T$  (see equation 2.6), the width of the potential barrier represents the spacing between dots. This is the reason why it is crucial to be able to tune the distance between dots for tunneling to happen. In fact, if the dots are distributed close enough to each other, the wave functions of adjacent QDs overlap significantly and the carriers can travel through the material via tunneling effect creating a QDs superlattice. The band offset  $V_0 - E$  represents, in QDs superlattices, the difference in energy between the bottom of the conduction band of the matrix and the confined energy level of the QD. A schematic representation of the band offset between bulk c-Si and different dielectric matrices is showed in figure 2.4.

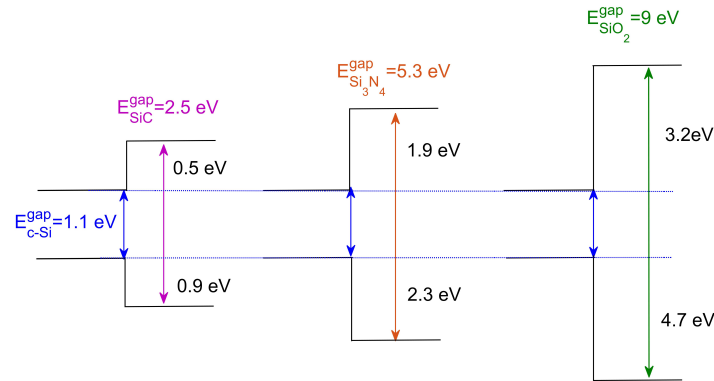


**Figure 2.4:** Schematic representation of the band offset between c-Si QDs and different matrices [5]. For c-Si, the reported value corresponds to the bulk material. For crystals subjected to QC effects this value will increase, according to equation 2.8.

The expression for the tunneling probability contains information about the degree of interaction between QDs. The value of band offset is determined by the matrix material in which the dots are embedded and by the size of the QDs. Depending on the value of  $V_0$ , charge transport by tunneling is possible for different spacing. For silicon carbide (SiC) a spacing around 4 nm is estimated to be sufficient, while in silicon oxide (SiO<sub>2</sub>) the dots should not be placed at more than 1-2 nm apart [42].

### 2.1.4 Quantum confinement & Phase separation

What it is aimed for in the fabrication of c-Si QDs is the control of their size and their size dispersion. In fact, as earlier mentioned in section 1, what makes the application of QDs in solar cells most attractive, is the tunability of their optical properties with size (see figure 2.5). The QDs energy band gap and their size are related to each other by [43]:

$$E_{QD}^{gap}(D) = E_{bulk} + \frac{A}{D^2} \quad (2.8)$$

Where  $D$  is the diameter of the dot  $E_{bulk}$  is the energy band gap of the bulk material and  $A$  is a parameter which depends on the QD material, on the confinement regime (1D, 2D or 3D) and on the number of confined dimensions. The induced energy band gap of a quantum dot corresponds therefore to the value of the bulk semiconductor material band gap, plus the confined energies of the electron and hole.

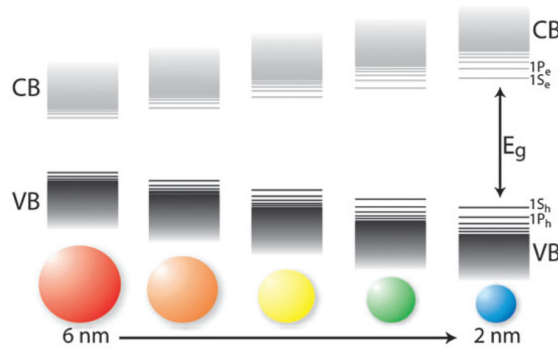
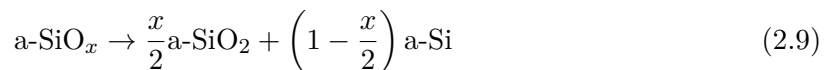


**Figure 2.5:** Representation of the dependence of QDs energy band gap on QDs size [6].

Size controlled Si QD synthesis is possible to achieve, as proven by Zacharias et al. [42], by the fabrication of a-SiO<sub>x</sub>/SiO<sub>2</sub> superlattices, followed by high temperature annealing. Thermal annealing at a higher temperature than the crystallization threshold results in the separation of the two constituent phases. The excess silicon precipitates to form QDs and leaves a network of nearly stoichiometric silicon dioxide. The precipitated atoms condense into embryos which are the nuclei of the crystals. The nuclei then grow and incorporate diffusing Si atoms. This occurs according to equation 2.9 [34, 44].



At this stage the condensed silicon is still in an amorphous phase. When the threshold temperature is reached, a solid phase transition occurs and they become crystalline. This

transition is similar to the crystallization of a-Si:H, suggesting that the two phenomena are governed by the same mechanism [34, 44].

The size of the clusters depends on the excess silicon, which is determined by the subscript  $x$  and by the thickness of the a-SiO<sub>*x*</sub> layer. Also a critical amount of oxygen in the material ( $x \sim 1.8$ ) above which crystallization does not occur was reported [34].

The kinetics of phase separation of excess silicon in sub-stoichiometric a-SiO<sub>*x*</sub> upon thermal annealing has been the object of several studies, both in conventional furnaces [45] and in rapid thermal annealing furnace [46, 47]. The progression of the decomposition reaction is observed to be a nearly linear with temperature and independent on the initial composition. Phase separation is complete, for annealing at 1000 °C, after only 1 s, in this case the nuclei are found to already be in the crystalline phase. Such a fast kinetics of the process is attributed to oxygen diffusion through the matrix [47]. Phase separation, though was also observed for much lower temperatures (750 °C). In this case the nuclei are in the amorphous phase.

Upon crystallization, the QDs show a size distribution that ranges around the thickness of the silicon-rich layers and, according to phase separation theories [34, 44], their shape is approximately spherical. The size dispersion is partly explained by the fact that, due to the presence of an original a-SiO<sub>*x*</sub>/SiO<sub>2</sub> interface roughness, some crystals can have one or two atomic layers more on each side of the interface [34]. Note that such a precise control of the crystal size can not be realized with other fabrication techniques, such as ion implantation or annealing of thick a-SiO<sub>*x*</sub> layers, which result in randomly distributed and sized QDs in the matrix. Assuming complete crystallization, the phase separation of a-SiO<sub>*x*</sub> automatically ensures that the QDs are separated from each other by a shell of silicon dioxide (a-SiO<sub>2</sub>) [34]. The amount of excess silicon determines therefore the spacing between the QDs, hence their density within a given layer. The thickness of the SiO<sub>2</sub> buffer layer provides control on the overall QDs density in the film [34]. From transmission electron microscopy images is also noticeable a tidy self arrangement, which is connected to the chosen stoichiometry and thickness of the buffer layer. The QDs of adjacent layers appear to be forming in the middle of other two adjacent QDs. Periodic strain fluctuation in the network can explain this behaviour [34].

## 2.2 Crystallization theory

When a film of a-Si is brought to a temperature greater than the initial temperature of nucleation, the atomic structure within the thin film starts rearranging and crystalline nuclei begin to form [7, 48, 49]. This can be measured with Raman spectroscopy where, for increasing annealing time and temperatures, the intensity of the transverse optical (TO) mode of a-Si decreases and the TO mode of c-Si appears and increases in sharpness and intensity. This indicates the transition of the Si-Si bonds from amorphous to crystalline phase. An exponential model can usually describe the kinetics of thermal crystallization behaviour of a-Si. This process depends on parameters such as [48]:

- The incubation time  $\tau_0$ , defined as the effective time required to reach a stable state for nucleation from the initial state of the film.  $\tau_0 \propto T_{Annealing} \exp(\frac{E_d}{kT})$ , where  $T_{Annealing}$  is the annealing temperature,  $E_d$  is the activation energy of self diffusion in a-Si.
- The grain growth rate  $\nu_g$ , which is exponentially proportional to the ratio  $\frac{\Delta G}{kT}$ , where

$\Delta G$  is the Gibb's free energy difference between the crystalline and the amorphous phase. The more negative the  $\Delta G$ , the more spontaneous the process is.

- The nucleation rate
- The activation energy of the process  $E_a$

The assumptions made in this model are that nucleation does not start before the incubation time has passed and that, when nucleation becomes stable,  $\nu_g$  becomes independent of time. The crystallinity fraction  $X_c$  of the film is then described as a function of these parameters as:

$$X_c = 1 - \exp \left[ -\frac{(t - \tau_0)^3}{\tau_c^3} \right] \quad (2.10)$$

Where  $\tau_c$  is the characteristic crystallization time and it is inversely proportional to the annealing temperature. It expresses the time required for thin film crystallization under a certain annealing temperature to start.

According to this model, the crystallinity evolution can be described in three phases (see figure 2.6): i) it remains zero (meaning that the material is still fully amorphous) for the whole incubation time. ii) after  $\tau_0$  has passed it starts increasing with increasing annealing time. iii) after a certain time it reaches a saturation value and becomes independent of annealing time. While for a-Si:H an annealing temperature of 700 °C is sufficient for a complete crystallization, we know from literature [12] and from the experiments reported in section 4.2.3 that in case of a-SiO<sub>x</sub> a higher temperature is needed (~950-1000 °C).

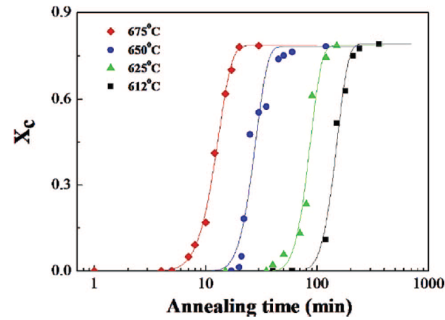


**Figure 2.6:** Crystallization trend of a-Si:H as a function of time and temperature [7]

### 2.2.1 Annealing induced defects

The evolution of paramagnetic centers (spin density) throughout the annealing process is studied by K. Ding et al. [50, 51]. It is observed that, during annealing, an important process is the release of hydrogen from the deposited films with the subsequent formation of dangling bonds. Additional defects cause an increased sub-band gap absorption, which is shown by a lower photo-luminescence intensity, a symptom of poor photovoltaic performance [50]. At every temperature the formation of new dangling bonds is assumed to be proportional to the overall amount of hydrogen effused. On its turn, the hydrogen effusion is a temperature dependent phenomenon. This shows a direct correlation between the dangling bond creation and the annealing temperature. The formation of new dangling bonds is expected to be

ruled by thermal motion of atoms [50, 51]. The observed behaviour for increasing annealing temperature is an initial increase in defect states, followed by a decrease that shows that a portion of defects is “healing”. Since this phenomenon starts at temperatures much lower than the one expected for bulk silicon solid phase crystallization, it cannot be explained by the passivation of silicon QDs interface by SiO<sub>2</sub>. It is explained by a probable recombination of dangling bonds during the structural reconstruction of the material and it suggests the presence of neighbouring dangling bonds. The recombination increases if atoms can exchange place via diffusion through the material. The formation of new bonds and the diffusion through the material are regarded as thermally activated processes, so the healing of dangling bonds is modeled to exponentially increase with temperature. The recombination probability is expressed as:

$$f(T_{Annealing}) = A \exp\left(-\frac{E_a}{k_B T_{Annealing}}\right) \quad (2.11)$$

Where  $E_a$  is the activation energy of the healing process,  $k_B$  is the Boltzmann constant,  $A$  is a factor which indicates a measure of the efficiency of defect healing and  $T_{Annealing}$  is between 450 and 1050 °C. The combination of the increase in dangling bond density due to hydrogen effusion and its decrease due to bond reconstruction results in the observed non-monotonous trend in defect sate density. Ding et al. analyzed different ways of passivating annealing induced defects by hydrogen reincorporation in the material [51]. The expected trend is verified in all the analyzed samples, which show a decreased spin density confirming the passivation of unsaturated bonds within the material, but the effects of hydrogen reincorporation on the sub-band gap absorption are found to be weak [51].



# Experimental procedures and setups

During the fabrication and characterization of our samples, several experimental setups were used in this work. This chapter is dedicated to a detailed discussion about each procedure we followed and to an explanation about the structure and functioning of each setup we used. The first section deals with the fabrication procedure of the samples (3.1). It is, in turn, divided into subsections where the single steps are presented, namely the cleaning procedure of the substrates (3.1.1), the deposition of the films (3.1) and their annealing (3.1.3). In the section dealing with the deposition the process parameters are discussed, together with an introduction to the deposition technique: radio frequency plasma enhanced chemical vapour deposition. The influence of different deposition parameters on the characteristics of the film together with the deposition conditions used during this work are discussed in section 3.1.2. Since two annealing setups were used throughout this work, the section dedicated to the annealing procedure is divided in two parts, the first deals with the Carbolite furnace (3.1.3) and the second with the rapid thermal annealing furnace (3.1.3). Follows then the part dedicated to the characterization of the samples. Here are discussed the spectroscopic ellipsometry (3.2.1), Raman spectroscopy (4.2), photothermal deflection spectroscopy (3.2.3) and X-ray photoelectron spectroscopy (3.23). Together with the description of the setups, also an introduction to the physics behind their functioning and to the models we used to process the results are given.

## 3.1 Sample fabrication

### 3.1.1 Substrate cleaning

Using clean substrates is of absolute importance for the quality of the deposition. Small particles, debris and potential residues which might stick on the substrate surface must be removed to guarantee optimal deposition conditions. To limit their contamination, before and after the cleaning, the substrates are only handled and moved using tweezers and while wearing gloves.

### Glass and quartz substrates

Glass substrates (Corning glass XG 10x10 cm) and quartz substrates are thoroughly cleaned in an ultrasonic bath. According to the following procedure the substrates are:

1. Immersed in acetone for 10 min
2. Dried with a nitrogen flow
3. Immersed in isopropylalcohol (IPA) for 10 min
4. Dried with a nitrogen flow

### c-Si Wafer substrate

The cleaning procedure for crystalline silicon wafers is slightly more complex, as it requires the use of strong acids in high concentrations. This cleaning step is necessary in order to remove the layer of native silicon oxide that is present on the surface of the wafer due to the natural oxidation of silicon when left in contact with oxygen at room temperature. If not removed, the layer of native  $\text{SiO}_2$  acts as an insulator layer, hindering the electrical properties of the other film which will be deposited afterwards. The procedure consists of a first dip in nitric acid (99% concentrated) for 10 min, followed by a rinse in demineralized water until the resistivity measured in the bath reaches  $5.0 \text{ M}\Omega$ . This first step removes organic contaminants by oxidising them and isolating them on the surface of the wafer [52]. A second dip is made in boiling nitric acid ( $T=105^\circ\text{C}$  and 69.5% concentrated) for ten minutes, followed by a second rinse in demineralized water. This second step is necessary to remove the metallic contaminants, by forming soluble complexes [52]. The third and last dip is made in hydrofluoric acid (HF 1%) for one minute, followed by a third rinse in demineralized water. This step is necessary to remove the oxide layer containing impurities and the native oxide layer [52]. In order to prevent the native oxide to form again on the surface of the substrates, they need to be quickly placed on a samples holders and loaded in the deposition machine, right after the cleaning procedure. Here vacuum conditions are maintained.

## 3.1.2 Film Deposition

### PECVD

Radio frequency plasma enhanced chemical vapour deposition (RF-PECVD) is a process used to deposit thin solid films from a gaseous state on various substrates. A mixture of gases is introduced in the deposition chamber, where it is excited into plasma by an oscillating electric field between two electrodes, with a frequency of 13.56 MHz. Once the glow discharge has started, the free electrons begin oscillating due to the applied field and detach from the initial molecules. The components of the gas mixture are then turned into highly reactive radicals, ions and neutral atoms. Secondary electrons are also generated due to the inelastic collision between the free electrons and the initially neutral gas molecules. This process maintains the plasma. The attachment of dissociated molecules to the substrate determines the start the

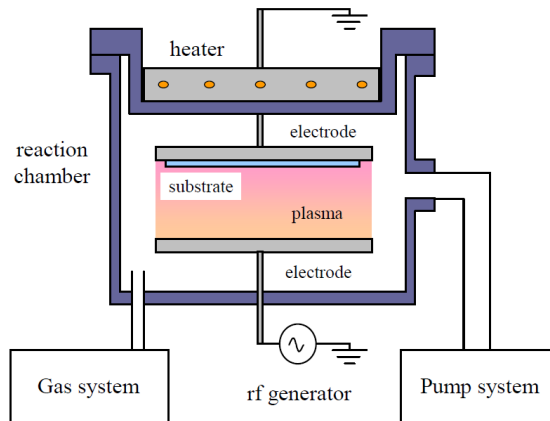


**Figure 3.1:** The schematic representation of a RF PECVD deposition system [8]

deposition of the film. After dissociation occurs, the collisions between electrons and silane molecules are considered the main excitation event in the plasma phase [53].

Composed by five main parts, the PECVD system is a simple setup [8] and it is schematically showed in figure 3.1. A reaction chamber with two parallel electrodes is connected to a gas handling system, which feeds the reaction gases. A vacuum pump is used to keep the pressure in the chamber very low (in the order of mbar), this helps maintaining a stable plasma. A heating system heats up the substrate on which the deposition occurs. The RF generator source provides the necessary power to ignite and maintain the plasma. The use of plasma for dissociation processes, compared to other vapour deposition techniques, offers the advantage of large deposition areas, uniform depositions and lower deposition temperatures [8]. Also, by changing the gas mixture during the same process, it is possible to deposit multilayer structures [8], which is of particular interest for the purpose of this work.

The precursor gases  $\text{SiH}_4$ ,  $\text{CO}_2$  and  $\text{H}_2$  were used for the deposition of  $\text{a-SiO}_x$ . As the material was intrinsic, no dopants were added. The composition and the characteristics of the film depend on several factors among which the precursor gases and their flow rates, the deposition pressure, the temperature of the substrate and the power used.

## AMIGO

This deposition setup consists of six different deposition chambers, each of which is used for different purposes (different gas lines), in order to avoid cross-contamination. Another chamber, the loadlock chamber, is used for loading and unloading the samples. The chambers are connected by a central transport chamber, inside which there is a robot arm. It allows to pick the sample holders and transfer them from one chamber to the other without vacuum breaks.

## Deposition conditions

- *Hydrogen dilution*

The growth surface is characterized by active sites (silicon atoms with at least one dangling bond), and passive sites (silicon atoms with silicon or hydrogen atoms at

each of the four bonds). Atomic hydrogen, which is an extremely reactive species, is produced after the dissociation of  $\text{SiH}_4$  and  $\text{H}_2$  [53]. During the film growth an equilibrium between the hydrogen concentration in the film and that in the plasma is reached, due to its freedom of moving in and out the growth surface [53]. The presence of hydrogen ions in the deposition chamber is a very influential parameter for the film properties. In fact, with higher concentrations the weaker Si-Si bonds are etched and dangling bonds are terminated. This effect leads to a denser and less defective material [53]. High hydrogen dilution also favours the deposition of an amorphous material. On the other hand a too high dilution can result in a too strong ion bombardment and no deposition on the substrate [53].

- *Chamber pressure*

Changes in deposition pressure  $p_{Depo}$  lead to several variations in the outcome material. High  $p_{Depo}$  causes a denser material, lower ion energy (and so lower ion bombardment of the growth surface) and higher deposition rate  $r_{Depo}$  [53]. Besides, high  $r_{Depo}$  causes the formation of powders and so a deterioration of the material (high roughness and porosity) [53]. The growth of powders in the film can be prevented by a lower residence time, obtained, if the pressure needs to be kept high, with a higher gas flow rate.

- *Substrate temperature*

High deposition temperatures ( $T_{Depo} > 200\text{ }^\circ\text{C}$ ) decrease hydrogen concentration in the film and provide a more stable material [53]. The effect the temperature has on the deposition rate is quite limited [53].

- *Radio Frequency power*

For increasing radio frequency power (RF power) values, the electron density increases together with the dissociation rate. It is reflected in a higher deposition rate, but also in a deterioration of the film quality in terms of uncontrolled powder growth and surface roughness [53]. The final composition of the material is also strongly influenced by the power used during deposition. What is observed, by increasing the RF power, is an increase in hydrogen etching effect [54]. The hydrogen content of the film is also affected by the power. For increasing RF power values a faster dissociation of the precursor gases occurs, leading to the presence of more reactive species in secondary reactions and causing the hydrogen fraction to increase. As a consequence the structural disorder increases [54] together with the defect density upon post deposition annealing [55].

Generally, what all the samples that were fabricated during this work have in common, is the structure. It consists of a multi-layer film, where silicon dioxide and silicon-rich layers are alternated.

In the first part of our work a power of  $P=0.128\text{ W cm}^{-2}$ , a pressure of  $p=1.4\text{ mbar}$ , an electrode temperature of  $300\text{ }^\circ\text{C}$  and an electrode distance of  $14\text{ mm}$  are used, for both the silicon-rich and the silicon dioxide layers.

In the second part of our work, for both the materials, a power of  $P=0.0192\text{ W cm}^{-2}$ , a pressure of  $p_{Depo}=1.4\text{ mbar}$ , an electrode temperature of  $200\text{ }^\circ\text{C}$  and an electrode distance of  $14\text{ mm}$  are used.

### Silicon rich layers

Different gas mixtures result in different layer compositions<sup>1</sup>. In order to find a correlation between the silicon content of the layers and the reachable degree of crystallinity several different combinations are used:

**Table 3.1:** Deposition gas flow rates and measured silicon content for silicon rich layers

| SiH <sub>4</sub> [sccm] | CO <sub>2</sub> [sccm] | H <sub>2</sub> [sccm] | Silicon content [%] |
|-------------------------|------------------------|-----------------------|---------------------|
| 8                       | 48                     | 0                     | 66                  |
| 10                      | 27                     | 200                   | 78.1                |
| 10                      | 80                     | 200                   | 65.2                |
| 2.5                     | 9.5                    | 200                   | 57.9                |

### Silicon dioxide

For this buffer layer two different materials were used, according to the gas mixtures reported in table 3.2.

**Table 3.2:** Deposition gas flow rates and measured oxygen content of silicon dioxide layers

| SiH <sub>4</sub> [sccm] | CO <sub>2</sub> [sccm] | H <sub>2</sub> [sccm] | Oxygen content [%] |
|-------------------------|------------------------|-----------------------|--------------------|
| 1                       | 55                     | 0                     | 66                 |
| 2                       | 72                     | 200                   | 56.6               |

The first recipe was only used for the first part of our experiment, where the samples were annealed in the Carbolite nitrogen purged furnace, according to the procedure which will be explained in section 3.1.3.

For the second part of the experiments, the deposition recipe was changed in order to obtain a higher quality material (see second line of table 3.2. In fact, as mentioned in section 3.1.2, higher hydrogen dilution leads to a denser and less defective material.

Since the silicon dioxide layers are used only as buffer layers to maintain the silicon-rich layers separated upon annealing, their thickness was never changed. A constant value of 1 nm was used, which we considered the minimum necessary thickness in order to obtain a uniform deposition.

### 3.1.3 Annealing

As explained in chapter (2.2), in order for QDs to form, the samples need to be annealed at higher temperature than the crystallization temperature which, in our case, as it will be shown in section 4.2.3, is approximately 950 °C. Two different annealing setups were used during this work for the fabrication of QDs. The first one was a Carbolite furnace while the

<sup>1</sup>Values obtained with XPS measurements at TU Eindhoven

second one was a rapid thermal annealing (RTA) furnace. Below a brief description of these two machines is given, together with the experimental procedure followed in each case.

### **Carbolite furnace**

The first annealing experiments were carried out in a Carbolite AAF Ashing Furnace. It is a small furnace, used in R&D context, it has a chamber which can host up to 10 wafers of 4 inches and they are, in turn, loaded on a quartz holder. The maximum continuous operating temperature which can be reached is 1100 °C and the nominal ramp time is of 140 min. The chamber, which has a volume of 3 L, is nitrogen purged and the maximum gas flow rate is 25 L min<sup>-1</sup>. A controller provides a programmable temperature control. It allows to program the furnace up to 8 segment, each of which comprises of ramp (up or down) and a dwelling time. The controller also shows in real time the actual temperature inside the chamber together with the set-point temperature.

### **Annealing procedure**

Two different annealing procedures were used in this part of our work:

1. The furnace was set at a temperature slightly higher than the desired set-point (about 10 °C more). When the temperature was reached, the samples were placed on the quartz holder and loaded in the furnace. Opening the furnace for loading the samples caused the temperature to drop approximately at the desired set point. After the desired annealing time the samples were unloaded, and the temperature could be programmed to the next set point.

This procedure allowed to carry out several annealing per day.

2. The samples were prepared, placed on the quartz holder and loaded in the furnace. In this procedure the programmable controller was used. The ramp up and ramp down rates were set, together with the desired temperature and the dwelling time. The samples were unloaded only when the temperature of the chamber had reached ambient temperature. This procedure took much longer than the previous one, since the ramp down can take up to several hours, depending on the temperature set-point. On the other hand, opening and closing the furnace at ambient temperature, reduced the exposure of samples to high temperature oxygen. In fact, during the ramp up, large part of the oxygen which entered the chamber when the samples were loaded, was purged away by the nitrogen flow.

Depending on the purpose of the investigation, some parameters are varied:

- *Hydrogen effusion*

In this set of experiments the hydrogen effusion from our film was investigated. This phenomenon was studied as a function of annealing temperature, while keeping the annealing time constant to 30 min. The temperature was increased from 400 to 550 °C with an interval of 25 °C. Procedure 1 was followed.

- *Crystallization*

The aim of these experiments was the investigation of the behaviour of the samples upon high temperature annealing. The temperature was varied from 900 to 1075 °C with an interval of 25 °C and the annealing time was kept at 30 min. In this case the experiment was repeated for both procedure 1 and 2.

### Rapid thermal annealing furnace

In the second part of this work the annealing process was carried out with the rapid thermal annealing furnace Solaris 100 RTP. It is a small furnace meant for R&D purposes, it can host samples with a diameter up to 4 inches and heat them up to 1300 °C with a heating rate of up to 60 °C s<sup>-1</sup> [56]. The samples were placed on a crystalline silicon wafer (carrier wafer), which lays on a high purity quartz holder. A thermocouple is mounted on the quartz structure touching the carrier wafer, so that its temperature is monitored during the whole process. Thirteen halogen quartz lamps are distributed on top and at the bottom of the samples, in order to increase the heating uniformity. The chamber can be flushed with flows of pure nitrogen, forming gas (10 % hydrogen and 90 % nitrogen) or argon. The maximum allowed gas flow is 10 slm. A graphical software controller allows to monitor the process in real time.

### Annealing procedure

The samples, both on quartz and on wafer substrate, were loaded in the furnace and placed on the carrier wafer. The first step of the procedure was, always, a nitrogen purge of 60 s, with a flow rate of  $\phi_{N_2}=5$  slm. This allowed to remove most of the air contained in the chamber (moisture and oxygen, at high temperature, are detrimental for the samples annealing). Depending on the annealing recipe, the samples were then kept in a continuous flow of gas ( $\phi_{N_2}=8$  slm) during the ramping up, the dwelling time and the ramping down of the chamber (down to a temperature of 100 °C). Ramping up from ambient temperature to the desired temperature was carried out with a heating rate of 15 °C s<sup>-1</sup>. A purging step with pure nitrogen flow  $\phi_{N_2}=8$  slm was then carried out for two minutes, in order to remove all the hydrogen left in the chamber. Depending on the purpose of the investigation, some parameters were varied:

- *Annealing atmosphere*

For the investigation of hydrogen effusion from the layers two types of annealing environments were used: pure nitrogen and forming gas. In this case the annealing temperature is kept constant at 500 °C and the annealing time 3 min. The temperature is set to such value because from previous experiments it was evinced that at 500 °C all hydrogen contained in the film effused. Complete dehydrogenation was not reached for forming gas annealing. This result was obtained only when the procedure was repeated for a twice as long annealing time. The influence of these two different annealing atmospheres was also investigated on the crystallization of the samples. This procedure which was carried out in both cases at 1000 °C for a duration of 3 min.

- *Silicon & hydrogen content*

For the investigation of the evolution of defects and achievable crystalline fraction as a function of the silicon content of the film, three different deposition recipes were used. The samples were annealed in forming gas for a duration of 6 min at the annealing temperature of 500 °C to investigate the hydrogen effusion from the films. Always in forming gas, the samples were annealed for a duration of 3 min at 1000 °C to investigate the crystallization.

- *Annealing temperature*

For the investigation of the dependence of the degree of crystallinity and the optical properties on the annealing temperature, this parameter was varied with an interval of 20 °C between 900 and 1040 °C. The annealing time was consistently kept at 3 min. The annealing atmosphere was, also in this case, forming gas.

- *Annealing time - Forming gas & Nitrogen gas*

For the investigation of the dependence of the degree of crystallinity and of the optical properties on the annealing time, this parameter was varied with intervals of 30 s between 0.5 and 5 min. The procedure was repeated at three different temperatures: 980, 1000 and 1020 °C and in both the annealing atmospheres.

- *Si-rich layer thickness*

In this experiment the correlation between the Si-rich layer thickness of the samples and their behaviour upon high temperature annealing is investigated. The annealing time is varied between 3, 3.5 and 4 min, while the annealing temperature was increased from 980, to 1000 and to 1020 °C. The procedure is repeated, in all the combinations of annealing temperature and time, for samples with different Si-rich layer thickness.

## 3.2 Sample characterization

After their fabrication and treatment the samples need to be characterized in several aspects. It is done with the help of the different setups described in the following paragraphs.

### 3.2.1 Spectroscopic Ellipsimotry

#### Setup & Working principles

Spectroscopic ellipsometry (SE) is a method of characterizing optical properties of thin film materials by measuring the change in polarization of a beam of light incident on the film before and after reflection (or transmission). The change in polarization is expressed in terms of amplitude ratio  $\Psi$  and phase change  $\Delta$  of the electromagnetic wave. Light is described as an electromagnetic (EM) wave traveling through space, its behaviour in space and time (in terms of phase and amplitude of the signal) is defined as polarization. Polarized light follows a distinct shape (orientation and phase) at any given moment [57]. Two indices are mainly used to express the interaction between light and a material: the refractive index  $n(\lambda)$  and the extinction coefficient  $k(\lambda)$ . They are combined in the complex refractive index  $N(\lambda) = n(\lambda) - ik(\lambda)$  [57]. The real part is defined as the ratio between the propagation velocity of light in the medium and in the vacuum. The complex part is an indicator of the absorption loss encountered when the light is traveling through the medium and it is related to the absorption coefficient as:  $k(\lambda) = \frac{\lambda\alpha}{4\pi}$  [57]. Also the the complex dielectric function  $\tilde{\epsilon}$  describes the optical and electrical properties of a material. Its real part  $\epsilon_1$  is an indicator of how much, when exposed to a magnetic field, a material is polarized. The imaginary part  $\epsilon_2$ , is representative of the portion of energy which is absorbed by the material from the magnetic field.  $\tilde{\epsilon}$  and  $N(\lambda)$  are then correlated according to [58]:  $N(\lambda) = \sqrt{\tilde{\epsilon}(\lambda)} = \sqrt{\epsilon_1(\lambda) \pm \epsilon_2(\lambda)}$ . When a beam of light encounters a surface, part of it is reflected, a part is transmitted and a part is absorbed. Light can be separated into components orthogonal in relation to the incidence plane. The parallel and perpendicular components are defined as p-polarized and s-polarized respectively. Fresnel's equations describe the behaviour of EM waves as a function of their polarization and the refractive indices of the materials they are traveling through [58].

For p-polarized light:

$$\tilde{r}_p = \frac{\tilde{n}_1 \cos\theta_1 - \tilde{n}_2 \cos\theta_2}{\tilde{n}_1 \cos\theta_1 + \tilde{n}_2 \cos\theta_2} \quad (3.1)$$

$$\tilde{t}_p = \frac{2\tilde{n}_1 \cos\theta_1}{\tilde{n}_1 \cos\theta_1 + \tilde{n}_2 \cos\theta_2} \quad (3.2)$$

For s-polarized light:

$$\tilde{r}_s = \frac{\tilde{n}_2 \cos\theta_1 - \tilde{n}_1 \cos\theta_2}{\tilde{n}_1 \cos\theta_2 + \tilde{n}_2 \cos\theta_1} \quad (3.3)$$

$$\tilde{t}_s = \frac{2\tilde{n}_1 \cos\theta_1}{\tilde{n}_1 \cos\theta_2 + \tilde{n}_2 \cos\theta_1} \quad (3.4)$$

Where the subscripts 1 and 2 indicate the two different materials.  $\theta_1$  and  $\theta_2$ , the angles of incidence and refraction, are subjected to Snell's law [58]:  $\sin\theta_1 n_1 = \sin\theta_2 n_2$ . Ellipsometry measurements detect the change in polarization state of the light after reflection or transmission of  $p$  and  $s$  components. The variation is expressed as [58]:  $\rho = \tan(\Psi)e^{i\Delta}$ . Regression

analysis is the most common way of obtaining information from an ellipsometry measurement. Based on the structure of the sample, a model to describe it is implemented. After the sample is measured, the model is used to predict the response from Fresnel's equations. Since they are based on the optical constants of the material and on its thickness, if these quantities are not known, a guess is made on the starting value. Experimental and calculated data are compared. Using MSE (Mean Squared Error) as an estimator of the error, the unknown parameters are varied iteratively until the fit reaches the desired approximation [58].

## Model

Two typical models used for the description of amorphous semiconductors are the Tauc-Lorentz and the Cody-Lorentz models. The former simulates the joint density of states by combining the Tauc band edge with the classical Lorentz broadening function, giving an expression for the imaginary part of the complex dielectric function [59]:

$$\varepsilon_2(E) = \left[ \frac{AE_0(E - E_g)^2}{(E^2 - E_0^2)^2 + C^2E^2} \frac{1}{E} \right] \text{ for } E > E_g \quad (3.5)$$

$$\varepsilon_2(E) = 0 \text{ for } E < E_g \quad (3.6)$$

Where  $A$  is the amplitude,  $C$  is the broadening,  $E_0$  is the peak transition energy,  $E_g$  is the energy band gap and  $E$  is the energy of a wave  $E=h\nu$ . Even though this model proved to be valid for many amorphous materials, it has some limitations due to the fact that the imaginary part of  $\tilde{\varepsilon}$  is neglected for energies below the band gap. For those energies though,  $\varepsilon_2$  will not be zero, due to defects and the intraband absorptions. This last factor becomes more relevant for materials with high energy band gap. Tauc's model calculates  $\varepsilon_2$  on the assumption of parabolic bands and a constant momentum matrix elements [59]:

$$\varepsilon_2(E) \propto \frac{(E - E_g)^2}{E^2} \quad (3.7)$$

Differently, Cody's model derives  $\varepsilon_2$  assuming parabolic bands and constant dipole matrix element, resulting in a different expression near the band edge [59]

$$\varepsilon_2(E) \propto (E - E_g)^2 \quad (3.8)$$

Applying these difference the Cody-Lorentz model was derived by Ferlauto et al. Especially for high  $k$  materials with a high band gap the Cody-Lorentz model shows a higher accuracy (lower MSE) compared to the Tauc-Lorentz model [59].

## Samples measurement

During this work,  $M - 2000$  J. A. Woollam Co., Inc. Spectroscopic Ellipsometer is used to carry out Spectroscopic Ellipsometry measurements. The wavelength range we use is 6.5–0.73 eV, the data is acquired at different light incident angles (55-60-65-70° for quartz samples and 60-65-70-75° for wafer samples), with an acquisition time of 10 s for each angle. Usually, the Cody-Lorentz model was used in the fitting procedure.

In the fabrication of our samples, too thin layers might not be uniform enough to guarantee the separation of the layers upon high temperature annealing, while too thick samples would hinder the desired quantum confinement effect. For these reasons, it is crucial to precisely know the deposition rate  $r_{Depo}$  [ $\text{nm s}^{-1}$ ] of each deposition recipe. This is possible by measuring the thickness  $d_{SE}$  [nm] of some test layers with SE and dividing it by the deposition time  $t_{Depo}$  [s]:

$$r_{Depo} = \frac{d_{SE}}{t_{Depo}} \quad (3.9)$$

Other important parameters that we obtain from SE are the refractive index  $n$  and the thickness  $d$  of the samples. They are necessary, as it will be explained in chapter 2.3 for the fitting of the PDS measurements and the optical properties analysis of the samples.

### 3.2.2 Raman Spectroscopy

#### Setup

When a sample is illuminated, two scattering phenomena occur: Rayleigh scattering and Raman scattering. The former is the dominant process and is an elastic process [60]. The latter is an inelastic process and it is caused by the transition between two adjacent vibrational levels of an atom. In Raman scattering, when light interacts with an atom, it is polarized. More specifically, the cloud of electrons situated around the nuclei is excited to a virtual state. This vibrational state, with a higher energy level when compared to the ground state, is unstable and the photons almost immediately radiate when the electrons drop back to their ground state [60]. Raman spectroscopy detects the variation in the energy carried by the photons. Compared to Rayleigh scattering, Raman scattering is a weak process which involves only one out of  $10^6 - 10^8$  photons [60]. Raman scattering is divided into two different processes: Stokes and anti-Stokes scattering (see figure 3.2). At room temperature most of the atoms are found to be at their lowest energy level. Stokes scattering, which is the phenomenon that is measured in this work, consists in the promotion of electrons into higher energy virtual vibrational states upon the absorption of energy from incident photons. When the electrons fall back to their ground state, the scattered photons experience a drop in energy and so in frequency. The opposite happens in anti-Stokes scattering. What is observed during Raman scattering is either an increase or a decrease in frequency of the scattered photons  $\pm \nu_{vib}$  in comparison with the incident frequency  $\nu_{ph_0}$ , which correspond to two different peaks at  $\nu_{ph} = \nu_{ph_0} \pm \nu_{vib}$  [61]. Raman spectroscopy uses a monochromatic light source and, what it actually measures, is a shift in frequency of the incident beam. In order to distinguish the Raman peaks from the dominant Rayleigh one, the frequencies close to the frequency of the incident laser need to be filtered out [60]. With the use of different notch filters, both Stokes and anti-Stokes scattering can be measured. Representing a shift in energy of the exciting radiation, Raman scattering is usually expressed in wavenumbers, that is defined as the reciprocal of the wavelength  $\omega = \frac{1}{\lambda}$  [ $cm^{-1}$ ] [60]. The shift, so the difference in energy between incident and scattered radiation, is expressed as [60]:

$$\Delta\omega = \frac{1}{\lambda_{Incident}} - \frac{1}{\lambda_{Scattered}} \quad (3.10)$$

A Raman spectrum represents the number of counts of scattered photons versus the wavenumber  $\omega$ .

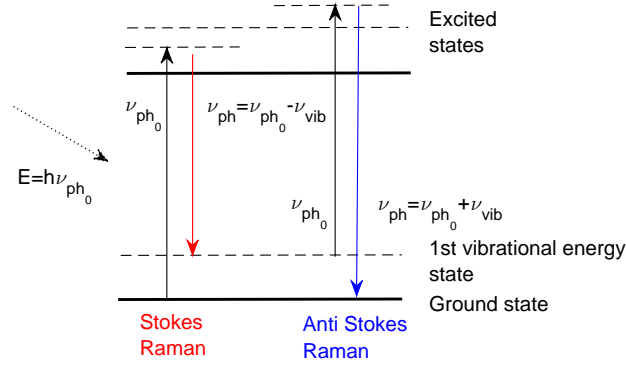


**Figure 3.2:** Schematic representation of Stokes and anti-Stokes Raman scattering phenomena

### Sample measurement

A Renishaw inVia Raman Microscope with an Argon laser is used, in this work, to perform Raman spectroscopy of the samples. The experimental settings were kept constant for each measurement and are summarized in table 3.3.

**Table 3.3:** Raman Spectroscopy measurements: specifications

|                                     |                      |          |
|-------------------------------------|----------------------|----------|
| <b>Excitation source wavelength</b> | [nm]                 | 514      |
| <b>Laser power</b>                  | [mW]                 | 25       |
| <b>Set power</b>                    | [%MaximumPower]      | 5        |
| <b>Lens magnification</b>           | [-]                  | 100×     |
| <b>Area of focus</b>                | [ $\mu\text{m}^2$ ]  | 1        |
| <b>Number of acquisitions</b>       | [-]                  | 1        |
| <b>Acquisition time</b>             | [s]                  | 400      |
| <b>Wavenumber range</b>             | [ $\text{cm}^{-1}$ ] | 100-3000 |

### IRFR

The Integrated Raman Fitting Routine (IRFR) is used to obtain information about the crystalline fraction of the material, together with the crystalline peak position. A four phonon mode contribution is used in IRFR for the amorphous phase in combination with a modified phonon confinement model to represent the crystalline phase [62]. The phonon modes of the amorphous phase are modeled as Gaussian distributions, while the phonon mode of the crystalline phase is described by a phonon confinement mode which represents the transverse optical (TO) mode of the crystalline phase [62]. The script fits the measurement to this model

and by integrating of the TO crystalline mode and the TO amorphous mode, it gives as an output the degree of crystallinity of the material calculated as:

$$X_C = \frac{I_{TO_{c-Si}}}{I_{TO_{c-Si}} + I_{TO_{a-SiO_x}}} \quad (3.11)$$

### Hydrogen content

From the Raman spectra it is also possible to qualitatively estimate the hydrogen content of the layers. In fact, the silicon hydrogen stretching modes show up in two different peaks between  $2000-2200 \text{ cm}^{-1}$  [55]. The lower stretching mode (LSM) corresponds to the Si-H bond and is found to be approximately  $2000 \text{ cm}^{-1}$ . The higher stretching mode (HSM) corresponds to the Si-H<sub>2</sub> bond and appears at higher wavenumbers, approximately  $2100 \text{ cm}^{-1}$ . In the Raman spectra, these two peaks usually overlap. It is possible to distinguish them by deconvoluting the broad peak in two Gaussian curves. The relative hydrogen content  $R_H$  is then calculated as [1]:

$$R_H = \frac{I_{LSM} + I_{HSM}}{I_{TO_{c-Si}} + I_{TO_{a-SiO_x}}} \quad (3.12)$$

These quantities are obtained by integrating the peaks of the Si-H stretching modes ( $I_{LSM}$  and  $I_{HSM}$ ) and the TO phonon modes of the amorphous ( $I_{TO_{a-SiO_x}}$ ) and the crystalline ( $I_{TO_{c-Si}}$ ) phases at  $485 \text{ cm}^{-1}$  and  $521 \text{ cm}^{-1}$  respectively. In order to be able to fit the Si-H peaks, the baseline needs to be removed from the Raman measurements. It can be fitted with a second order polynomial, which is then subtracted from the raw data in the range of interest ( $1900-2400 \text{ cm}^{-1}$ ) excluding the range where the peaks are expected ( $2000-2300 \text{ cm}^{-1}$ ).

### 3.2.3 Photothermal Deflection Spectroscopy

#### Setup

Photothermal deflection spectroscopy (PDS) is a powerful tool for the measurement of optical absorption of thin films for a range of wavelengths which spans between 300 and 3000 nm [63]. Its sensitivity allows the measurement of accurate values of absorbance down to the infrared region, which usually corresponds to the sub-gap region. These features make PDS very suitable for the characterization of amorphous and nanocrystalline silicon. In the PDS setup which is used during this work, the sample is mounted on a holder and immersed in a cuvette filled with perfluorohexane (Fluorinert FC-72) and it is illuminated by a monochromatic beam [64]. The light source is a white Xenon lamp, the beam (pump beam) is passed through a monochromator and then through a chopper after which it finally illuminates the sample. A second beam (probe beam), consists of a red laser aligned parallel to the sample, that just skims its surface. The portion of incident light which is absorbed by the sample is subsequently released through a relaxation process as heat. The thermal wave propagates through the FC-72, which is an inert and highly temperature-sensitive liquid. A time dependent increase of the medium temperature starts, resulting in a refractive index gradient, which results in a deflection from its original propagation direction of the red laser [65]. Two photodiodes measure this deflection up to values as small as  $10^{-9}$ - $10^{-10}$  rad [65]. The monochromatic light allows to record the absorption as a function of the incident photon energy [63]. In these measurements only the sample is assumed to absorb light with an absorption coefficient  $\alpha$  and the incident light is assumed to be uniform in wavelength. The deflection can then be expressed as a function, among other parameters, of the refractive index of the liquid  $n$ , the temperature of the sample surface and the thermal diffusivity of the liquid [65]. The PDS simultaneously measures absorbance ( $A$ ), reflectance ( $R$ ) and transmittance ( $T$ ), and it is important to note that these values are measured in the exact same spot [64]. When fitting the measurements, it is possible to correct for the resulting interference fringes if the thickness of the film and its refractive index  $n$  are known [64].

#### Sample measurement

The absorption measurements were carried out in a range of photon energy between 1 and 3.6 eV with intervals of  $\Delta E = 0.04$  eV from low to high energies and with a maximum of 20 measurements for each step. While fitting the measurements, the data with an instable phase ( $dA > 30$ ) were neglected. The fitting routine for the absorption coefficient as a function of the wavelength uses the Ritter-Weisser formula [64]. Each sample was measured as-deposited, after annealing at 500 °C and after annealing above  $T_{Crystallization}$ . The  $T$ ,  $R$  and  $A$  spectra were often calibrated by carrying out measurements with cuvette filled with FC-72, a sapphire sample and a carbon nanotubes sample, respectively.

#### Optical Models

Once the PDS measurement is completed, the raw data need to be processed in order to extract the characteristics of the a-SiO<sub>x</sub> and the embedded QDs. This is done by means of a fitting routine which is based on two different DOS models for the a-SiO<sub>x</sub> and the QDs.

Since the QDs and the dielectric matrix they are embedded in are physically separated, it is assumed impossible for electron transitions caused by illumination to happen between the two [1]. This means that the absorption coefficient of the composite material is the result of two different contributions which can be separately described.

Given the DOS of a semiconductor  $g$  and the Fermi-Dirac distribution  $f$ , both functions of the electron energy  $\epsilon$ , the absorption coefficient  $\alpha(E)$  is expressed as a function of the electron energy and the photon energy  $E$  [1]:

$$\alpha(E) = \frac{C}{E} \int g(\epsilon)f(\epsilon)g(\epsilon + E)[1 - f(\epsilon + E)]d\epsilon \quad (3.13)$$

Where  $C = 3.34 \times 10^{-38} \text{ cm}^5 \text{ eV}^2$  is a constant which takes into account the photon energy dependence of the refractive index and the matrix dipole moment. The models used to describe the contribution of the amorphous dielectric matrix and of the dots are described in the following sections.

- *Dielectric matrix*

The DOS of the intrinsic a-SiO<sub>x</sub> matrix is composed by the conduction band, the valence band and the defect density, as it is shown in figure 3.3 [66].

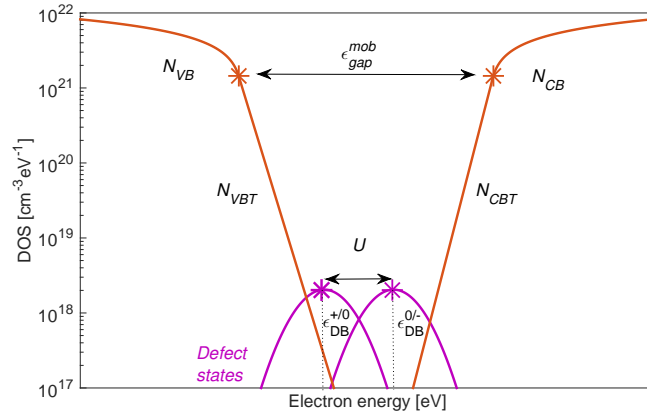


**Figure 3.3:** Schematic representation of a-SiO<sub>x</sub> DOS

The conduction band (CB) is in turn divided into extended states ( $N_{CB}$ ) and tail states ( $N_{CBtail}$ ), both function of the electron energy  $\epsilon$ . The same symmetrically applies for the valence band (VB) as:

$$\begin{aligned} N_{CB}(\epsilon) &= N^0 \sqrt{\epsilon - \epsilon_C} & N_{VB}(\epsilon) &= N^0 \sqrt{\epsilon - \epsilon_V} \\ N_{CBtail}(\epsilon) &= N_C^{tail} \exp \left[ - \left( \frac{\epsilon_C^{tail} - \epsilon}{\epsilon_{C_0}^{tail}} \right) \right] & N_{VBtail}(\epsilon) &= N_V^{tail} \exp \left[ - \left( \frac{\epsilon_V^{tail} - \epsilon}{\epsilon_{V_0}^{tail}} \right) \right] \end{aligned}$$

Where  $N^0$  represents the parabolic shape of the extended states of both bands.  $\epsilon_{C_0}^{tail}$  and  $\epsilon_{V_0}^{tail}$  account for the exponential trend of the tail states of the conduction and the

valence band, respectively.  $\epsilon_C^{tail}$  and  $N_C^{tail}$  are the connection point of extended and tail states. The expression for  $\epsilon_C = \epsilon_C^{tail} + \frac{1}{2}\epsilon_{C_0}^{tail}$  is found by solving a set of equations which imposes that both the *CB* and *CBT* DOS distributions and their derivatives are equal at their connection point. Again, the same holds for the valence band, where the connection point between extended and tail states is given by  $\epsilon_V^{tail}$  and  $N_V^{tail}$ . The difference between  $\epsilon_C^{tail}$  and  $\epsilon_V^{tail}$  is defined as the mobility gap  $\epsilon_{gap}^{mob}$ . Finally, the defect density of states is modeled by two Gaussian curves. They are shifted from each other by the correlation energy  $U$ .

In hydrogenated amorphous silicon the dominant source of defects are the dangling bonds contained in the film [66]. There are three charge states in which a dangling bond can be found: positive, negative or neutral. The possible charge transitions are therefore two:  $+/0$  (donor-like state) and  $0/-$  (acceptor-like state) and the two Gaussian distributions express their energy distribution of states through the following equations [66]:

Donor-like states:

$$N_{DB}^{+/0}(\epsilon) = \frac{N_{DB}^{tot}}{\sigma_{DB}\sqrt{2\pi}} \exp\left[-\frac{(\epsilon - \epsilon_{DB}^{+/0})^2}{2\sigma_{DB}^2}\right] \quad (3.14)$$

Acceptor-like states:

$$N_{DB}^{0/-}(\epsilon) = \frac{N_{DB}^{tot}}{\sigma_{DB}\sqrt{2\pi}} \exp\left[-\frac{(\epsilon - \epsilon_{DB}^{0/-})^2}{2\sigma_{DB}^2}\right] \quad (3.15)$$

Donor and acceptor-like states are related to each other through the correlation energy  $U$  as:

$$N_{DB}^{0/-}(\epsilon) = N_{DB}^{+/0}(\epsilon + U) \quad (3.16)$$

Where  $N_{DB}^{tot}$  is the total defect density,  $\sigma_{DB}$  is the width of the Gaussian,  $\epsilon_{DB}^{+/0}$  and  $\epsilon_{DB}^{0/-}$  are the energy levels of  $N_{DB}^{+/0}$  and  $N_{DB}^{0/-}$ , respectively. Finally, the Fermi level is calculated by solving the following equation for a given density of states:

$$\int g_{CB} f d\epsilon = \int g_{VB} (1 - f) d\epsilon \quad (3.17)$$

This is possible because, since the material we are considering is an intrinsic semiconductor, the electron density in the conduction band is approximately equal to the hole density in the valence band.

- *Quantum dots*

Modeling the DOS distribution of QDs should take into account quantum confinement (QC) effects, which produce a discretization of the available states and restricts the absorption window to narrow photon energy bands [5]. According to density functional theory calculations, the allowed energy states vary depending on the squared quantum number  $n$ . However, there are several factors which increase their density [5]. For example, 3D confinement introduces numerous energy solutions, which are associated with allowed optical transitions between states. Due to proximity between dots, each allowed

state broadens into a band which depends on the spacing between the dots. Moreover, even if according to Yi et al. the deposition of ordered  $\text{SiO}_x/\text{SiO}_2$  superlattices allows size controlled Si QDs synthesis [67], the size of the QDs is still subjected to a dispersion. This causes additional overlapping of the wave functions and so of the allowed and not-allowed energy states [5]. To these considerations is to be added that, what is under analysis in this report, are QDs composed by thousands of atoms with an expected diameter  $d \geq 2$  nm. As reported by E. Ramos et al. [68], in clusters composed by up to 239 Si atoms, the lowest optical transitions have energies above 3 eV, clearly showing QC effects, but for crystals with diameter above 1.5 nm the first bulk-like properties appear. In conclusion, what we are dealing with can be regarded as semi-continuous DOS distributions of allowed optical transition energies for the electrons between valence and conduction bands [5].

M. van Seville et al. [1] proposed a model to describe the density of state for QDs which is composed by two Gaussian distributions (see figure 3.4):  $N_{QD}^{HOS}$  for the highest occupied states and  $N_{QD}^{LUS}$  for the lowest unoccupied states.

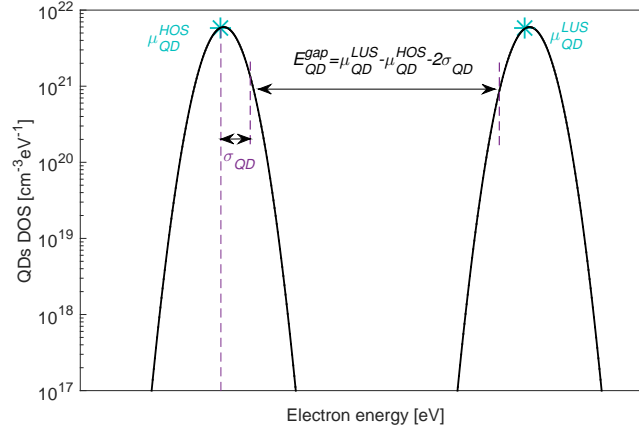


**Figure 3.4:** Schematic representation of c-Si QDs DOS

The overall DOS of the QDs is given by the sum of the two distributions as:

$$N_{QD}(\epsilon) = N_{QD}^{HOS} + N_{QD}^{LUS} \quad (3.18)$$

$$\begin{cases} N_{QD}^{HOS}(\epsilon) = \frac{N_{QD}^0}{\sigma_{QD}\sqrt{2\pi}} \exp\left[-\frac{(\epsilon - \mu_{QD}^{HOS})^2}{2\sigma_{QD}^2}\right] \\ N_{QD}^{LUS}(\epsilon) = \frac{N_{QD}^0}{\sigma_{QD}\sqrt{2\pi}} \exp\left[-\frac{(\epsilon - \mu_{QD}^{LUS})^2}{2\sigma_{QD}^2}\right] \end{cases} \quad (3.19)$$

The amplitude and the standard deviations of the Gaussians are  $N_{QD}^0$  and  $\sigma_{QD}$ , respectively. While  $\mu_{QD}^{HOS}$  and  $\mu_{QD}^{LUS}$  are the means of the highest occupied states and of the lowest unoccupied states, respectively. Being  $\epsilon_F$  the Fermi level, they are calculated as:

$$\mu_{QD}^{HOS} = \epsilon_F - \frac{1}{2}E_{QD}^{gap} \quad (3.20)$$

$$\mu_{QD}^{LUS} = \epsilon_F + \frac{1}{2} E_{QD}^{gap} \quad (3.21)$$

The band gap of the QDs is defined as:

$$E_{QD}^{gap} = \mu_{QD}^{LUS} - \mu_{QD}^{HOS} - 2\sigma_{QD} \quad (3.22)$$

The two distributions contain information about properties of the QDs. As shown in figure 3.4, the difference in energy between the two Gaussians is used to define the band gap of the QDs, the standard deviation of the QD DOS also implies a size standard deviation. In fact, since the QDs energy band gap and their size are strongly correlated, as shown in equation 2.8, a variation in energy band gap is due to a variation in size. During this work, the DOS standard deviation  $\sigma_{QD}$  is used as a measure of the size dispersion of the QDs in the amorphous matrix. The integrated lowest unoccupied QD states is related to the total number of QD states present in the sample volume [1].

To be noted is that this model is assumed to be valid for QDs formed by hundreds to thousands of atoms, whose DOS distribution can be described by semi-continuous energy bands. This condition can be assumed to be respected in our work, where the expected size of the QDs is kept between 2 and 5 nm. For the smaller crystals that might form in the film, QC produces discrete energy levels [5] and in this case the model described above is not accurate for their DOS description.

According to the fabrication procedure followed during this work, after deposition the samples are annealed at two different temperatures. The lower (500 °C) is used to obtain a dehydrogenated material, the higher (1000 °C) is used to attain QDs formation in the film. What is of greatest interest for this section is the correlation, in terms of absorption coefficient spectra, between hydrogen-free and crystallized materials. When, upon high temperature annealing, the material separates into amorphous and crystalline phase, no changes in the composition of the material occur <sup>2</sup>. The evolution induced by crystallization only concerns the atomic structure of the material. So, the only difference which occurs between the two materials is considered to be the presence of the QDs themselves. The difference in shape of the absorption coefficient spectra shown in figure 3.5, is therefore completely attributed to the QDs.

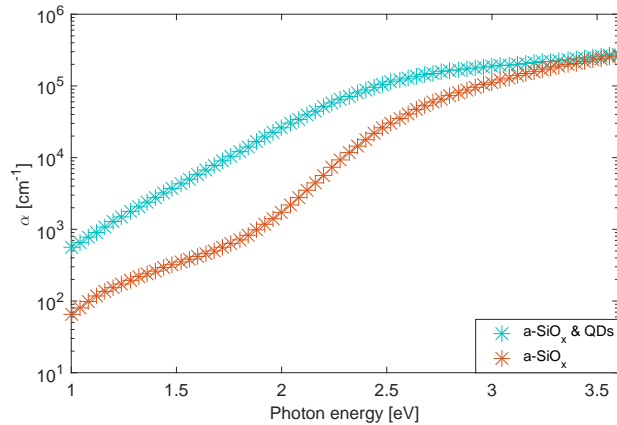


**Figure 3.5:** Absorption coefficient  $\alpha(\lambda)$  spectra of an hydrogen-free a-SiO<sub>x</sub> film and a crystallized film

<sup>2</sup>Hypothesis confirmed by XPS measurements on both types of samples at TU Eindhoven

In the area of the spectrum which corresponds to photon energies much higher than the materials' band gap, the absorption coefficient spectra almost coincide. Moving to lower energy values the presence of QDs causes a sharp increase in absorption in correspondence of their band gap. This enhancement in absorption continues also in the tail states and defect states.

Using formula 3.13 to correlate  $\alpha(\lambda)$  and the DOS models proposed above, it is possible to extract from the absorption spectra measurement information about the QDs' optical properties.

### Measurement fitting

The same fitting procedure as that reported by van Sebillie et al. was followed [1]. In a first place the absorption coefficient of as deposited a-SiO<sub>x</sub>:H samples were measured and the raw data were fitted. The DOS parameters described in section 3.2.3 ( $\epsilon_{DB}$ ,  $N_{DB}^{tot}$ ,  $\sigma_{QD}$ ,  $U$ ,  $N^0$ ,  $\epsilon_{C_0}^{tail}$ ,  $\epsilon_{V_0}^{tail}$ ,  $\epsilon_{gap}^{mob}$ ) were used as free fit parameters. This procedure allowed the extraction of the amorphous matrix DOS characteristics. The second step consisted in the measurement of dehydrogenated samples. Since the effusion of hydrogen causes the defect density of the material to greatly increase,  $N_{DB}^{tot}$  was used as a free fit parameter.  $\epsilon_{DB}$ ,  $U$  and  $\sigma_{DB}$  were kept constant. The third step regarded the extraction of optical properties of sample after crystallization. From literature it was known that no remarkable variations in the amorphous matrix and in the defect density occur after crystallization [1], this was also evinced from our experiments. So, the annealed samples were fitted by keeping constant  $\epsilon_{C_0}^{tail}$ ,  $\epsilon_{V_0}^{tail}$ ,  $\epsilon_{gap}^{mob}$  for the amorphous matrix and  $\epsilon_{DB}$ ,  $\sigma_{QD}$ ,  $U$  for the defects. In this case the free fit parameters were  $N^0$  and  $N_{DB}^{tot}$ . In fact, upon crystallization, a decrease of the number of silicon atoms in the amorphous phase causes a decrease of the the amorphous DOS. Moreover, it was reported that an increase in annealing temperature leads to a defect healing process, which causes the defect density to decrease [51].

### 3.2.4 X-Ray Photoelectron Spectroscopy

X-ray photoelectron spectroscopy (XPS) is a powerful tool for the determination of the elemental composition of a material. It is widely used in nanomaterials and in photovoltaic technology characterization processes. The analysis is done at superficial level. By repeatedly etching away the top layer, it is possible to obtain depth profiles of the material. The working principle of this setup is the detection of core electrons that, when hit by sufficiently energetic x-rays, absorb enough energy to exceed the binding energy and are emitted as photoelectrons from the sample surface [69]. An electron energy analyzer is used to measure the kinetic energy of the photoelectrons, which is related to the photon energy as:

$$E_{Photon} = h\nu = E_{Kinetic} + E_{Binding} + \phi \quad (3.23)$$

The XPS spectrum is formed by counting the number of emitted photoelectrons at each kinetic energy. Since each chemical bond is characterized by a certain binding energy, the positions of the peaks reveal the components of the film. The area and the intensity of the peaks allow to quantify their presence [69]. These measurements were carried out at the chemistry department of TU Eindhoven.



---

## Chapter 4

---

# Results & Discussion

In this chapter the experimental results obtained during this work are presented. The chapter is structured in two parts which correspond to the two furnaces used during this work: the Carbolite and the RTA furnaces.

In section 4.1, the results obtained from the first furnace are presented. They are divided in low and in high annealing temperature. The former, where the temperature is varied between 400 and 500 °C, deals with the investigation of hydrogen effusion from the film as a function of temperature. The latter regards annealing at temperatures between 900 and 1075 °C. This section was meant to observe the crystallization of samples with different Si-rich layer thicknesses and the evolution of QDs of different sizes as a function of temperature.

The discussion proceeds, from section 4.2.1, with the description of the results obtained from RTA experiments. This section is divided into five parts. The first (see 4.2.1) deals with the effect different annealing atmospheres have on hydrogen effusion from the films (and so annealing induced defect generation) and on their crystallization. The two annealing environments that are investigated are forming gas (FG) and pure nitrogen gas. From this first experiment it was chosen to proceed with annealing in FG. In the second experiment the influence of silicon content in the Si-rich layers is studied in section 4.2.2. From this section a recipe for the deposition of Si-rich layer was chosen and used throughout the rest of the work. What is analyzed next, in the third part, is the influence of annealing temperature on crystallization of the samples and on the QDs properties (see section 4.2.3). The fourth experiment, which is reported in section 4.2.4, is aimed to investigate the influence annealing time has on the samples. The procedure was carried out for three different temperatures and increasing the annealing time, first in FG and, in a second moment, in nitrogen gas. This was done because, interestingly, the evolution of QDs properties was found to be completely different in the two annealing environments. The results relative to the two annealing atmospheres are shown in parallel. Two possible explanations to what is observed are offered in section 4.2.4. The fifth part of the RTA section deals with the investigation of the role played by different Si-rich layer thicknesses in the evolution of QDs properties. A brief discussion follows each of the sections described above.

## 4.1 Carbolite furnace annealing

The purpose of this set of experiments was the investigation of the evolution of optical properties of our samples upon hydrogen effusion and crystallization when annealed in a nitrogen purged furnace.

In this section samples with different Si-rich layer thickness were fabricated. The deposition gas flow rates for the layers are those reported in table 4.1.

**Table 4.1:** Gas flow rates for the deposition of Si-rich and SiO<sub>2</sub> layers.

| Layer            | SiH <sub>4</sub> [sccm] | CO <sub>2</sub> [sccm] | H <sub>2</sub> [sccm] |
|------------------|-------------------------|------------------------|-----------------------|
| Si-rich          | 8                       | 48                     | 0                     |
| SiO <sub>2</sub> | 1                       | 55                     | 0                     |

The silicon content of the former is 66 % and the oxygen content of the latter is 66 %. The depositions were made on quartz substrates. The structure was, for each sample, an a-SiO<sub>x</sub>/SiO<sub>2</sub> superlattice of 20 periods. By varying the deposition time of the of the a-SiO<sub>x</sub> layer its thickness was, approximately, 2, 3, or 4 nm. The thickness of the SiO<sub>2</sub> layers was of about 2.7, 2 and 1.35 nm, respectively.

### Hydrogen effusion

In this experiment the hydrogen effusion from the film was studied as a function of increasing annealing temperature. Samples of all three thicknesses described above were annealed for 30 min at increasing temperature (from 400 to 500 °C, with intervals of 25 °C).

In figure 4.1, the trend of energy band gap and the relative hydrogen content of the samples upon hydrogen effusion are shown.

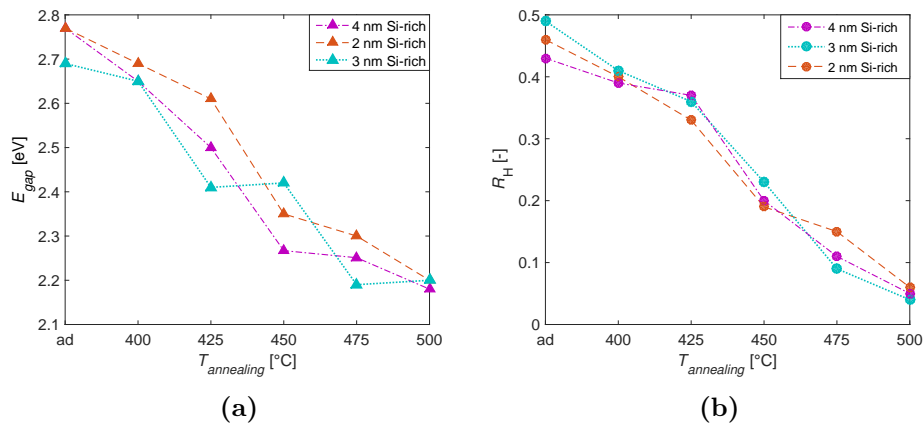


**Figure 4.1:** Energy band gap (a) and relative hydrogen content (b) of samples as-deposited and annealed from 400 to 500 °C for 30 min.

The energy band gap values are those measured with Spectroscopic Ellipsometry measurements (Cody-Lorentz model was used). The relative hydrogen content  $R_H$  was obtained from

Raman spectroscopy measurements by using formula 3.12.

For each Si-rich layer thickness the same trend is observed and it is in accordance with theory [70]. The band gap of the material decreases proportionally to the effusion of hydrogen from the film.

For annealing at 500 °C, a full effusion of hydrogen is obtained. The calculated relative hydrogen content is not completely null. This can be explained by the fact that its value is calculated as the ratio between two Raman modes. Due to some noise in the measurement, the area below the curve of the Raman spectrum is never zero. From figure 4.2 though, it is visible that the peak between 2000 and 2200  $\text{cm}^{-1}$  completely flattens out.

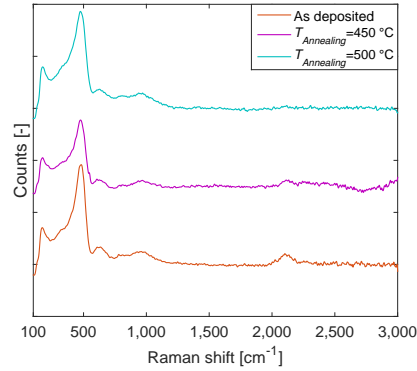


**Figure 4.2:** Raman spectra of samples as-deposited and annealed for 30 min at 450 and 500 °C

The value of the absorption coefficient  $\alpha$  at 1.5 eV is taken as a measure of the sub-gap defect related absorption of the material. Upon hydrogen effusion, as mentioned in section 2.2.1, the defect density strongly increase as effused H atoms leave bonds in the film.

From each sample the absorption coefficient is measured before and after hydrogen effusion, its value at 1.5 eV is reported in table 4.2.

**Table 4.2:** Absorption coefficient at 1.5 eV of as-deposited and dehydrogenated samples with different Si-rich layer thickness.

| Si-rich layer thickness [nm] | $\alpha_{AsDeposited} [cm^{-1}]$ | $\alpha_{Dehydrogenated} [cm^{-1}]$ |
|------------------------------|----------------------------------|-------------------------------------|
| 2                            | 40                               | 293                                 |
| 3                            | 52                               | 252                                 |
| 4                            | 44                               | 305                                 |

## Crystallization

The aim of this section was the investigation of the crystallization and of the evolution of QDs properties as a function of the annealing temperature. Samples of all the three Si-rich layer thicknesses described above were annealed for 30 min at increasing temperature (from 900 to 1075 °C, with intervals of 25 °C).

The annealing series was repeated with both procedures described in section 3.1.3.

What was found from the two series of experiments is that, when the samples are annealed at such temperatures a thick over layer of thermal oxide grows on the films. The thickness of the grown layer varies, depending on the initial thickness of the layer and on the annealing temperature, between 36 and 65 nm.

Moreover, it was not possible to obtain a good fit of the SE measurements with any of the models available. This means that the extraction of QDs characteristics, which is done through absorption coefficient measurements and fit with SE data, became impossible.

This made the samples unusable and the Carbolite nitrogen purged furnace unsuitable for the purpose of this work.

## Discussion

From this set of experiment it was possible to analyze the hydrogen effusion process as a function of annealing temperature. It was found that it starts at approximately 400 °C and the film reaches full dehydrogenation at  $T_{Annealing}=500$  °C.

It was also found that the absorption coefficient at a photon energy of 1.5 eV, as expected, strongly increases after annealing, indicating an increase in defect density in the material.

Unfortunately it was not possible to proceed in QDs fabrication and characterization, as high temperature annealing induced an oxidation of the samples which made them not usable.

## 4.2 Rapid thermal annealing furnace

### 4.2.1 Influence of annealing atmosphere

In this section a comparison between two annealing atmospheres is described. The two environments we tested are pure nitrogen and forming gas (10% hydrogen and 90% nitrogen). The purpose of this part of experiments is investigating the evolution of the optical properties of the samples upon hydrogen effusion and crystallization of the silicon-rich layers in different environments. The samples used in these experiments were all obtained from the same deposition batch. The configuration is 4-nm thick silicon-rich followed by 1-nm thick silicon dioxide, repeated for 35 periods, deposited on a quartz substrate. The silicon content of the silicon-rich layers is 65.2%<sup>1</sup>. The annealing procedure is summarized in table 4.3.

**Table 4.3:** Annealing conditions for chapter 4.2.1.

| Sample | $t_{\text{Annealing}}$ [min] | $T_{\text{Annealing}}$ [°C] | Atmosphere     | Gas flow [slm] |
|--------|------------------------------|-----------------------------|----------------|----------------|
| 1      | 3                            | 500                         | Forming Gas    | 8              |
| 2      | 3                            | 500                         | N <sub>2</sub> | 8              |
| 3      | 3                            | 1000                        | Forming Gas    | 8              |
| 4      | 3                            | 1000                        | N <sub>2</sub> | 8              |

### Hydrogen effusion

Very little difference is present between the dehydrogenated samples and the crystallized ones, apart from the presence of the QDs themselves [1]. This difference is visible in the absorption spectra of the samples, which are the starting point for the optical analysis. It is important therefore, to understand under which annealing conditions the films are completely dehydrogenated.

Samples 1 and 2 were annealed at 500 °C. From previous experiments (see section 3.1.3) and from literature [71] this temperature was expected to be sufficient to obtain complete effusion of hydrogen from the film. The annealing time was 3 min. Applying formula 3.12, the relative hydrogen content is 0.53 for the as-deposited sample. For sample 2, the Si-H peak disappears upon annealing, showing that the relative hydrogen content in the layers drops to zero and indicating a complete dehydrogenation, as shown in figure 4.3-b. The same can not be said for sample 1, as shown by the Raman spectra of the sample before and after annealing in figure 4.3-c. After a 3 min long annealing the Si-H peak, even if it has evidently decreased in intensity, is still present. The calculated relative hydrogen content is now 0.11. A complete flattening of the Si-H modes is obtained, in forming gas atmosphere, when the annealing time is doubled.

<sup>1</sup>Value obtained from XPS measurements carried out at TU Eindhoven

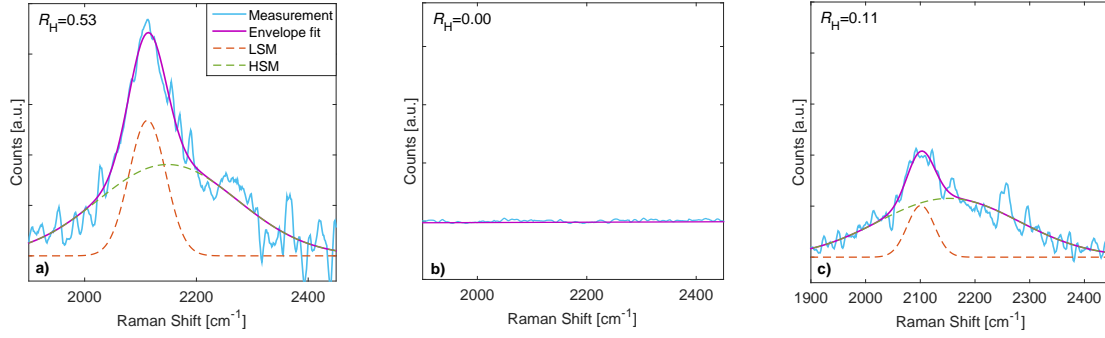


**Figure 4.3:** Raman spectra comparison: LSM and HSM peak fitting and relative hydrogen content of samples annealed in different atmospheres. (a) As deposited. Annealed at 500 °C for 3 min (b) in N<sub>2</sub> (sample 2). and (c) in FG (sample 1).

As explained in section 2.2.1, the effusion of hydrogen from the matrix causes an increase in the defect density of the material, as each effusing H atom leaves a dangling bond behind. A comparison of the absorption spectra of the two samples provides information about the density of sub-gap defect related states.

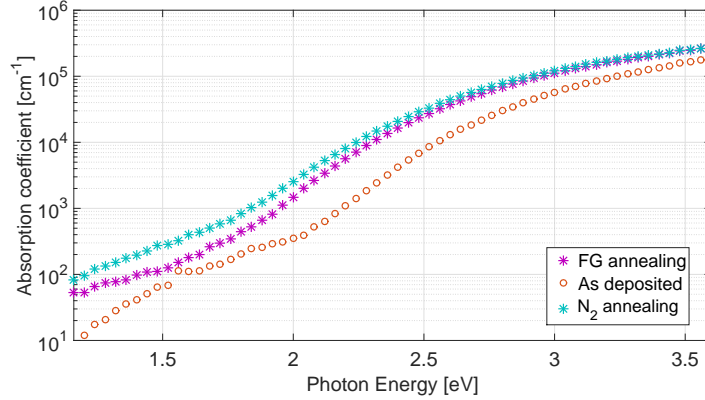


**Figure 4.4:** Comparison of  $\alpha(\lambda)$  spectra of an as-deposited sample, sample 1 ( $t_{\text{Annealing}}=6$  min) and sample 2 ( $t_{\text{Annealing}}=3$  min) at 500 °C.

As can be seen from figure 4.4 in both cases the absorption in the low-energy range (related to defects) increases with respect to the as-deposited sample. In the high energy range (related to optical transitions to and from extended states) the two curves almost overlap. While, below 2.5 eV, the two curves start diverging. The value of absorption coefficient at 1.5 eV can be used as a measure of sub-gap absorption. The ratio between the values of the two samples annealed in N<sub>2</sub> and in FG, respectively, is  $\left[ \frac{\alpha(1.5\text{eV})_{\text{N}_2}}{\alpha(1.5\text{eV})_{\text{FG}}} \right] = 2.24$ . The annealing in forming gas leads, after hydrogen effusion, to a material with a lower defect density with respect to annealing carried out in nitrogen gas atmosphere.

## Crystallization

The second part of this section consists of a comparison of the two annealing atmospheres upon silicon crystallization. From literature [72] and from previous experiments it was known that a temperature of 1000 °C and an annealing time of 3 min would be sufficient to obtain partial crystallization of the samples.

Also in this case a comparison of the absorption spectra gives information about the characteristics of the material.

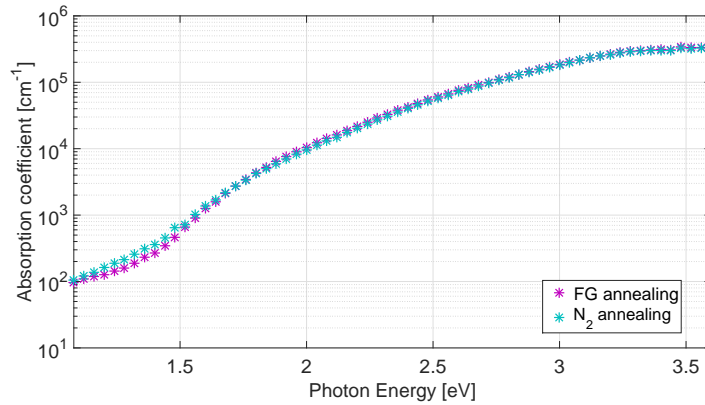


**Figure 4.5:** Comparison of  $\alpha(\lambda)$  spectra of sample 3 (annealed in FG) and sample 4 (annealed in  $N_2$  at 1000 °C for 3 min).

In the spectral range related to extended states the two curves are overlapping as well as in the tail states area. In the spectral range related to defects (below 1.5 eV), the curves slightly diverge. Also in this case the value of absorption coefficient at 1.5 eV is taken as a measure of defect-related absorption:  $\left[ \frac{\alpha(1.5\text{eV})_{N_2}}{\alpha(1.5\text{eV})_{FG}} \right] = 1.11$ . Also in this case the forming gas atmosphere leads to a lower defect density for high temperature annealing. In figure 4.5 it is possible to see, between 1.6 eV to 2 eV the absorption enhancement related to the presence of QDs. For what concerns the crystallization process, the results are comparable as shown in figure 4.6 by the Raman spectra and by the crystalline fraction calculation. By fitting the  $\alpha(\lambda)$  spectra of samples 3 and 4 it is then possible to extract information about the QDs.

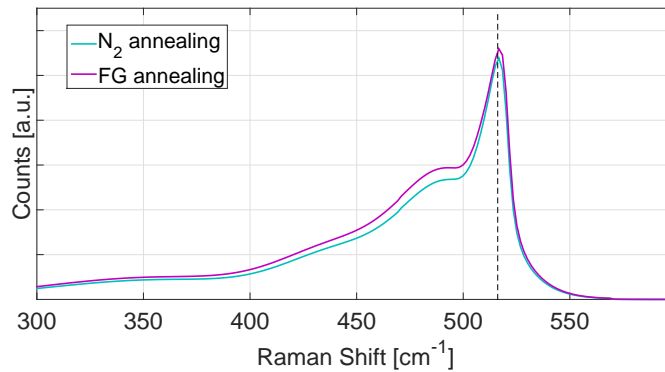


**Figure 4.6:** Comparison of Raman spectra of samples annealed at 1000 °C for 3 min in  $N_2$  and in FG.

**Table 4.4:** QDs characteristics evolution as a function of annealing atmosphere.

| Sample | Ann. atmosphere | $E_{QD}^{gap}$ [eV] | $\sigma_{QD}$ [eV] | $I_{QD}$ [ $\text{cm}^{-3}$ ] | MSE [-] | $X_c$ [%] |
|--------|-----------------|---------------------|--------------------|-------------------------------|---------|-----------|
| 3      | FG              | 2.51                | 0.133              | $2.37 \times 10^{20}$         | 0.0169  | 32.7      |
| 4      | $\text{N}_2$    | 2.12                | 0.134              | $3.18 \times 10^{20}$         | 0.0182  | 31.6      |

Even though the crystallinity values of samples 3 and 4 are comparable, from what is reported in table 4.4 the two annealing atmospheres lead to different QDs characteristics. Sample 3 shows a higher  $E_{QD}^{gap}$  and a lower integrated QD DOS. Meaning that, possibly, the QDs formed in sample 3 are slightly smaller and they have a lower density. However, since crystallinity is a measure of the QD states density, this result is unexpected. Crystallinity and  $I_{QD}$  are supposed to be proportional, this discrepancy might be due to a lack in uniformity of the film and its properties, or inaccuracy of the measurement.

## Discussion

In this section the effect of different annealing conditions on samples from the same batch were investigated. The first part of the experiment dealt with the hydrogen effusion in samples annealed at 500 °C and for 3 min in FG (sample 1) and in nitrogen gas (sample 2). For the latter sample complete dehydrogenation was obtained after the annealing while, for the former, a relative hydrogen content of  $R_H=0.11$  was still found. Annealing in FG required a longer annealing time, in fact, complete hydrogen effusion was obtained only after 6 min. A difference in absorption for the dehydrogenated samples was also found. The ratio of absorption coefficient values of sample 2 and sample 1 at 1.5 eV, is 2.24.

Upon crystallization samples 3 and 4 show similar behaviour. The ratio of absorption coefficients at 1.5 eV decreases to 1.11 and they both reach a crystallinity of approximately 30%.  $I_{QD}$  is lower for sample 3.

In conclusion, annealing in forming gas shows to lead to a slower hydrogen effusion from the matrix, and the passivating effect of hydrogen leads to a lower defect density. On the other hand the density and the size of the QDs in sample 3 may be smaller.

### 4.2.2 Influence of silicon content

As mentioned in section 3.1.2, by varying the flow rates of the components of the gas mixture it is possible to obtain films with different composition. This leads to different properties of the material and different behaviour upon hydrogen effusion and crystallization. As reported by Zacharias et al. [34], the stoichiometry of the silicon-rich layer determines the density of QDs and the spacing between them within the layer itself. For a given thickness, the higher the excess silicon, the higher the dot density, the lower the spacing. For c-Si QDs embedded in  $\text{SiO}_2$ , where the band offset between the crystals and the host matrix is very wide (7.9 eV [42]) and the spacing between dots should not be larger than 1-2 nm for tunneling transport to be possible, it is crucial to achieve the highest possible crystallinity. On the other hand, it was also observed in literature [73], that in a-SiN:H there are charge trap centers due to silicon dangling bonds, which increase as the material becomes more silicon-rich. The presence of these dangling bonds is attributed to the incorporation of N atoms in the film and to the small covalent-bond radius of N atoms with respect to that of Si atoms. As the covalent-bond

radii of nitrogen and oxygen (71 and 76 pm, respectively [74]) are quite close, this might occur in a-SiO<sub>x</sub> samples as well. Also, in order to obtain a denser and less defective material, it is desirable to maintain a high hydrogen dilution [53]. On the other hand, too high dilution can lead to a very slow or also absent deposition. Obtaining the highest crystalline fraction and the least defective material possible are part of the objectives of this work. It is worth, therefore, to investigate the evolution of both defect and crystallinity evolution depending on the silicon content of the silicon-rich film. Several recipes were experimented, here we report only the more significant.

The sample structure was, also in this case, an a-SiO<sub>x</sub>/SiO<sub>2</sub> superlattice of 35 periods, deposited on a quartz substrate. The silicon-rich and the silicon dioxide layers have a thickness of 4 nm and 1 nm, respectively. Three different samples were deposited, using the three deposition recipes reported in table 4.5. With respect with the recipe used in the previous section (4.1) the biggest difference is hydrogen dilution. This choice was made to obtain a denser material with a lower defect density. Several recipes were initially experimented and from SE measurements it was possible make an estimation of the silicon content of the material. Too high hydrogen dilution led to no deposition and those recipes were obviously discarded. The three recipes with highest silicon content were finally chosen, and their composition was precisely determined via XPS measurements performed at TU Eindhoven.

**Table 4.5:** Deposition conditions for silicon-rich layers and relative silicon content

| Sample | SiH <sub>4</sub> [sccm] | CO <sub>2</sub> [sccm] | H <sub>2</sub> [sccm] | Silicon content [%] |
|--------|-------------------------|------------------------|-----------------------|---------------------|
| 1      | 10                      | 27                     | 200                   | 78.1                |
| 2      | 10                      | 80                     | 200                   | 65.2                |
| 3      | 2.5                     | 9.5                    | 200                   | 57.9                |

## Hydrogen effusion

Similar to what was explained in section 4.2.1, also in this case the first step consisted in evaluating the behaviour of samples 1, 2 and 3 upon hydrogen effusion. The samples were annealed in RTA furnace, in FG atmosphere at 500 °C. Given the results of the previous experiment, the annealing durations were kept at 3 min and 6 min. The procedure was repeated on two sets of samples.

Also in this case, for all the three samples, hydrogen starts effusing during the shorter annealing step which though, is not sufficient for a full dehydrogenation (see figure 4.7). What is observed is that the monohydrides and the polyhydrides leave the amorphous silicon matrix differently. In fact, after the annealing step of 3 min, the lower stretching mode decreases considerably in intensity. On the other hand, the higher stretching mode is only slightly influenced.

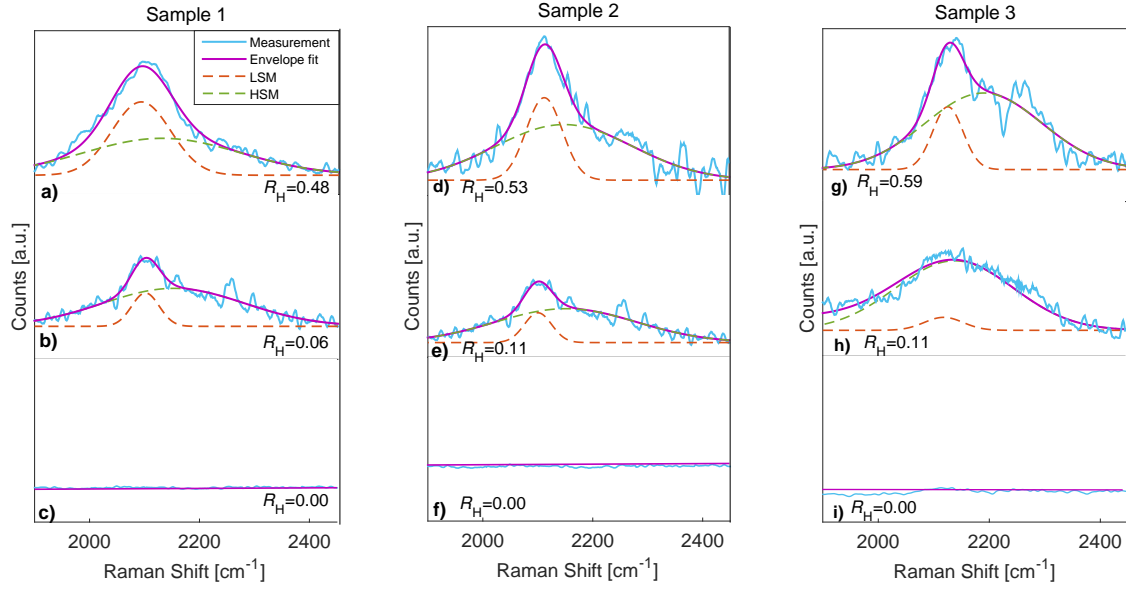


**Figure 4.7:** LSM and HSM peak fitting and relative hydrogen content of samples with different Si content. (a), (d), (g) As deposited. (b), (e), (h) Annealed at 500 °C for 3 min in FG, (c), (f), (i) Annealed at 500 °C for 6 min in FG.

After annealing for 6 min both the LSM and the HSM peaks completely disappear, showing a full hydrogen effusion from the matrix.

The absorption coefficient was measured and its value at 1.5 eV was used in order to compare defect related absorption (see figure 4.8 and table 4.6). The measurement is repeated for the as-deposited and for the fully dehydrogenated samples.

Sample 2 and 3 show similar absorption values both for the as-deposited and for the annealed case. What can be evinced is that sample 1 shows a much lower absorption for the annealed case. This indicates a lower defect related absorption for the sample with highest silicon content and lowest relative hydrogen content  $R_H$ .

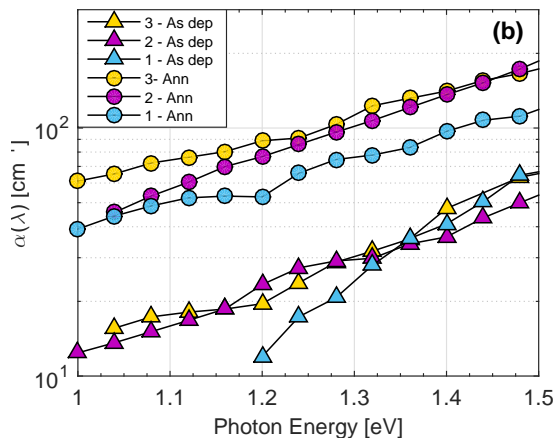


**Table 4.6: (b)**

| Sample | $\alpha_{1.5eV_{Asdep}}$ [cm <sup>-1</sup> ] | $\alpha_{1.5eV_{Ann}}$ [cm <sup>-1</sup> ] | Si [%] |
|--------|--|--|--------|
| 1      | 64.54  | 111.6                                      | 78.1   |
| 2      | 50.02  | 165.3                                      | 65.2   |
| 3      | 67.72  | 172.3                                      | 57.9   |

**Figure 4.8:** (a) Absorption coefficient  $\alpha(\lambda)$  and (b)  $\alpha$  at 1.5 eV for samples 1, 2 and 3, as-deposited and annealed at 500 °C for 6 min.

## Crystallization

The second part of this section deals with the comparison of the above mentioned deposition recipes upon silicon crystallization. For each of the three recipes one as-deposited sample was annealed at a temperature of 1000 °C for a duration of 3 min. A comparison among absorption coefficient spectra is shown in figure 4.9:

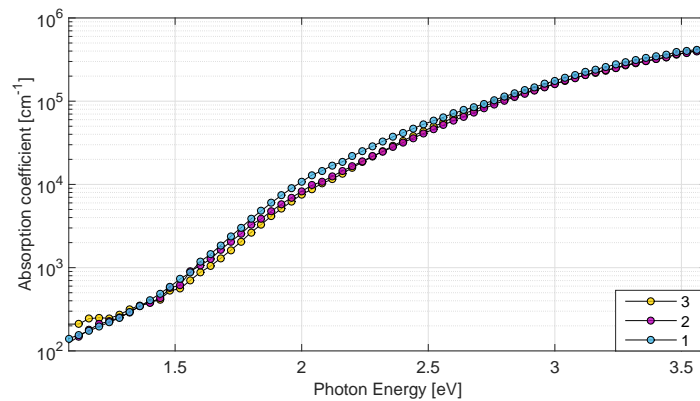


**Figure 4.9:** Comparison of  $\alpha(\lambda)$  spectra: samples 1, 2 and 3 annealed at 1000 °C for 3 min in FG

The absorption coefficient curves almost overlap for photon energies above 2.5 eV, showing no significant differences. Between 1.5 eV and 2.5 eV, where the shoulder due to QDs absorption is visible, sample 1 shows a higher  $\alpha(\lambda)$  value. In the sub-gap region, below 1.5 eV, the curves of samples 1 and 2 are hardly possible to distinguish meaning that, upon crystallization, the materials have comparable defect densities. Sample 3 shows slightly higher absorption in this range. The stronger absorption from the QDs is confirmed by the results of Raman spectroscopy measurements. In fact, as shown in table 4.7, sample 1 reaches a significantly higher crystallinity with respect to the other two samples.

**Table 4.7:** Crystallinity of samples 1, 2 and 3 after annealing in FG at 1000 °C for 3 min.

| Sample | Crystallinity [%] | Si content [%] |
|--------|-------------------|----------------|
| 1      | 28.26             | 78.1           |
| 2      | 19.27             | 65.2           |
| 3      | 16.13             | 57.9           |

Additional confirmation is found when fitting the absorption spectra of the samples. The results are summarized in tale 4.8.

**Table 4.8:** QDs evolution as a function of silicon content

| Sample | $E_{QD}^{gap}$ [eV] | $\sigma_{QD}$ [eV] | $I_{QD}$ [ $\text{cm}^{-3}$ ] | MSE [-] | Si content % |
|--------|---------------------|--------------------|-------------------------------|---------|--------------|
| 1      | 2.01                | 0.129              | $3.61 \times 10^{20}$         | 0.0194  | 78.1         |
| 2      | 2.49                | 0.162              | $2.41 \times 10^{20}$         | 0.0152  | 65.2         |
| 3      | 2.63                | 0.233              | $1.970 \times 10^{20}$        | 0.0171  | 57.9         |

The trend in crystallinity is confirmed by the values of integrated QD DOS, the density of QDs states increases with increasing silicon content in the as-deposited a-SiO<sub>x</sub> layer. From figure 4.10 an almost linear trend is visible between the silicon content, the crystallinity and  $I_{QD}$ .

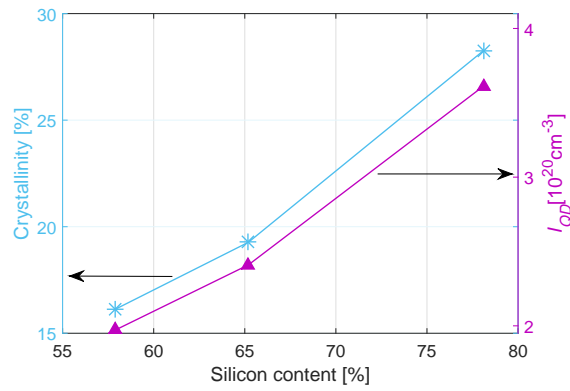


**Figure 4.10:** Integrated QDs DOS (right axis) and crystallinity (left axis) as a function of silicon content in the as-deposited samples, after annealing at 1000 °C for 3 min in FG atmosphere.

Also for what concerns the QD energy band gap a clear trend is visible as a function of the silicon content of as-deposited samples (see figure 4.11).

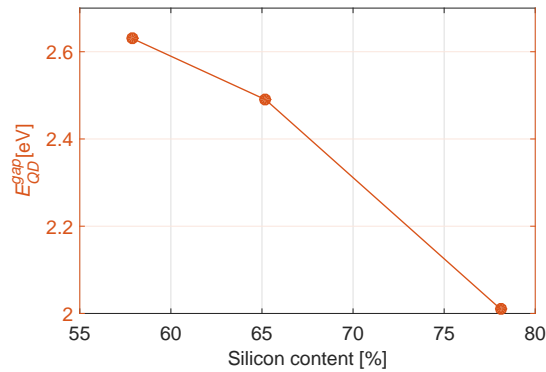


**Figure 4.11:** QD energy band gap as a function of silicon content in the as-deposited samples, after annealing at 1000 °C for 3 min in FG atmosphere.

For samples 2 and 3  $E_{QD}^{gap}$  is considerably higher than for sample 1. This might be explained

by the fact that, according to nucleation theory, the formation of QDs starts from very small nuclei [34], which then grow larger. The growth stops either when their diameter reaches the thickness of the silicon-rich layer or when all the excess silicon separates from the  $\text{SiO}_2$  matrix [34]. The presence of smaller crystals explains the increase in  $E_{QD}^{gap}$  for lower silicon content. This would also explain the larger values of standard deviation shown by samples 2 and 3. During crystallization, some QDs grow until they reach the maximum diameter allowed by the structure of the sample (4 nm), while some others might stop growing due to excess silicon unavailability, resulting in a wider size dispersion. Another hypothesis is that the growth stops when the diameter of the dots reaches the thickness of the silicon-rich layer. This is supported by the fact that the DOS standard deviation of our samples (confined in size by the superlattice structure) is less than half the value reported by van Seville et al. [1], where the samples used were monolayers.

The deposition recipe which corresponds to sample 1 shows to lead to a less defective material upon hydrogen effusion and to higher crystallinity upon high temperature annealing in forming gas. So, what was expected from theory and mentioned in the introduction is confirmed by our experiments which show a higher integrated QD DOS for increasing silicon content and therefore a higher QD density within the Si-rich layers. On the other hand, a higher silicon content does not lead to a higher, but to a lower defect density, both upon hydrogen effusion and crystallization.

## Discussion

In this section the effect of the silicon content in Si-rich layer is investigated for the same annealing procedure, upon hydrogen effusion and crystallization.

Three samples with different silicon content were annealed in FG at 500 °C for 3 and 6 min to investigate the hydrogen effusion process and the consequences it has on the defect formation in the material. Also in this case complete dehydrogenation was obtained only after an annealing duration of 6 min. According to the results, the relative hydrogen content  $R_H$  decreases for increasing Si content of the material. This is reflected by the absorption coefficient below 1.5 eV, which showed to slightly decrease for increasing silicon content.

In a second stage three as-deposited samples were annealed, always in FG, at 1000 °C for 3 min. This was done to investigate the evolution of QDs properties as a function of different composition of material. The results showed a clear increase of crystallinity and  $I_{QD}$  for increasing Si content. Slightly lower band gap and DOS standard deviation are associated to increasing crystallinity.

In conclusion a higher silicon content in the Si-rich layer seems to be beneficial in terms of annealing induced defects and reachable crystallinity.

### 4.2.3 Influence of annealing temperature

In this section the influence of annealing temperature on the evolution of QDs is investigated. The aim of this set of experiments is to find the threshold temperature at which crystallization starts for a-SiO<sub>x</sub>/SiO<sub>2</sub> superlattice samples annealed in a RTA furnace. Another aspect which is investigated is the effect of increasing temperature on the QDs formation and evolution. Samples obtained from the same batch are used for this annealing temperature series. The deposition consisted in a stack of 35 alternating a-SiO<sub>x</sub> (4 nm thick) and a-SiO<sub>2</sub> (1 nm thick) layers, on a quartz substrate. The deposition recipe used for the a-SiO<sub>x</sub> layer (see 4.2.2) corresponds to the highest silicon content (78,1%). From what was concluded from section 4.2.1, annealing in forming gas leads to a lower defect density in the dehydrogenated material and to a higher crystallinity. Therefore, this environment was chosen for these experiments.

Each sample was annealed once for a duration of 3 min. The annealing temperature was increased, from sample to sample, from 900 up to 1040 °C with intervals of 20 °C. As the crystallization was expected, from previous experiments, to start at around 950 °C, the step size around this temperature was decreased to 10 °C. Increasing the annealing temperature by intervals of 10 °C from sample to sample results in a determination error of approximately ± 5 °C for the occurrence of crystallization. One sample was kept as-deposited and one was annealed at 500 °C for 6 min, in order to obtain a dehydrogenated film and use it in the QDs characterization.

After annealing the crystallinity was obtained from Raman spectroscopy measurements, and the results are reported in figure 4.12 on the left *y*-axis.

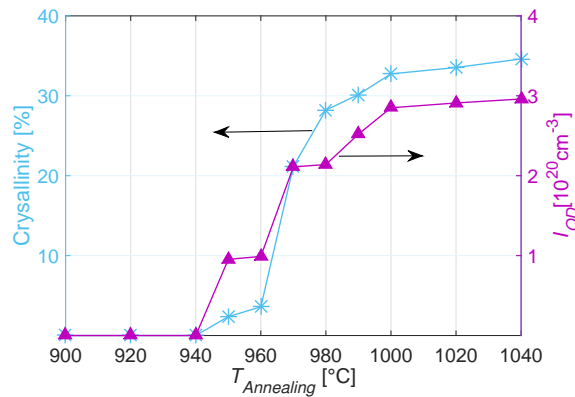


**Figure 4.12:** Crystallinity (left axis) and integrated QD DOS (right axis) of samples annealed from 900 to 1040 °C for 3 min in FG atmosphere.

Crystallization starts between 940 and 950 °C, but up to 960 °C it remains below 5%. A considerable increase occurs between 960 and 970 °C, after which the crystalline fraction as a function of temperature keeps increasing, but at a lower pace. The RTA furnace does not allow to anneal at temperatures above 1040 °C, so it was not possible to continue the series and verify whether a saturation point had already been reached. In figure 4.12, on the right *y*-axis, the integrated QD DOS as a function of annealing temperature is shown. The results obtained for  $I_{\text{QD}}$  are in good agreement with what was observed in crystallinity. Zero or extremely low values are obtained for samples annealed up to 960 °C. For the next annealing

step a step increase occurs, followed by a more stable increase which continues up to the highest temperature 1040 °C.

The next parameters to be analyzed are the QD energy band gap and their QD DOS standard deviation and they are reported in figure 4.13.

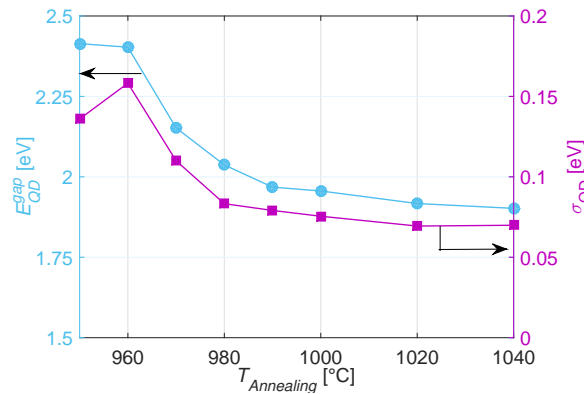


**Figure 4.13:** QDs energy band gap (left axis) and standard deviation of QDs DOS distribution (right axis) of samples annealed from 950 to 1040 °C for 3 min in FG atmosphere.

Apart from the sample annealed at 960 °C, for which  $E_{\text{QD}}^{\text{gap}}$  and  $\sigma_{\text{QD}}$  show discordant trends, the two parameters follow a similar behaviour for increasing annealing temperature. This is in accordance with what shown by crystallinity and integrated QD DOS and with theory. In fact, as the QD grow larger, their size uniformity increases and the energy band gap decreases.

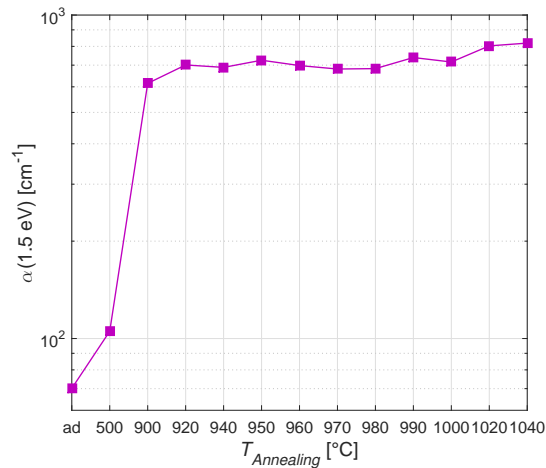


**Figure 4.14:** Absorption coefficient  $\alpha$  at 1.5 eV of samples annealed from 900 to 1040 °C for 3 min in FG atmosphere. Note that the  $x$ -axis step size is **not** constant.

The value of the absorption coefficient at 1.5 eV is taken as a reference to analyze the evolution of sub-gap, defect related absorption. Its trend is represented in figure 4.14. There is an increase in absorption between the as-deposited sample and the dehydrogenated one. After that, another considerable step is visible between hydrogen effusion and annealing at 900 °C.

$\alpha(1.5\text{ eV})$  stabilizes then without significant changes for increasing temperatures. This is shown by its average stabilized value, which is  $715\text{ cm}^{-1}$  with a standard deviation of  $57\text{ cm}^{-1}$ .

## Discussion

To summarize, a-SiO<sub>x</sub>/SiO<sub>2</sub> samples were annealed in FG atmosphere for 3 min for increasing temperature (from 900 up to 1040 °C) to observe the evolution of QDs as a function of annealing temperature.

What can be concluded from this set of experiments is that the crystallization of the films and the QDs properties strongly depend on the annealing temperature. The results were in full agreement with what is expected from theory and they can be summarized in a few points:

- Crystallization starts between 940 and 950 °C, crystallinity increases proportionally with increasing temperature throughout the whole range we considered. The increase in crystallinity is very steep between 960 and 970 °C where it passes from 4 to 21 %. Between 970 and 1040 °C it keeps increasing but with a lower slope.
- Fitting the absorption measurements allowed to extract the characteristics of embedded QDs. The results are in accordance with what was previously found with crystallinity measurements. The integrated QD DOS follows the same exact trend, constantly increasing from 950 to 1040 °C. A change in slope is found also here after 970 °C. The calculated energy band gap of the samples starts from high values (approximately 2.4 eV and it decreases for increasing crystallinity and  $I_{QD}$ , to a minimum of approximately 1.9 eV). As the crystals grow larger, from the first to the last sample of the series, the DOS standard deviation is almost halved, indicating a narrower size distribution.
- The absorption coefficient at 1.5 eV, which is in the sub-gap, defect related range of the spectrum, is taken as a measure of the evolution of defects in the material. A first increase is observed upon hydrogen effusion, and a second one occurs for annealing at 900 °C. Its value does not seem to be affected by increasing temperatures, nor by crystallization.

#### 4.2.4 Influence of annealing time

After the analysis of the influence of annealing temperature on the crystallization of the films and the evolution of QDs, it is interesting to assess the influence of annealing time on these parameters. With this aim a new set of experiments was carried out and is presented in this section.

For this purpose, samples obtained from the same deposition batch were used. The configuration of the samples is 4 nm-thick silicon-rich and 1 nm-thick silicon dioxide, repeated for 35 periods. Given the results of section 4.2.1 the annealing is carried out, in this experiment, in FG atmosphere. From what was found in section 4.2.2 the deposition recipe used for the a-SiO<sub>x</sub> layer is the one corresponding to sample 1 (78,1% of silicon content). The deposition was made on quartz substrates.

The procedure consisted, after cutting the as-deposited sample in pieces, in annealing them for different durations varying from 0.5 min to 5 min with an interval of 0.5 min. Increasing the annealing time by intervals of 0.5 min from sample to sample results in a determination error of approximately  $\pm 15$  s for the occurrence of crystallization. The procedure was repeated at three different temperatures (980, 1000 and 1020 °C), in order to be able to draw more consistent conclusions on the results. These specific temperatures were chosen after what was observed in section 4.2.3, at approximately 1000 °C the maximum crystallinity was obtained. A sample was kept as-deposited and one was annealed at 500 °C for 6 min, in order to obtain a dehydrogenated film and use it in the QDs optical analysis.

After annealing, the samples were measured with Raman spectroscopy and their crystalline fraction was calculated. What is observed is an unexpected behaviour and it is shown in figure 4.15a.

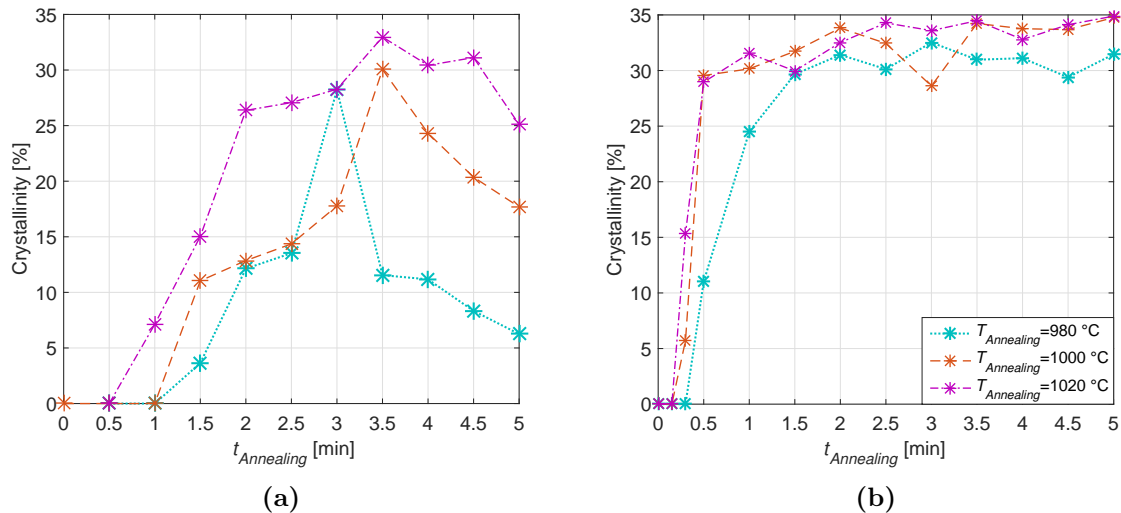


**Figure 4.15:** Crystallinity of samples annealed at 980, 1000 and 1020 °C for 0.5 min to 5 min (a) in FG atmosphere and in (b) N<sub>2</sub> atmosphere.

The usual crystallization behaviour of amorphous silicon was explained in section 2.2, where the process was divided into three phases [48]:

- Incubation time

- Nucleation and crystallization
- Saturation of crystallinity

For what concerns the first and the second phases, our samples seem to behave coherently with what is expected from theory. Crystallization starts after a certain incubation time (which decreases for increasing annealing temperature) and then increases until it reaches a maximum value. From this point on, instead of remaining stable at a saturation value, the crystalline fraction of the samples starts decreasing. The trend is clear and visible independently of the annealing temperature. It was not possible to further extend the annealing time as the RTA furnace can not be operated at such temperatures for longer than 5 min.

Annealing in forming gas initially seemed to be more beneficial in terms of defects evolution upon hydrogen effusion and slightly more effective in terms of crystallinity compared to nitrogen atmosphere annealing. By extending the annealing time up to 5 min, though, it turned out to be unstable with respect to all the variables which are taken into account in this work. To understand whether this phenomenon is correlated to the annealing atmosphere, the same exact annealing procedure section was repeated in nitrogen atmosphere. The results of crystallinity measurements for this experiments are shown in figure 4.15b.

It is noticeable how the incubation time decreases with respect to the forming gas atmosphere. In fact, when annealed in forming gas, the samples did not crystallize before 0.5 or 1 min at each tested temperature. In this case the crystallization starts between 10 and 20 s. It should be underlined, though, that the accuracy in the determination of incubation time through crystallinity measurements as a function of annealing time is less accurate for these short annealing times. In fact, even if the annealing time can be precisely controlled, the RTA furnace used for this procedure has a ramp-up time of approximately 0.5 min, part of which is above crystallization temperature.

For all three annealing temperatures the crystallinity profiles reported in figure 4.15b are in accordance with what is described in literature [7], showing an incubation time, crystallization and saturation. The samples annealed at 1000 and 1020 °C show comparable behaviours, both in terms of trend and crystallinity values. They both show a beginning of crystallization between 0 and 0.15 min. The crystalline fraction steeply increases up to 1 min, from where it keeps increasing at a slower pace. From  $t_{Annealing} \geq 2$  min the crystallinity saturates at an average value of  $33 \pm 2.1\%$  and  $33.8 \pm 0.8\%$  for annealing temperatures of 1000 °C and 1020 °C, respectively. At  $T_{Annealing} = 980$  °C the crystallization starts later (between 0.15 and 0.3 min) and the crystalline fraction remains lower, also for long annealing times. The average value around which crystallinity stabilizes after saturation is  $31.1 \pm 1\%$ . The fluctuation of the crystallinity value can be considered within measurement error margin.

Proceeding in the optical analysis the characterization of the QDs is carried out. An analogous trend as observed for crystallinity is found in the values of the integrated QD DOS  $I_{QD}$ . The results are reported in figure 4.16a. A first steep increase is visible and then, at each temperature,  $I_{QD}$  decreases after a certain threshold annealing time. This result was expected, since the crystallinity is directly related to the density of QD states.

When looking at the samples annealed in N<sub>2</sub> (see figure 4.16b), the same trend as shown by crystallinity is found.  $I_{QD}$  starts increasing after 0.15 min for the samples annealed at 1000 and 1020 °C. After the start of crystallization a steep increase in  $I_{QD}$  occurs, followed by a slower one. The integrated QD DOS stabilizes around a saturation value. The average saturation values for these samples are  $2.79 \times 10^{20} \pm 0.22 \times 10^{20} \text{ cm}^{-3}$ ,  $3.05 \times 10^{20} \pm 0.21 \times 10^{20}$

$\text{cm}^{-3}$ , respectively. The samples annealed at  $980^\circ\text{C}$  show an increasing  $I_{\text{QD}}$  after 0.3 min. In this case the average saturation value is  $2.67 \times 10^{20} \text{cm}^{-3}$  and its standard deviation is  $0.12 \times 10^{20} \text{cm}^{-3}$ .

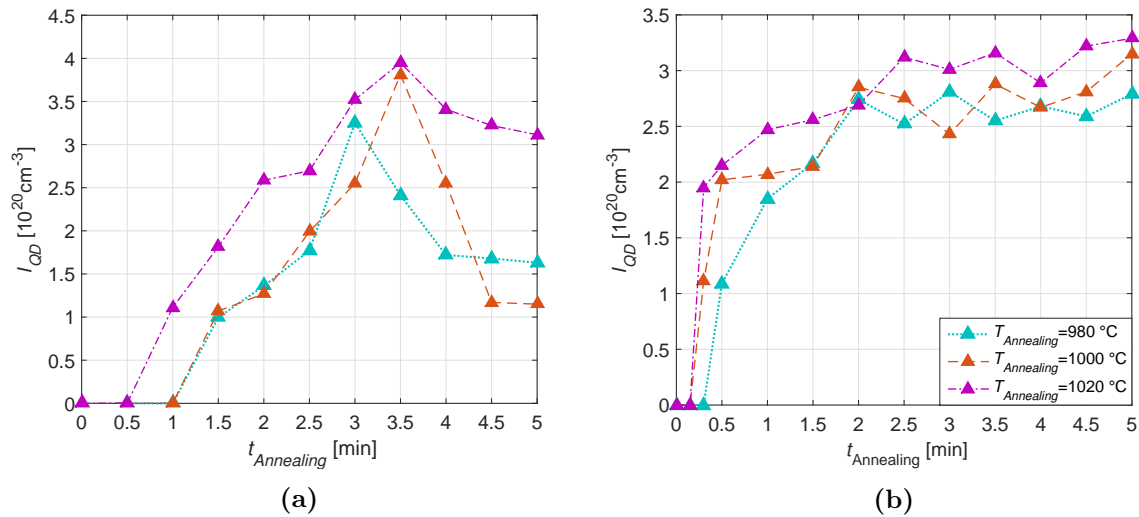


**Figure 4.16:** Integrated QD DOS of samples annealed at  $980$ ,  $1000$  and  $1020^\circ\text{C}$  for  $0.5$  min to  $5$  min (a) in FG atmosphere and in (b)  $\text{N}_2$  atmosphere.

What is analyzed next is the evolution of QDs energy band gap as a function of annealing time, for both the annealing environments.

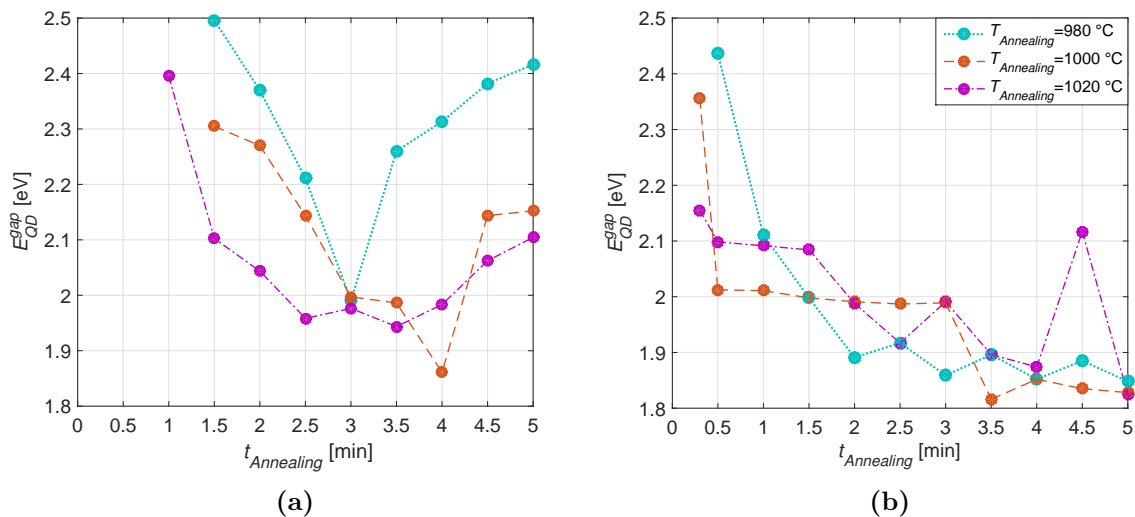


**Figure 4.17:** QDs energy band gap of samples annealed at  $980$ ,  $1000$  and  $1020^\circ\text{C}$  for  $0.3$  min to  $5$  min (a) in FG atmosphere and in (b)  $\text{N}_2$  atmosphere.

Also when considering the QDs energy band gap, the results are consistent with what was found so far, as shown in figure 4.17a. For short annealing time, as the nucleation starts, the QDs are very small and their energy band gap is consequently very wide. As the crystallinity reaches its maximum the QDs have grown to their largest size and their band gap decreases

accordingly. Coherently, when the crystalline fraction decreases, their band gap becomes wider again, indicating the QDs are shrinking.

For the samples annealed in  $N_2$  (see 4.17b), as expected, the energy band gap of the dots decreases for increasing crystallinity and  $I_{QD}$ . After a considerable decrease, which corresponds to the crystallization phase, the band gap reaches saturation.

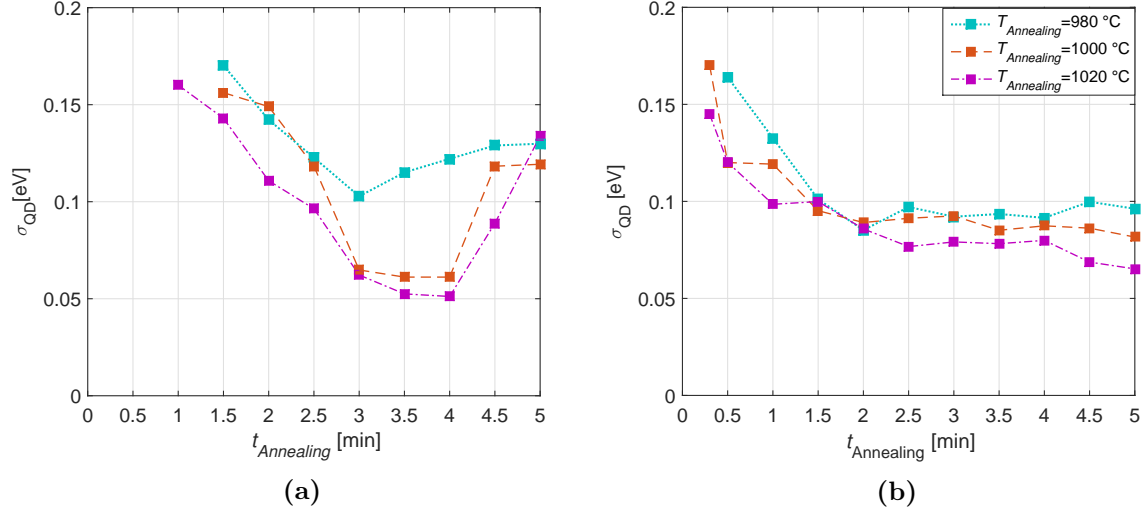


**Figure 4.18:** QD DOS standard deviation of samples annealed at 980, 1000 and 1020 °C for 0.3 min to 5 min (a) in FG atmosphere and in (b)  $N_2$  atmosphere.

A trend as that noticed in QDs energy band gap is noticeable for the standard deviation of QDs DOS distribution for the samples annealed in FG (see 4.18a).  $\sigma_{QD}$  becomes narrower for increasing values of crystallinity, showing that as the QDs grow larger they find themselves confined by the structure of the stack and their size becomes more uniform. For decreasing values of crystallinity  $\sigma_{QD}$  increases again, indicating a wider size distribution. Combining these results, we can conclude that the QD growth follows the typical nucleation theory, up to 2 to 2.5 min. For longer annealing, the QDs state density and crystallinity decrease, indicating smaller and/or fewer QDs. From the increase in energy band gap, we can conclude that the mean QD size decreases. However, the QD DOS distribution width increases simultaneously, indicating that not all QDs shrink at the same rate.

For samples annealed in  $N_2$  (see figure 4.18b) the DOS standard deviation  $\sigma_{QD}$  also follows a trend which is inversely proportional to the crystalline fraction. The size distribution becomes noticeably narrower during crystallization since, for all three temperatures, after a steep decrease,  $\sigma_{QD}$  stabilizes between 0.1 and 0.07 eV.

The evolution of sub-gap absorption upon hydrogen effusion and crystallization is reported in figure 4.19. For what concerns the samples annealed in FG, a strong increase is visible upon hydrogen effusion with respect to the as-deposited condition. Another step increase in absorption is noticeable upon crystallization (from 0.5 min to 1.5 min), after which the absorption becomes almost independent of annealing time. The average value of absorption coefficient after crystallization starts, is of  $736 \text{ cm}^{-1}$  with a standard deviation of  $14 \text{ cm}^{-1}$ .

For the samples annealed in  $N_2$  the behaviour is analogous. At each annealing temperature a first strong increase in absorption is visible when passing from the as-deposited samples

to the dehydrogenated ones. Another considerable step occurs upon crystallization. After nucleation all the three curves saturate around a common value. For increasing annealing temperature, the values of  $\alpha$  at 1.5 eV) are stabilized at approximately  $1026 \pm 9 \text{ cm}^{-1}$ .

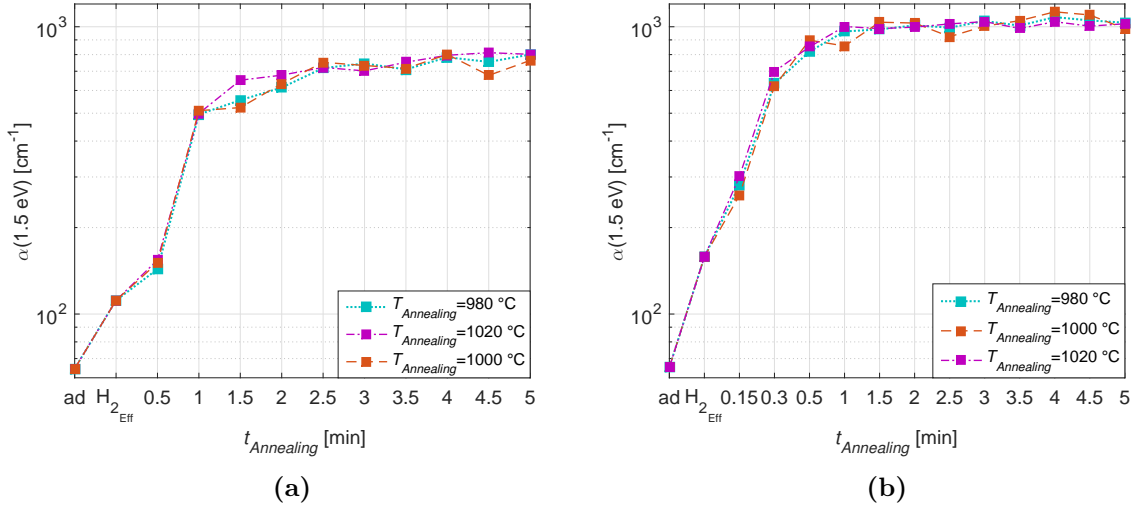


**Figure 4.19:** Sub-band gap absorption at 1.5 eV of samples as-deposited, upon hydrogen effusion and annealed at 980, 1000 and 1020 °C for 0.5 min to 5 min. (a) in FG atmosphere and in (b) N<sub>2</sub> atmosphere. Note that the  $x$ -axis step size is **not** constant in this figure.

To be noticed is the difference with the samples annealed in forming gas whose average value of  $\alpha$  at 1.5 eV) were found to be of approximately  $736 \text{ cm}^{-1}$ .

As all these parameters show a trend as a function of annealing time, it is also interesting to investigate correlations among them.

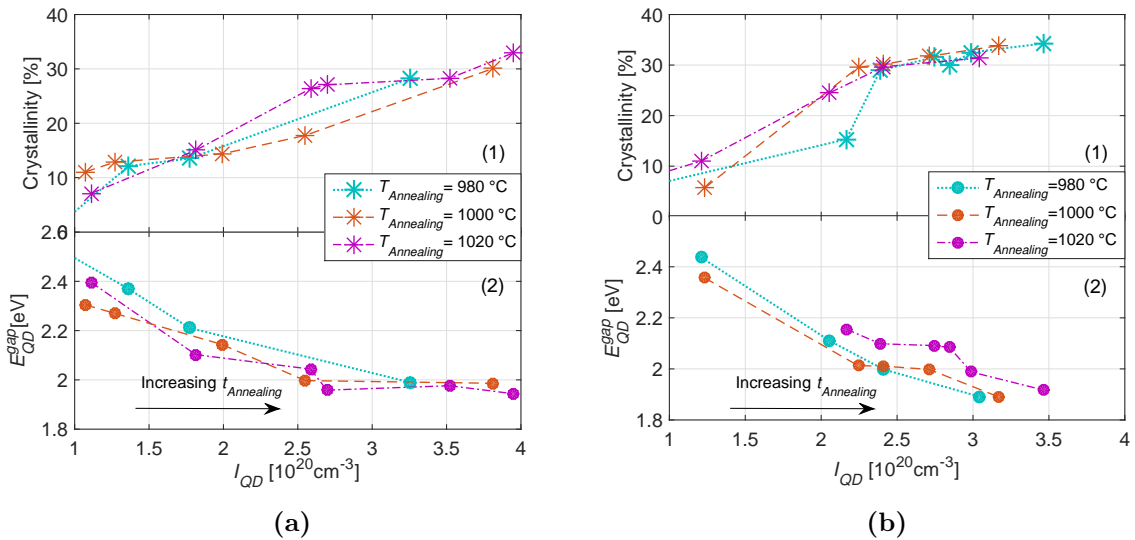


**Figure 4.20:** (a-1) Crystallinity and (a-2)  $E_{\text{QD}}^{\text{gap}}$  as a function of  $I_{\text{QD}}$  for increasing annealing time in FG atmosphere. (b-1) Crystallinity and (b-2)  $E_{\text{QD}}^{\text{gap}}$  as a function of  $I_{\text{QD}}$  for increasing annealing time in N<sub>2</sub> atmosphere.

In figure 4.20a the crystallinity and the QDs band gap are plotted as a function of the inte-

grated QDs DOS. The annealing time considered ranges between 1 and 3.5 min, the interval in which the parameters under analysis are monotonous in trend. As  $I_{QD}$  increases with annealing time, the crystallinity varies accordingly, in an approximately linear trend. Instead, the QDs band gap decreases for increasing  $I_{QD}$ . The increase in QD state density can therefore be associated to an increasing mean QD size, in accordance with theory (see section 2.1.4). In figure 4.20b the crystallinity and the  $E_{QD}^{gap}$  are shown as a function of the integrated QD DOS for samples annealed in  $N_2$ . In order to have monotonous values for both the band gap and the crystallinity, only annealing times between 0.15 and 2 min are considered. This interval corresponds to the nucleation phase, after which these variables stabilize.

As  $I_{QD}$  increases the crystalline fraction behaves accordingly, while the QDs energy band gap decreases. This happens at each annealing temperature and the variables show approximately the same rate. The energy band gap decreases leads to the conclusion that the increase in  $I_{QD}$  is due to an increase in mean QD size and not to an increase in QD density.

Another correlation which is interesting to investigate is the one between the QDs' DOS standard deviation, their band gap and the integrated unoccupied QDs DOS.

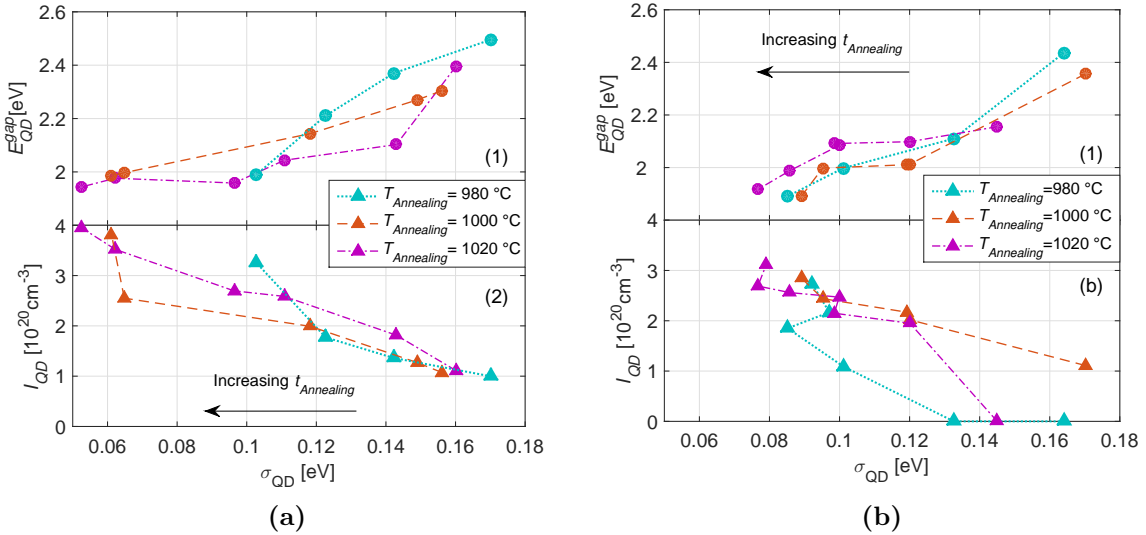


**Figure 4.21:** (a-1) QDs energy band gap and (a-2) Integrated QD DOS as a function of the QDs' DOS standard deviation for increasing annealing time in FG atmosphere. (b-1) QDs energy band gap and (b-2) Integrated QD DOS as a function of the QDs' DOS standard deviation for increasing annealing time in  $N_2$  atmosphere.

In figure 4.21a, for increasing annealing time, as the crystallinity and  $I_{QD}$  increase,  $\sigma_{QD}$  drops. While the nucleation proceeds and the QDs reach the maximum size allowed by the structure of the sample, their size distribution becomes more uniform until  $\sigma_{QD}$  reaches its minimum. The maximum value of  $\sigma_{QD}$  corresponds to the widest band gap, so to the minimum size of the QDs. During the phase of increasing crystallinity and  $I_{QD}$ , the QDs' DOS standard deviation decreases differently for different annealing temperatures. The sample annealed at 980 °C shows a minimum  $\sigma_{QD}$  almost twice as large as the samples annealed at higher temperatures. It might indicate that, after nucleation starts, the QDs growth rate increases with increasing temperature.

In figure 4.21b, as expected from previous experiments,  $\sigma_{QD}$  and  $I_{QD}$  are inversely proportional and as the former decreases, the latter increases.

On the other hand the QDs band gap and  $\sigma_{QD}$  both decrease, approximately linearly, throughout the nucleation phase.

In general, what is observed during the annealing in FG for increasing duration seems to be anomalous. For this reason further investigation is needed to study this unexpected phenomenon.

## Discussion

To summarize, a-SiO<sub>x</sub>/SiO<sub>2</sub> multilayer samples were annealed in forming gas atmosphere at three different temperatures (980, 1000 and 1020 °C) for increasing annealing time (from 0.5 to 5 min) to observe the evolution of QDs as a function of annealing time.

What is observed to happen to our samples is something unexpected and in disagreement with crystallization theories for a-Si alloys. The same phenomenon occurred at the three different temperatures that were tested during these experiments. The crystallinity, after a certain threshold annealing time at which a maximum value is reached, starts decreasing. A similar trend is reflected by all the parameters which are used, during this work, for the characterization of the QDs: the integrated QDs states, their energy band gap and the standard deviation of their DOS distributions. The only parameter that, as was expected, increases until its maximum and then saturates is the absorption coefficient at 1.5 eV.

XPS measurements showed that the oxygen content of the film does not increase, after annealing, with respect to the as-deposited sample. This indicates that no oxidation occurs upon annealing. The decrease in crystallinity can not be attributed, therefore, to a conversion of Si-Si bonds into Si-O bonds. A different behaviour is shown by the samples annealed in pure nitrogen atmosphere. In fact, even if the exact same procedure was followed in terms of annealing time and temperatures, the characterization parameters followed the trends suggested by theory. In N<sub>2</sub> annealed samples, the crystallinity increased proportionally with time until saturation, and the other QD characterization parameters varied coherently.

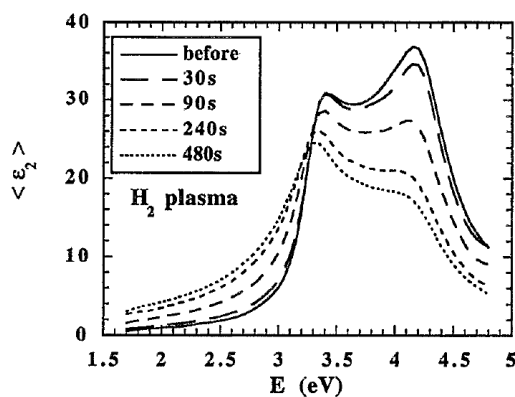


**Figure 4.22:** Imaginary part  $\varepsilon_2(\lambda)$  of the dielectric function of boron-doped crystalline silicon wafers as a function of plasma annealing time [9].

hand, a side effect is the introduction of electronic defects on the surface that undergoes the

As this phenomenon happened repeatedly and with a consistent trend it is very unlikely to be an artifact and it deserves further investigation. As already mentioned, the only difference between the two procedures was the annealing atmosphere and, therefore, a relevant role is thought to be played by the presence of hydrogen in the chamber.

Hydrogen treatments on semiconductor surfaces are used for a variety of purposes, for example defect passivation or surface cleaning [9]. The treatments are mostly carried out in plasma environment, which turns out, in case of silicon wafers, to be an excellent tool for dangling bonds passivation. On the other

treatment [9, 75, 76]. As this can be detrimental in the fabrication of silicon based optoelectronic devices, a technique for monitoring the evolution of electronic defects on the material during hydrogen treatment was studied by Neitzert et al. [9]. An amorphization process was observed as a function of duration of plasma exposure. The trend of the imaginary part of the dielectric function  $\varepsilon_2(\lambda)$  was studied (see figure 4.22). A considerable decrease and red-shift in the peaks at 3.4 and 4.2 eV were noticed and considered as the signature of a porosification and roughening of the film. An increase of  $\varepsilon_2(\lambda)$  for photon energies lower than 4.2 eV suggests an increased absorption in low energy range, meaning an amorphization of the crystalline surface occurred. An amorphous fraction of approximately 20% is found to appear in the top layer of the crystalline silicon wafer, which also becomes more porous. The thickness of the layer varies with the square root of the hydrogen plasma exposure duration. A drastic decrease in optically generated excess carriers lifetime is observed after plasma treatments, meaning that the number of surface states which act as recombination centers has increased. It was concluded, from this experiment, that hydrogen plasma has a chemical effect on the exposed material and, by diffusing through the crystalline wafer, it etches the weak Si-Si bonds and it passivates the Si dangling bonds. This creates a defective and partly amorphous over-layer, whose thickness increases with the exposure time

What reported here is specifically referred to as plasma treatments on crystalline silicon, which does not really coincide with what is used in this work. Still, we are looking for some possible influence the hydrogen presence can have on the stability of crystalline silicon.

Some considerations can be done and some analogies between our case and what reported in literature emerge.

Our samples consist of a-SiO<sub>x</sub> layers with embedded c-Si QDs. Keeping in mind that:

- Spontaneous dissociation of molecular into atomic hydrogen, which occurs at temperatures much larger than those used in this work (about 5000 °C [77]), is not necessary for hydrogen diffusion. Studies on H<sub>2</sub> solubility and diffusivity in silicon [78] show that measurable permeation rates are observed for annealing in H<sub>2</sub> gas atmosphere for temperatures around 1000 °C and that the diffusion coefficient is governed by an Arrhenius law. What is interesting is that, defined  $p_0$  as the partial pressure of H<sub>2</sub> in the annealing environment, the diffusion coefficient varies proportionally to  $p^{0.56}$ . This means that the dissolved hydrogen is almost totally in its mono-atomic configuration. Further studies [79] shown that the dissociation of molecular into atomic hydrogen and its diffusion in the material are, for crystalline silicon wafers, enhanced by surface damage. The silicon vacancies  $V$  at the surface can cause the spontaneous dissociation of H<sub>2</sub> molecules. In this process a H-H bond is broken and a Si-H bond is formed according to [79]:  $\text{H}_2 + V \Rightarrow (\text{H} + V) + \text{H}$ . The complexes H and (H + V) can then independently diffuse through the material with a diffusion coefficient which is proportional to the concentration of vacancy-related defects [79]. The kinetics of this phenomenon was studied and reported by Estreicher et al. [80]. They show that as the distance between a hydrogen molecule and a vacancy  $V$  decreases, the energy barrier which separates the molecular form from the atomic form disappears, and H<sub>2</sub> dissociates. This is accompanied by a large release of thermal energy (1.7 to 4 eV). Li et al. showed that this hydrogen dissociation process due to surface damage mechanism can also apply to PECVD passivation processes [81].
- The substrate temperature during RTA annealing in forming gas is much higher than

during plasma treatment, 425 °C and  $1000 \pm 20$  °C, respectively, and the diffusion of H atoms is, as its will be thoroughly explained in the next paragraphs, temperature dependent.

- From previous experiments carried out on PECVD-deposited, laser annealed a-Si<sub>0.66</sub>O<sub>0.33</sub> samples a measurable passivation effect occurred when they were exposed to a hydrogen treatment. Interesting finding was the little difference noticed when the annealing was carried out with or without plasma <sup>2</sup> (see Appendix A). From the same experiments no significant difference was found when varying the RF power from 5 to 40 W, when varying the time from 1 to 2 h, nor when varying the chamber temperature from 425 to 525 °C.
- The residence time of a gas in a chamber is expressed by [82]:  $\tau = \frac{p_0}{p_{ref}} \frac{V}{\phi}$ , where  $p_0$  is the partial pressure of the gas,  $p_{ref}$  is the reference atmospheric pressure,  $V$  is the volume of the chamber and  $\phi$  is the gas flow rate. The value of  $\tau$  during RTA annealing we carried out in forming gas is much higher than that during the plasma treatment, 18.75 s and 0.55 s, respectively.

The diffusion coefficient of hydrogen in a-Si is temperature dependent and it generally follows the relation [83]:

$$D_H = D_0 \exp\left(-\frac{E_a}{kT}\right) \quad (4.1)$$

Where  $k$  is the Boltzmann's constant,  $T$  is the temperature,  $E_a$  is the activation energy and  $D_0$  is a prefactor. The specific values of  $E_a$  and  $D_0$ , which in the study by Neizert et al. were calculated for a-Si, are probably different for a-SiO<sub>x</sub> but the exponential law is expected to remain applicable. Street et al. propose three different models according to which hydrogen can diffuse through an a-Si matrix [83] and they are described below.

- *Hydrogen diffusion via dangling bonds*  
According to this model atomic hydrogen atoms can diffuse by hopping to the nearest-neighbour dangling bond. This implies that the atoms can not move unless a new Si-H bond can be formed at an adjacent site. The diffusion of a hydrogen atom corresponds to the diffusion of dangling bonds. In this model the diffusion coefficient is calculated as  $D_H = a^2 \frac{p_H}{6}$ . Where  $a$  is the distance the H atoms need to cover and  $p_H$  is the hopping rate. This latter parameter is defined as the probability  $p_{HD}$  that a dangling bond and a H atom switch place multiplied by the ratio in dangling bond density  $N_D$  and H atoms density  $N_H$ . The process is assumed to be activated by an empirical prefactor  $\nu_0$  and by an activation energy  $E_a$ . This results in the following expression for the diffusion coefficient:

---

<sup>2</sup>Samples of a-Si<sub>0.66</sub>O<sub>0.33</sub> were fabricated in the same batch. They were deposited in a monolayer configuration and their thickness was approximately 100 nm, in a second step they were laser annealed with a sufficient power fluence to obtain phase separation and silicon crystallization. The absorption coefficient was then measured and, at 1.5 eV, it was  $\alpha=2050$  cm<sup>-1</sup>. Hydrogen plasma treatment was carried out on one of the samples at the conditions of 525°, 200 sccm of hydrogen gas flow, an RF power of 5 W for one hour.  $\alpha$  was measured again and at 1.5 eV it decreased to 900 cm<sup>-1</sup>. Hydrogen gas treatment was carried out on another sample at the same conditions, but without RF power. Again  $\alpha$  at 1.5 eV dropped, this time to 1140 cm<sup>-1</sup>. The experiments were carried out by Martijn van Sebille at TU Delft.

$$D_H = a^2 \left( \frac{N_D}{6N_H} \right) p_{HD} = a^2 \left( \frac{N_D}{6N_H} \right) \nu_0 \exp \left( -\frac{E_a}{kT} \right) \quad (4.2)$$

The validity of this model, though, holds only if the distance between dangling bond and H atom is roughly corresponding to a Si-H bond length. Since this is not always the case, the diffusion mechanism should be able to happen, with the same probability, from all Si-H sites.

- *Hydrogen diffusion via interstitials*

The assumption made for this model is that an interstitial H atom can diffuse until it can recombine with a dangling bond. By defining the energy of the reaction as  $E_I$ , the density of interstitials  $N_I$  is related to the density of empty interstitial sites density  $N_0$  through:

$$N_I N_D = N_0 N_H \exp \left( -\frac{E_I}{kT} \right) \quad (4.3)$$

Being the hopping rate of the interstitial hydrogen as  $p_{HI}$ , it is possible to define the diffusion coefficient of this process:

$$D_H = a^2 \left( \frac{N_0}{6N_D} \right) p_{HI} \exp \left( -\frac{E_I}{kT} \right) \quad (4.4)$$

- *Hydrogen diffusion via silicon bonds*

This model assumes that a H atom can diffuse by breaking a Si-Si bond and forming a Si-H. The diffusion energy corresponds to the energy necessary to break a Si-H bond. Given  $f$  the mean free path for the interstitial, the diffusion coefficient is given by:

$$D_H = f^2 \left( \frac{\nu_0}{6} \right) \exp \left( -\frac{E_I}{kT} \right) \quad (4.5)$$

The three mechanisms described above are not mutually exclusive, the phenomenon of H atoms diffusion can probably be expressed as a contribution from all of them [83].

As already mentioned and also proven by our experiments, at approximately 400 °C the hydrogen in the film starts effusing from the a-SiO<sub>x</sub>:H. After some time an equilibrium between the atomic H flux provided by the surrounding annealing environment and the hydrogen flux leaving the matrix establishes. This diffusion process can occur, not only at the surface of the film, but also in the bulk as it is confirmed by secondary ions mass spectrometry carried out for hydrogen profiles, on a-Si samples [83]. As the temperature of the film increases (at approximately 750 °C [45]), according to nucleation theories, the excess silicon in the silicon-rich layers starts precipitating into a-Si QDs (figure 4.23 -a), and after reaching crystallization temperature, the amorphous Si-Si bonds in the newly formed amorphous clusters rearrange and become crystalline (figure 4.23-b). As a result, an a-SiO<sub>x</sub>/c-Si interface is formed and the QDs are surrounded by silicon oxide, as shown in figure 4.25. The hydrogen gas dissociates and in its atomic form flows, via diffusion, in and out the amorphous matrix and reaches the QDs interface, where, according to what reported in the paragraphs above, it amorphizes the crystalline phase by creating an over-layer of porous and partly amorphous material (figure

4.23-c). In this way the two phases, silicon and silicon oxide, remain separated, but the crystalline part of the QDs shrinks as an amorphous shell forms around it (see figure 4.23-c).

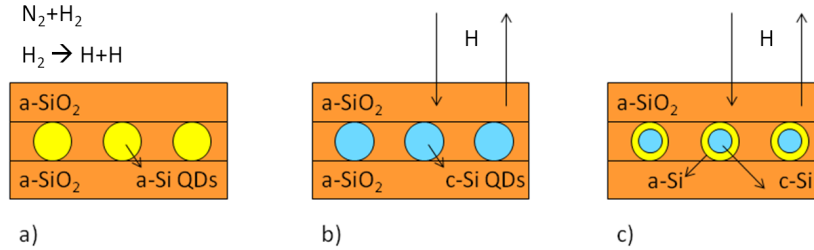


**Figure 4.23:** Schematic representation of (a) nucleation a-Si dots and H<sub>2</sub> splitting in atomic hydrogen H (b) crystallization of a-Si into c-Si dots and H diffusion through the film, (c) H diffusion to the QDs interface, formation of an a-Si shell and consequent shrinkage of c-Si QDs

Another possible explanation involves the participation of oxygen atoms in the diffusion process. This is called a hydrogen enhanced oxygen diffusion phenomenon. As Murray showed [84] the diffusion of interstitially bonded oxygen through silicon crystals is a thermally activated process and, among other factors, it is enhanced by high temperature annealing in the presence of a fast diffusing species. Especially he examined the case of samples annealed at 900 °C in a hydrogen containing atmosphere. The normal interstitial oxygen diffusion process (with no hydrogen involved), which leads to the formation of silica precipitates in c-Si, is described by a relation exponentially dependent on the temperature as:

$$D(O_i) = 0.11 \exp\left(-\frac{E_a}{kT}\right) \quad (4.6)$$

Where  $D(O_i)$  is the interstitial oxygen diffusion rate. The calculated activation energy is  $E_a = 2.5$  eV for normal diffusion.

In this study the diffusion of oxygen in crystalline silicon was observed in different annealing conditions. Among them, samples annealed at 900 °C in an inert gas with a partial pressure of hydrogen showed a diffusion coefficient which is almost one order of magnitude larger than the value calculated for normal diffusion. In this case the diffusion activation energy drops to 1.6 to 2 eV.

A further analysis of this phenomenon was carried out in the study by Capaz et al. [10], where the interaction of diffusing O+H complex with silicon was simulated. The steps of the process are represented in figure 4.24. The ground-state configuration of an oxygen atom in a silicon structure is a bond-center (BC) or an interstitial configuration ( $O_i$ ). During its migration through the lattice an O atom moves from a BC to an adjacent one and it has to jump a potential barrier of 1.46 eV. The migration of O atoms was modeled as follows.

Firstly the ground state of the (O+H) system is found (figure 4.24 (a)), then a migration pathway which leads to a final configuration electronically equivalent to the starting point is searched. The only difference between the initial and the final states is the translation of both atoms in the migration direction (figure 4.24 (d)).

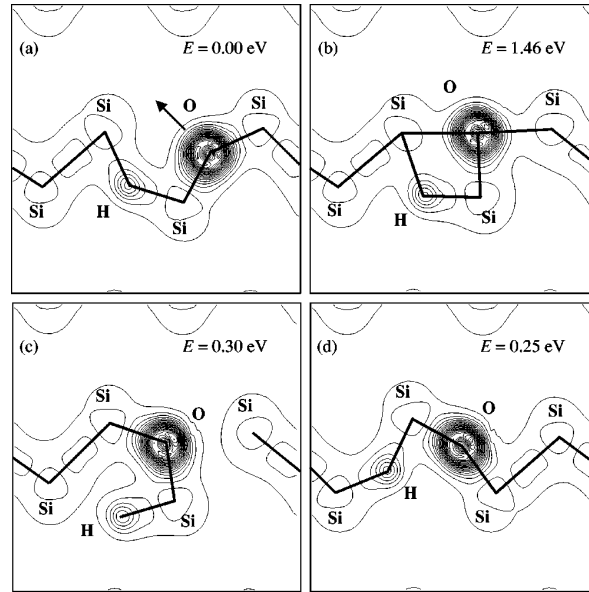


**Figure 4.24:** Steps of hydrogen enhanced oxygen diffusion through silicon crystals [10].

What was found is that this process occurs in two different steps. First, the O atom moves from one BC configuration to the adjacent one, reaching a maximum potential energy of 1.46 eV above its ground state (figure 4.24 (b)). Simultaneously, the system relaxes finding a new, metastable, minimum energy configuration. The H atom, instead of following the O atom and jumping to the next BC position, remains bonded to the central Si atom (figure 4.24 (c)). This configuration has a potential energy slightly higher than the initial ground state (0.3 eV). The Si-Si bond where the O atom was centered in the initial configuration remains broken, meaning that this migration process creates a dangling bond defect in the material. At this point the H atom plays a crucial role, by saturating one of the two Si dangling bonds it reduces the total potential energy of the system. In the second step (figure 4.24 (d)), the Si-H bond is broken, the H atom moves to the next BC position and the Si-Si bond is reformed, completing the circle. The role of H atoms in oxygen diffusion through silicon crystals is therefore to first, open up a Si-Si bond where the O atom will jump and second, to lower the energy of the system by passivating one of the two dangling bonds and bring it back to its ground state.

The process modeled by Capaz et al. describe the behaviour of oxygen impurities contained in Czochralsky-grown crystalline silicon wafers when exposed to a hydrogen containing annealing environment. The concentration of oxygen atoms is extremely low, more precisely of approximately  $3.14 \times 10^{17} \text{ cm}^{-3}$  [84]. The situation is different for our case, where the samples consist of c-Si QDs with a diameter of approximately 4 nm surrounded by a silica matrix.

An ideal  $\text{SiO}_2/\text{c-Si}$  interface presents a single Si dangling bond termination, each oxygen atom at the boundary is bonded to three silicon atoms and in the bulk silicon each Si atom is backbonded by four other Si atoms. On the other side of the interface, only  $\text{Si-O}_4$  groups are present as can be seen in figure 4.25.

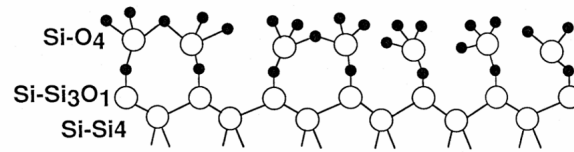


**Figure 4.25:** Ideal Si(111)/SiO<sub>2</sub> interface [11]. Silicon and oxygen atoms are represented by open and closed circles, respectively.

What is found to happen in reality is different from the metallurgical interface depicted above. More realistic is the formation of a not perfectly flat and ordered surface, where suboxide bondings are present (see figure 4.26). This layer, which for the interface between c-Si wafers and native SiO<sub>2</sub> is calculated to be a few Å thick [85], is called transition layer (Si-Si<sub>x</sub>O<sub>y</sub> in figure 4.26) and it introduces a certain degree of roughness and defects, namely dangling bonds and interstitial oxygen atoms [85].

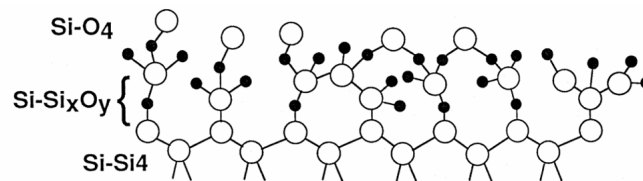


**Figure 4.26:** Si(111)/SiO<sub>2</sub> interface with sub-oxide bonding in a transition region [11]

If it is assumed that the hydrogen enhanced oxygen diffusion theory can be applied to any interstitial or BC oxygen atom in Si-Si bonds, an explanation to the phenomenon which occurs to our samples might be given.

A possibility is that, during annealing, two competing processes occur:

- The excess silicon precipitates into amorphous dots (figure 4.23 - a) and, after reaching an adequate temperature, they crystallize (figure 4.23 - b). This happens in accordance with phase separation and nucleation theories (see chapter 2.1.4).
- The hydrogen present in the forming gas dissociates and diffuses through the film and assists oxygen atoms in diffusing into the crystal, the transition layer broadens and the QDs shrink (figure 4.23 - c).

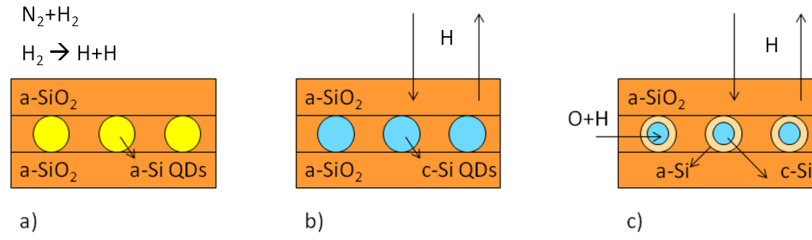


**Figure 4.27:** Schematic representation of (a) nucleation a-Si dots and  $H_2$  splitting in atomic hydrogen H (b) crystallization of a-Si into c-Si dots and diffusion of H through the film, (c) H enhanced migration of O atoms into the c-Si dots, formation of an  $a-SiO_x$  shell and consequent shrinkage of c-Si QDs.

In the first phase of crystallization, the first process prevails leading to QDs formation and growth. In the second phase, the growth of the crystals stops, due to lack of excess silicon in the Si-rich layers, or because they reached the maximum available space. From here on second process becomes the predominant one.

During its diffusion oxygen breaks crystalline Si-Si bonds leading to an amorphization of the QDs and to their apparent shrinking. This theory could also offer an explanation to the fact that, compared to the samples annealed in nitrogen, the films annealed in forming gas crystallize later for the same temperature.

The two mechanisms proposed above are not necessarily mutually exclusive. A possibility is also that they coexist and take part in the amorphization phenomenon of c-Si QDs. In fact, the  $Si-Si_xO_y$  transition layer might be too thin (few Å [85]) to be responsible, alone, for the decrease in crystallinity.

For what concerns annealing in  $N_2$  atmosphere,  $a-SiO_x/SiO_2$  superlattices were annealed, in this set of experiments, in nitrogen gas atmosphere at three different temperatures (980, 1000 and 1020 °C. The annealing time was varied from 0.5 to 5 min) to observe the development of QDs properties as a function of annealing time.

It was observed, in each measurement, a great dependence of the analyzed parameters on the annealing time. The trends were found to be consistent at each observed temperature. The outcome of these experiments is in line with what was expected from theory. A brief summary of the results is listed below:

- Nucleation starts between 0.15 and 0.3 min, crystallinity rapidly increases up to 2 min. The higher the temperature, the shorter the incubation time, the higher the crystallinity reached and the steeper the increase. After 2 min crystallinity stabilizes around a saturation value.
- From absorption measurements the properties of QDs were obtained. What is found is in full agreement with what was found in crystallinity measurements in the previous section. The integrated QD DOS follows the same trend as the crystalline fraction, it starts increasing after a certain incubation time and the maximum reached value is proportional with the annealing temperature. The calculated QDs energy band gap shows high values (about 2.4 eV for low crystallinity degrees and then it gradually decreases for increasing crystallinity and  $I_{QD}$ ). The minimum band gap reached is of approximately 1.85 eV. The size distribution becomes narrower as the crystals grow larger.

- The absorption coefficient at 1.5 eV shows two increasing steps, one correspondent to hydrogen effusion and the other one to the beginning of crystallization. For the following annealing steps, there is no evidence of correlations between defect related absorption and annealing time. To be noticed is that, compared to samples annealed in forming gas, those annealed in nitrogen show a considerably higher  $\alpha$ . This indicates that, upon nitrogen atmosphere annealing a much more defective material is generated.

#### 4.2.5 Influence of Si-rich layer thickness

For photovoltaic applications the most interesting aspect of QDs is the tunability of their optical properties with their size (see section 2.1.4). This is the reason why, after having analyzed the dependence of QDs characteristics as a function of silicon content, annealing atmosphere, temperature and time, it is interesting to observe their properties as a function of silicon-rich layer thickness. In fact, as earlier explained (see section 2.1.4), when QDs form upon crystallization, they are mostly spherical in shape and they are limited in diameter by the thickness in which they are confined by the SiO<sub>2</sub> buffer layers. In this section different types of samples are fabricated. The deposition recipes of the layers are kept constant to:

**Table 4.9:** Gas flow rates for the deposition of Si-rich and near stoichiometric silicon oxide layers.

| Layer            | SiH <sub>4</sub> [sccm] | CO <sub>2</sub> [sccm] | H <sub>2</sub> [sccm] |
|------------------|-------------------------|------------------------|-----------------------|
| Si-rich          | 10                      | 27                     | 200                   |
| SiO <sub>2</sub> | 2                       | 72                     | 200                   |

The silicon content of the former is 78.1% and the oxygen content of the latter is 56.6%. The depositions were made on quartz substrates. The structure was, for the samples used in this section, a Si-rich a-SiO<sub>x</sub>/SiO<sub>2</sub> superlattice of 35 periods. By varying the deposition time of the Si-rich layer its thickness was 2, 3, 4 or 5 nm. The thickness of the SiO<sub>2</sub> layer was kept at 1 nm. For a given Si-rich layer thickness, the samples used in this series of experiments were always obtained from the same batch. The as-deposited samples were cut in pieces and each of them was annealed for different durations and different temperatures. The annealing time was 3, 3.5 and 4 min while the annealing temperature was 980, 1000 and 1020 °C. The annealing atmosphere was nitrogen gas. The aim of this set of experiments is to observe the variation of optical properties as a function of Si-rich layer thickness. In this way the influence of QDs size and that of annealing conditions can be correlated.

For each thickness one sample was kept as-deposited and another one was annealed at 500 °C for 3 min in order to obtain a dehydrogenated film and use it in the QDs optical analysis. From now on, each sample will be called with a number referring to the thickness of its Si-rich layer. After annealing all samples were measured with Raman spectroscopy and their crystalline fraction was obtained. The results are reported in figure 4.28.

In figure 4.28 the three different plots correspond to the annealing durations. In each plot the crystallinity is shown as a function of the thickness  $d$  of the silicon-rich layer. The three different curves correspond to the annealing temperatures.

The crystallinity values of samples 2 and 3 show a strong dependence on annealing temperature and a weaker dependence on annealing time. For annealing at 980 °C, sample 2 shows a very low crystallinity of approximately 4%, meaning that crystallization had just started at that point. This happens independently of the annealing time. At 1000 °C and at 1020 °C its crystallinity increases considerably to 13 and 23.6 %, respectively, for 3 min annealing. For longer annealing times this increase becomes even more pronounced and a maximum of 29 % of crystallinity is reached.

Sample 3 shows to be dependent on annealing temperature as well, but not as strongly as sample 2. Even at 980 °C the nucleation phase is well started for each annealing time. For

a given annealing time, a higher temperature leads to an increase in crystallinity. For longer times this increase becomes less pronounced. The maximum crystallinity reached by sample 3 is approximately 29% for each temperature. As this maximum is not influenced by temperature, it may mean that sample 3 reached saturation. Samples 2 and 3 are comparable in terms of maximum crystallinity, but sample 2 presents a longer incubation time and a slower growth rate.

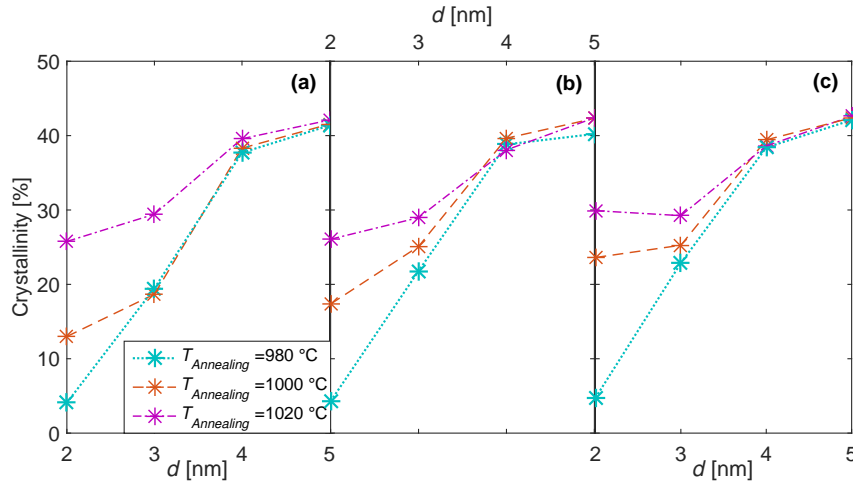


**Figure 4.28:** Crystallinity of samples with different thicknesses (2, 3, 4 and 5 nm) annealed in  $N_2$  at different temperatures (980, 1000 and 1020 °C) for (a) 3 min (b) 3.5 min (c) 4 min.

The results of samples 4 and 5 show to be comparable, both in terms of trend and crystallinity values. The latter are high, with respect to samples 2 and 3, and stable, independently of the annealing time and temperature. This was also observed in the previous section, where the incubation time of the samples was shown to be below 0.5 min. Crystallization seems to have reached saturation for both of them. The observed average crystallinity values for samples 4 and 5 are  $38.7 \pm 0.68\%$  and  $41.8 \pm 0.5\%$ , respectively.

The next step in the characterization of QDs properties as a function of their size is done by fitting the absorption measurements carried out using the PDS setup. The first parameter, shown in figure 4.29, is the integrated QD DOS.

This graph shows the  $I_{QD}$  for samples of different thicknesses, annealed at different temperatures and durations. Once again, the trends observed for crystallinity are reflected by  $I_{QD}$ . Sample 2 shows very low intensities, especially for low annealing temperatures. The value roughly doubles when going from 1000 °C to 1020 °C. The maximum value, reached for the combination of the highest temperature and longest time, is  $2.52 \times 10^{20} \text{ cm}^{-3}$ . So the QD DOS strongly increases with temperature but only slightly with time.

Sample 3 follows the same trend as sample 2. The biggest influence seems to be played by temperature and it is noticeable especially when passing from 1000 °C to 1020 °C. The maximum crystallinity corresponds to the maximum  $I_{QD}$ , which is  $3.18 \times 10^{20} \text{ cm}^{-3}$ .

Differently from what is observed in crystallinity, the maximum value reached by sample 3 differs from the maximum of sample 2 by a factor of 1.25. Again, samples 4 and 5 are independent of annealing temperature and time and always show quite stable values of  $I_{QD}$ . Their average integrated QD DOS values are  $4.4$  and  $5.69 \times 10^{20} \text{ cm}^{-3}$ , with standard deviations of  $11.6 \times 10^{18}$  and  $3.2 \times 10^{18} \text{ cm}^{-3}$ , respectively.

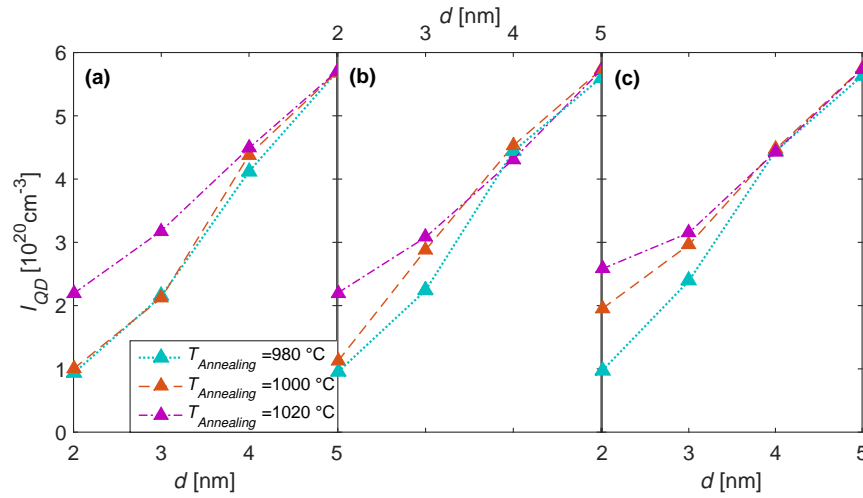


**Figure 4.29:** Integrated QD DOS of samples with different thicknesses (2, 3, 4 and 5 nm) annealed in  $\text{N}_2$  at different temperatures (980, 1000 and 1020  $^\circ\text{C}$ ) for (a) 3 min (b) 3.5 min (c) 4 min.

What is analyzed next is the trend of QDs energy band gap and it is shown in figure 4.30.

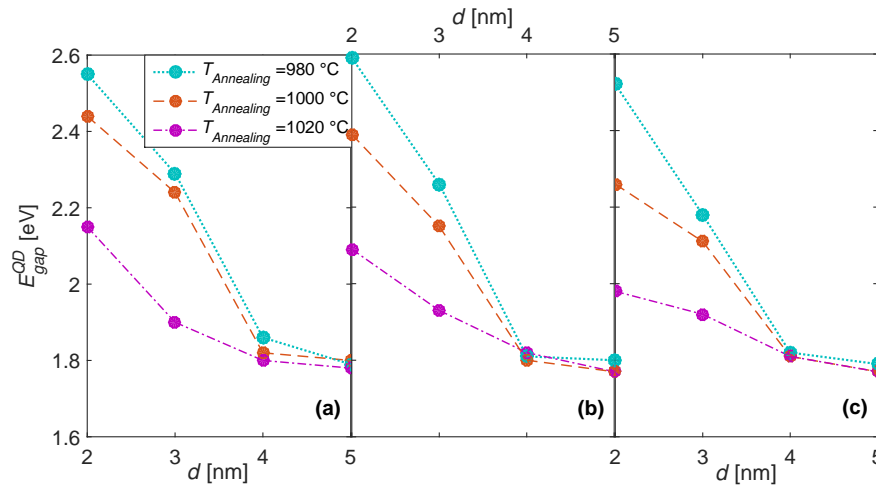


**Figure 4.30:** QD energy band gap of samples with different thicknesses (2, 3, 4 and 5 nm) annealed in  $\text{N}_2$  at different temperatures (980, 1000 and 1020  $^\circ\text{C}$ ) for (a) 3 min (b) 3.5 min (c) 4 min.

Also in this graph it is evident that samples 2 and 3, at least for the ranges we are investigating, are most affected by annealing time and temperature. In the first phase of crystallization, when the c-QDs are agglomerates of some tens of atoms, the QD allowed states are subjected to strong confinement and that is shown in the energy band gap value, which is significantly higher than after saturation is reached.  $E_{\text{gap}}^{QD}$  of sample 2 evolves from about 2.6 to 2 eV when the crystallinity varies from approximately 4 to 29 %.

Sample 3 follows an analogous trend, decreasing from about 2.3 to 1.9 eV.

Following the trend shown by crystallinity measurements, the energy band gaps of samples 4 and 5 are stable at a saturation value of  $1.82 \pm 0.009 \text{ eV}$  and  $1.77 \pm 0.015 \text{ eV}$ , respectively.

This shows that the mean QD size remains stable.

The standard deviation of the QD DOS distribution is shown in figure 4.31.

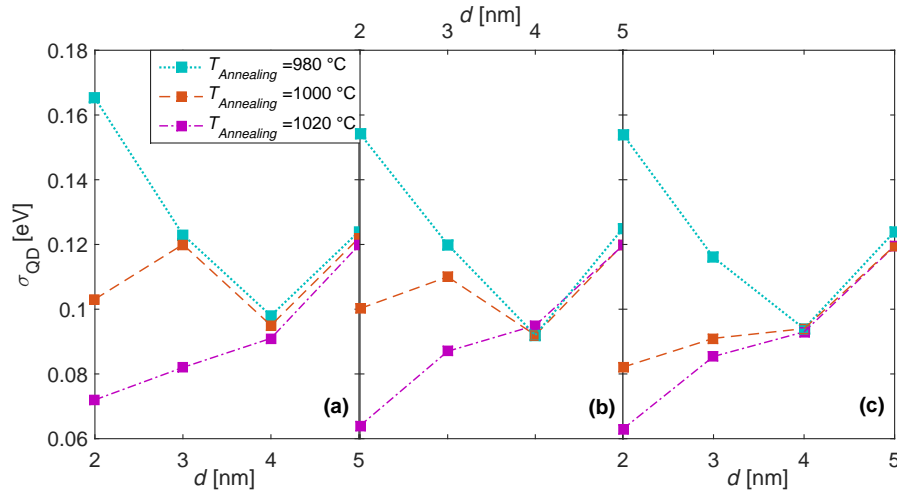


**Figure 4.31:** QD DOS standard deviation of samples with different thicknesses (2, 3, 4 and 5 nm) annealed in  $N_2$  at different temperatures (980, 1000 and 1020 °C) for (a) 3 min (b) 3.5 min (c) 4 min.

The three boxes correspond to increasing annealing time. Each line represents a temperature and shows the variation of QD DOS standard deviation as a function of the Si-rich layer thickness  $d$ .

Again, sample 2 and 3 are those which show to be most influenced by annealing conditions. As the annealing temperature and so their crystallinity increase, their  $\sigma_{QD}$  decreases proportionally. As the QDs grow bigger and occupy the whole width of the Si-rich layer, their size distribution becomes narrower.

Samples 4 and 5 show almost constant values of  $\sigma_{QD}$  at each annealing time and temperature. This is due to the fact that the crystallinity of these samples, for the annealing conditions we are considering, has already reached saturation.

In every graph of figure 4.30 a decrease in band gap with increasing size of the dots is clear. This is in full accordance with theory (see section 2.1.4). The opposite trend is visible, for the DOS standard deviation, in figure 4.31. A clearer representation of these trends is given in figure 4.32.

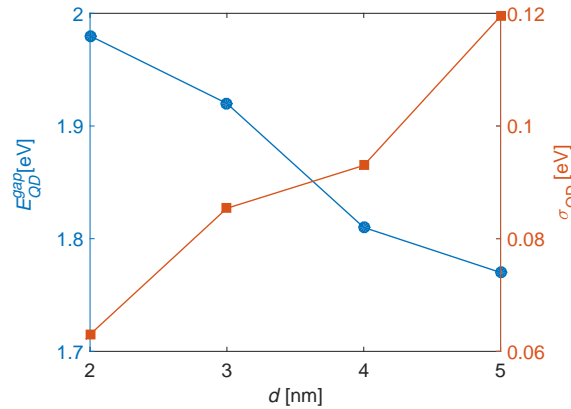


**Figure 4.32:** QD energy band gap and QD DOS standard deviation as a function of QD size (2, 3, 4 and 5 nm Si-rich layer thickness) annealed in  $N_2$  at  $1020^\circ C$  for 4 min.

In figure 4.32 the QDs energy band gap of samples with different Si-rich layer thicknesses is shown. For the purpose of showing the trend of QDs energy band gap and DOS standard deviation as a function of QD mean size, samples annealed at  $1020^\circ C$  for 4 min were chosen. This was done because, for these annealing conditions, sample 2 and 3 reached the highest crystallinity, meaning that these are the closest data point we have to saturation.

Analogously, in figure 4.33, the crystallinity and the integrated QDs DOS is represented as a function of the silicon rich layer thickness.

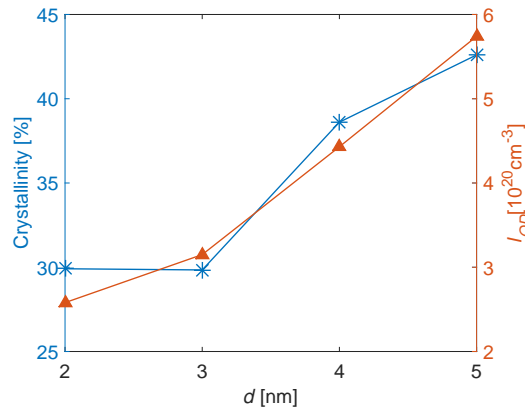


**Figure 4.33:** Crystallinity and integrated QD DOS as a function of QD size (2, 3, 4 and 5 nm Si-rich layer thickness) annealed in  $N_2$  at  $1020^\circ C$  for 4 min.

As the layer thickness increases, both the crystallinity and the integrated QDs DOS increase following an approximately linear trend.

Given all the trends found so far in the QD characterization as a function of their size, it is also interesting to investigate the correlations among these parameters. In figure 4.34 the QD energy band gap is represented as a function of the QD DOS standard deviation.

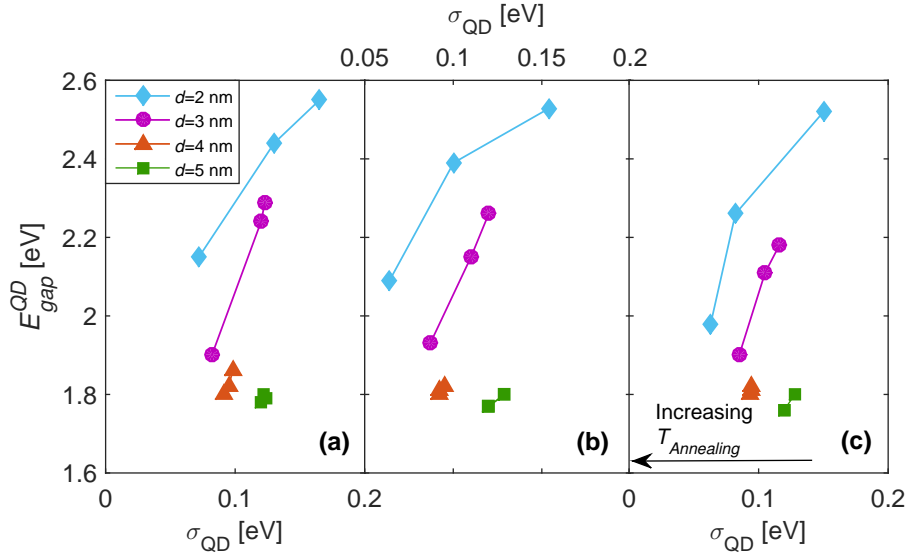


**Figure 4.34:**  $E_{gap}^{QD}$  as a function of  $\sigma_{QD}$  for samples with different Si-rich layer thicknesses (2, 3, 4 and 5 nm) annealed in  $N_2$  at different temperatures (980, 1000 and 1020 °C) for different durations (a) 3 min, (b) 3.5 min, (c) 4 min.

In figure 4.34, each box corresponds to a different annealing duration. Each curve represents a Si-rich layer thickness, as shown in the legend, and the black arrow shows the direction of increasing annealing temperature.

For decreasing  $\sigma_{QD}$  the QDs energy band gap decreases as well. This occurs, at each annealing time, for increasing annealing temperature. This trend is mostly visible for samples 2 and 3 which, as was also noticed from previous figures in this section, are the most affected by annealing time and temperature, at least for the ranges we consider in this experiment. Samples 4 and 5 show extremely small variations, within fitting error margin.

What can be evinced from this plot is that as the band gap decreases, so does the DOS standard deviation  $\sigma_{QD}$  indicating an increase in size uniformity upon crystallization. So, relatively to one Si-rich layer thickness, the larger the band gap, the wider the size distribution. On the other hand, when looking at all the Si-rich layer thicknesses, the larger the band gap, the narrower the size distribution. Extending this consideration to the QDs size, it can be concluded that the larger the QDs, the smaller their energy band gap and the larger their size dispersion.

Another correlation which is worth considering is that between the integrated QD DOS and its standard deviation, which is shown in figure 4.35. In this plot each curve corresponds to a Si-rich layer thickness. Here  $I_{QD}$  is shown as a function of  $\sigma_{QD}$  and both of them are expressed for increasing annealing temperature, as shown by the black arrow. Also in this case, the variations in both  $\sigma_{QD}$  and  $I_{QD}$  of samples 4 and 5 are very small.

The trend of  $I_{QD}$  reflects what was observed also in figure 4.34. When observing a single Si-rich layer thickness, the more the integrated QD states increase, the more the QDs grow in the film, and the more the size distribution becomes uniform. When considering all Si-rich layer thicknesses, to thicker layers correspond larger  $\sigma_{QD}$  and  $I_{QD}$ .

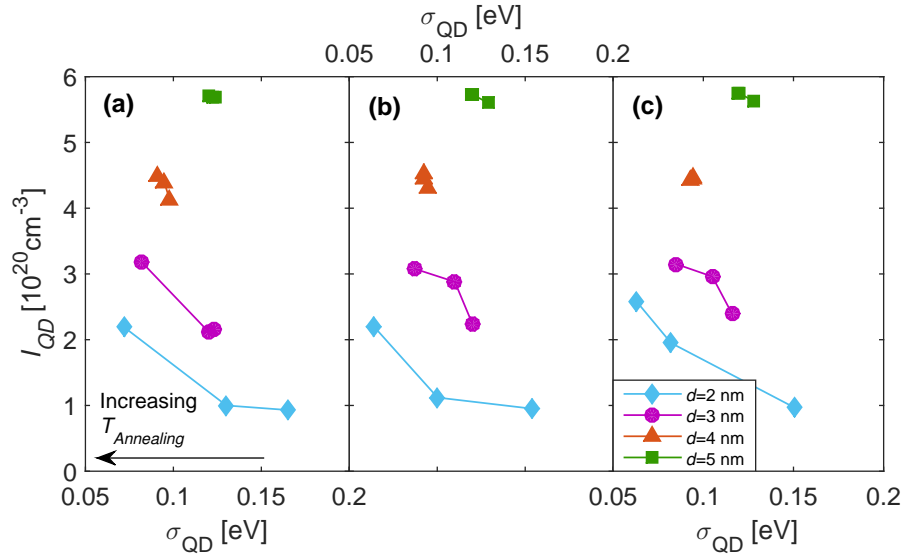


**Figure 4.35:**  $I_{QD}$  as a function of  $\sigma_{QD}$  of samples with different thicknesses (2, 3, 4 and 5 nm) annealed in  $N_2$  at different temperatures (980, 1000 and 1020 °C) for different durations (a) 3 min, (b) 3.5 min, (c) 4 min.

## Discussion

This last series of experiments was meant to investigate the relation between the Si-rich layer thickness, the QDs size and their properties. This was done by carrying out annealing at different temperatures and for different durations on samples of increasing Si-rich layer thickness (2, 3, 4 and 5 nm). In general, what is observed, is a strong dependence of crystallinity and other QDs parameters on the size of the QDs.

The crystallization of samples 2 and 3 is not only delayed with respect to the crystallization of samples 4 and 5, but it is also slower and the highest crystallinity they reach is almost 10% lower than that reached by 4 and 5.

This last consideration may not only depend on the Si-rich layer thickness of the samples, but also on the fact that the annealing time was not long enough to allow full crystallization of the film. In fact, the crystallinity of samples 2 and 3, at  $t_{Annealing}=4$  min was still increasing. The same considerations hold for the trends showed by the integrated QD DOS.

In general, to the maximum crystallinity of each sample corresponds the lowest  $\sigma_{QD}$ . So, for a given Si-rich layer thickness,  $\sigma_{QD}$  is strongly influenced by the stage crystallization reaches: the closer to saturation, the smaller the DOS standard deviation becomes, the more uniform the mean QD size. Observing  $\sigma_{QD}$  as a function of Si-rich layer thickness, two different trends are visible. At  $T_{Annealing}=980$  °C and for each annealing time, samples 2 and 3 show larger  $\sigma_{QD}$  than samples 4 and 5. This is due to the fact that for those annealing conditions, in samples 2 and 3 crystallization has just started (see figure 4.28), leading to a wide size distribution. On the other hand, samples 4 and 5 have already reached saturation of crystallinity and this means, from what was noticed from previous experiments, that they have also reached their minimum in size dispersion. At  $T_{Annealing}=1000$  °C and  $t_{Annealing}=3$  or 3.5 min the same happens. Things change for  $T_{Annealing}=1000$  °C and  $t_{Annealing}=4$  min, where a trend connected to Si-rich layer thickness becomes more pronounced. The larger the thickness, the larger  $\sigma_{QD}$  becomes. The same trend is visible at  $T_{Annealing}=1020$  °C for

each annealing time. This trend becomes visible only when the samples of all size become comparable in crystallinity. This implies that the size distribution relatively to one Si-rich thickness is close to its minimum. So, if we consider that for larger Si-rich layer thickness also the mean QD size increases, we can conclude that larger QDs show larger size dispersion.

This size-dependent effect on crystallinity is not surprising as it was already observed and reported by M. Zacharias et al. [12]. They fabricated a-Si/SiO<sub>2</sub> multilayer samples on Si wafers and varied the thickness of the Si layer from 1.9 to 20 nm. What they found was a strong effect of the Si layer thickness on the crystallization temperature.

According to their experiments, an increase of approximately 300 °C was noticed for a thickness of 3 nm, with respect to the crystallization temperature of the bulk material [12]. The relation between layer thickness and crystallization temperature was modeled as exponential, according to the empirical data (see figure 4.36). The crystallization behaviour can be described by [12]:

$$T_C = T_{ac} + (T_{melt} - T_{ac}) \exp\left(-\frac{d}{C}\right) \quad (4.7)$$

Where  $T_{melt}$  corresponds to the melting point of bulk crystalline material,  $T_{ac}$  expresses the crystallization temperature of a thick amorphous film of the material and  $d$  is the thickness of the amorphous film.  $C$  is a constant which was found to be independent of the material.

In our samples, the material used is not a-Si but a-SiO<sub>x</sub> and this, in general, leads to higher solid phase crystallization temperatures [12]. However, the trend noticed upon annealing is analogous. A further study should be carried out to verify whether the exponential nature of the phenomenon described by Zacharias et al. still applies.

For what concerns the characterization of QDs properties, the integrated QD DOS generally follows the trend observed for crystallinity. Assuming that the mean QDs size is determined by the Si-rich layer thickness it can be concluded that:

- The integrated QD DOS shows a clear increase for increasing Si-rich layer thickness, and so for increasing mean QD size, at each temperature and annealing time.
- The QDs energy band gap, especially when looking at samples annealed for the longest duration and the highest temperature, shows an evident decrease with increasing size.

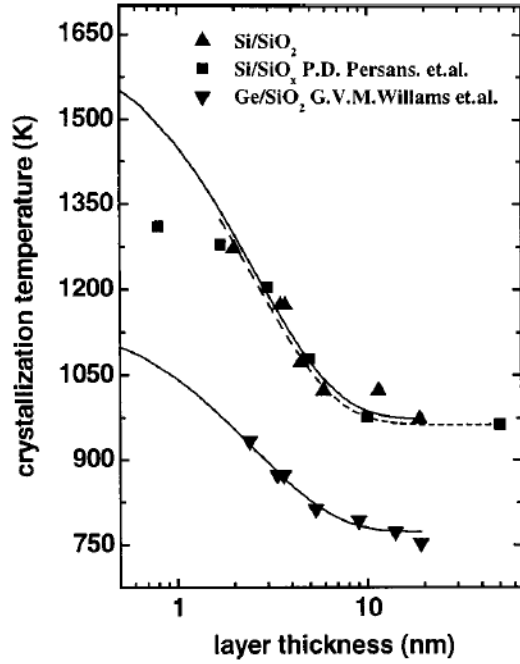


**Figure 4.36:** Si layer thickness dependent crystallization behaviour of Si/SiO<sub>2</sub> superlattices according to Zacharias et al. [12]. The solid line represents the trend described by equation 4.7.

- The same happens for the QDs size uniformity, which decreases for increasing crystallinity and increases for increasing size.

# Conclusions & Recommendations

In this thesis several series of experiments were carried out in order to determine the effect of the variation of relevant process parameters on the evolution of optical properties of c-Si QDs embedded in a silica matrix. This conclusive chapter is divided in two parts. The first section summarizes the results obtained from our experiments and presents the conclusions we were able to draw. The second section gives some suggestions about possible future work on this topic.

## 5.1 Conclusions

The conclusion we draw from this work can be listed, referring to each experiment we carried out, as:

- *Carbolite furnace*

The most important conclusion we were able to obtain from this series of experiments is that this furnace is not suitable for QDs fabrication. In fact, due to very high annealing temperature (between 900 and 1075 °C) even a small amount of oxygen in the annealing atmosphere is sufficient to cause a strong oxidation of the samples, which makes them unusable for further characterization.

However, from this series of experiments we were also able to show that, for our samples, hydrogen effusion starts at 400 °C and it is complete at 500 °C.

- *RTA furnace - Si-rich layer composition*

From this set of experiments it was found that an increasing silicon content (in our case up to 78 %) in the silicon rich layers leads to a lower defect density, both upon hydrogen effusion and upon crystallization. Moreover, the higher the silicon content, the higher the crystallinity and the integrated QD DOS. This is also visible in the values of energy band gap and DOS standard deviation, which decrease with increasing silicon content, indicating larger or denser and more uniform QDs.

- *RTA furnace - Annealing temperature*

By varying the annealing temperature a strong thermal dependence of crystallization and evolution of QDs was evinced. In the RTA furnace, with an annealing time of 3 min, the samples remained amorphous up to 940 °C, the crystallinity increased monotonously between 950 up to 1040 °C, the integrated QD DOS varied accordingly. Energy band gap and standard deviation decrease, showing an increase in size and in size uniformity.

- *RTA furnace - Annealing time*

Interestingly, what was observed for increasing annealing time greatly depends on the annealing environment. Samples treated in nitrogen gas showed, at each annealing temperature, trends in accordance with theory. An incubation time of 15-20 s is followed by a steep increase in crystallinity and then by a saturation plateau (between 30 and 35 %). The QDs properties extracted from absorption measurement are also in good agreement with crystallinity measurements and theory. The band gap decreases (from approximately 2.4 to 1.85 eV) and the QD DOS standard deviation varies accordingly (from about 0.16 to 0.08 eV). The integrated QD DOS follows the same trend as crystallinity. Also in this case it can be concluded that during crystallization the QDs grow in size and in size uniformity. In general, higher annealing temperatures led to shorter incubation time, higher crystallinity and narrower size distribution. The same trends were not observed for samples treated in forming gas. In this set of experiments the observed incubation time at each temperature is longer, between 0.5 and 1 min. After this first phase an increase in crystallinity is observed which continues until a maximum value is reached (between 28 and 33 %). Unexpectedly, after an annealing time of 3 to 3.5 min, the crystallinity decreases. This same trend is followed by the integrated QD DOS. Energy band gap and DOS standard deviation decrease from the beginning of crystallization up to 3 to 3.5 min. After this threshold time they both start increasing. From the former it can be concluded that the mean QDs size is decreasing. The increase of the latter indicates that not all the QDs are shrinking at the same rate. To explain this phenomenon two solutions are proposed and explained below. As the only difference between the two annealing procedures is the presence of hydrogen in the chamber, this is taken as a starting point:

- As described in section 4.2.4 the molecular hydrogen in the annealing chamber dissociates and, in its atomic form, diffuses through the film. When reaches the QDs interface it breaks Si-Si bonds and degrades the crystalline structure of the material. According to this explanation, the two phases (Si and SiO<sub>2</sub>) remain separate. An amorphous shell forms around the crystalline QDs, which consequently are reduced in size.

- In this second explanation, the participation of oxygen is involved in the diffusion process of hydrogen. Also in this case molecular hydrogen is split into its atomic form, according to what explained in section 4.2.4. H atoms are free to diffuse through the film and the so-called hydrogen enhanced oxygen diffusion occurs. After the QDs are formed, H atoms assist oxygen atoms in diffusing into the crystalline QDs by breaking Si-Si bonds. The transition layer between SiO<sub>2</sub> and c-Si broadens, while the c-Si QDs shrink. In this case oxygen is migrating back in the Si QDs, as a result the phase separation in the transition layer is no longer maintained.

The sub-gap absorption, in both samples annealed in forming gas and nitrogen gas, does

not show any thermal dependence. After crystallization no remarkable variation in its value is observed. However, the average value measured for samples annealed in forming gas is much lower than the average value measured for those annealed in nitrogen gas. More precisely the values for the annealing environments are  $736\text{ cm}^{-1}$  and  $1026\text{ cm}^{-1}$ , respectively.

A remarkable finding was also that, while in nitrogen gas complete dehydrogenation of the film is obtained in 3 min annealing, in forming gas the same result is obtained only after a twice as long treatment. This indicates that the kinetics of hydrogen effusion is slowed by the presence of hydrogen in the annealing environment.

- *RTA furnace - Si-rich layer thickness*

From this last series of experiments, a strong dependence of crystallization on the Si-rich layer thickness was found. The thinner the Si-rich layer the longer the incubation time and the lower the measured maximum crystallinity. However, for a given Si-rich layer thickness, the higher the annealing temperature, the shorter the incubation time and the higher the crystallinity. For thin samples (2 and 3 nm-thick Si-rich layer) it was noticed a decrease in DOS standard deviation and in QDs energy band gap as the crystallinity increased, in accordance with results from previous experiments. For the observed ranges of annealing durations and temperatures, the samples with thicker Si-rich layer (4 and 5 nm) have already reached saturation. For comparable crystallinity, some conclusions can be drawn on the characteristics of QDs as a function of Si-rich layer thickness. The thicker the layer, the larger the QDs' DOS standard deviation. This indicates that, at a stage in which a large portion of the QDs has reached its maximum size and so its minimum size dispersion, larger QDs show a broader size distribution. This is also confirmed by the QDs energy band gap, which decreases for increasing Si-rich layer thickness.

## 5.2 Recommendations

- In future experiments, avoid using a Carbolite furnace for long durations and high temperature annealing, in fact, it leads to the formation of a thick thermal oxide layer. This may happen either because some oxygen enters the chamber during the process, or because the nitrogen flow contains oxygen impurities, or because, when opening the chamber, some oxygen remains trapped in the porous lining of the chamber also after purging.
- The initial challenge we had to face during this work was the formation of QDs in our a-SiO<sub>x</sub>/SiO<sub>2</sub> multilayer samples, by means of high temperature annealing, avoiding oxidation of the top layer. For this purpose, the RTA furnace has proven to be an effective and quick tool. On the other hand, with a heating rate of 15 °C s<sup>-1</sup>, the film is subjected to an intense thermal stress, which enhances the defect generation and hinders the electrical properties of the material. In order to obtain higher quality films, in future experiments the annealing step could be carried out in a quartz tube furnace. This would mean lower heating rates and better prevention from oxygen contamination in the chamber.
- For what concerns the annealing in forming gas, some interesting results were repeatedly found, and two possible explanations were proposed. However, the phenomenon we observed was not extensively studied and may deserve more attention. In fact, annealing in forming gas led to a lower defect density in the material. A deeper insight on the kinetics of hydrogen diffusion in the layer may allow to benefit from the passivating effect of hydrogen without incurring the amorphization process we experienced. What it could be tried, for instance, is dividing the annealing procedure in two steps. The first could be done in forming gas, at low temperature, to obtain hydrogen effusion from the film. The second one, at high temperature, can be carried out in nitrogen gas atmosphere to reach crystallization of the samples .
- The series of experiments described in section 4.2.5 aimed to investigate the effect different annealing temperatures and durations have on samples with increasing Si-rich layer thickness. However, only limited ranges of time and temperature were tested, which gave us a limited insight on the evolution of the crystallization process. In future experiments, it would be interesting to repeat the annealing procedure for lower temperatures and for shorter annealing times. This would allow to better understand when and how the crystallization process of thick samples (4 and 5 nm-thick Si-rich) starts. An estimation could be given about their incubation time and about the QDs growth rate. Also experimenting longer annealing times could give interesting results. In fact, we do not know, from our experiments, if the thinner samples (2 and 3 nm-thick Si-rich) have already reached crystallinity saturation. This would allow to understand if thinner sample truly reach a lower crystallinity, or it is only because the crystallization, after 4 min is not complete yet. A broader picture would allow an estimation of the kinetics of this size-dependent phenomenon.

---

# Appendix A

---

## Appendix A

What we report here are experiments about hydrogen plasma passivation carried out by Martijn van Sebille at TU Delft.

Samples of PECVD-deposited  $\alpha\text{-Si}_{0.66}\text{O}_{0.33}$  were fabricated in the same batch. They were deposited in a monolayer configuration and their thickness was approximately 100 nm, in a second step they were laser annealed with a sufficient power fluence to obtain phase separation and silicon crystallization. The absorption coefficient was then measured and, at 1.5 eV, it was  $\alpha=2050\text{ cm}^{-1}$ . In a third step, each sample was exposed to a different plasma treatment, as shown in the figures below.

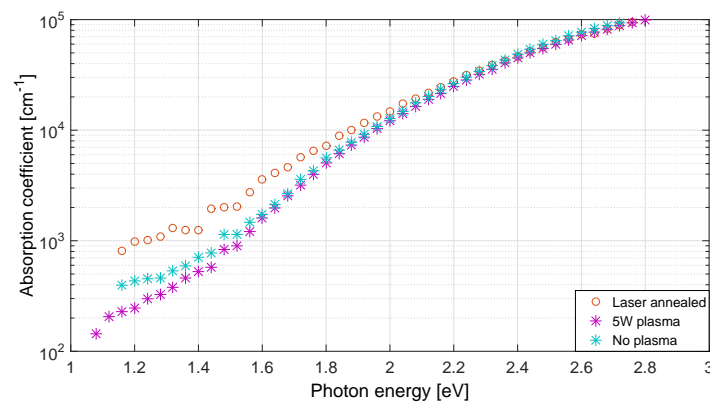


**Figure A.1:** Comparison of  $\alpha(\lambda)$  spectra of a laser annealed sample, a sample exposed to hydrogen plasma for 1 h, with a gas flow of 200 sccm, a temperature of 525 °C and an RF power of 5 W and a sample annealed in the same conditions but with no power.

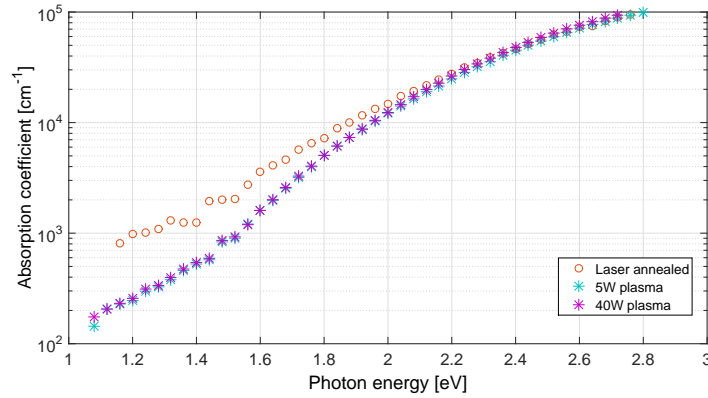


**Figure A.2:** Comparison of  $\alpha(\lambda)$  spectra of a laser annealed sample, a sample exposed to hydrogen plasma for 1 h, with a gas flow of 200 sccm, a temperature of 525 °C and an RF power of 5 W and a sample annealed in the same conditions but with an RF power of 40 W.

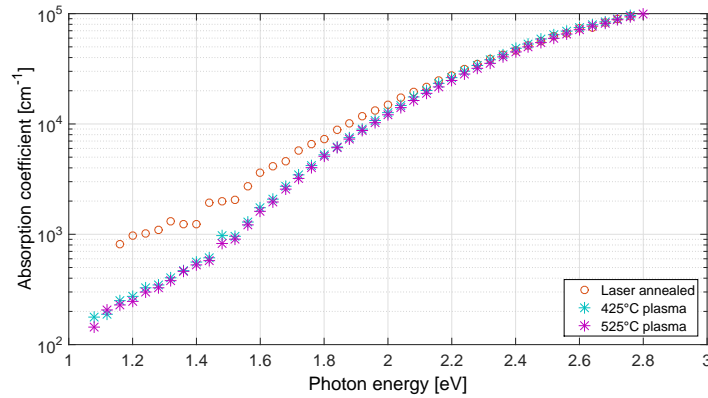


**Figure A.3:** Comparison of  $\alpha(\lambda)$  spectra of a laser annealed sample, a sample exposed to hydrogen plasma for 1 h, with a gas flow of 200 sccm, a temperature of 525 °C and an RF power of 5 W and a sample annealed in the same conditions but at a temperature of 425 °C .

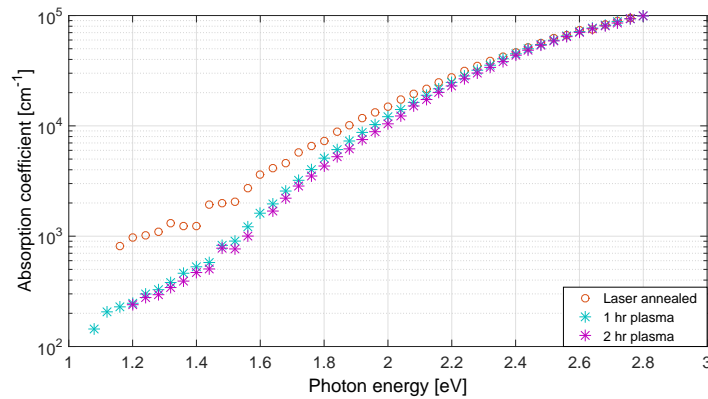


**Figure A.4:** Comparison of  $\alpha(\lambda)$  spectra of a laser annealed sample, a sample exposed to hydrogen plasma for 1 h, with a gas flow of 200 sccm, a temperature of 525 °C and an RF power of 5 W and a sample annealed in the same conditions but for an annealing time of 2 h.

---

# Appendix B

---

## Appendix B

### B.1 PDS measurement fitting procedure

The PDS measurement fitting procedure was carried out in the four steps listed below:

- *Fitting of absorbance  $A$* 

The first script is used to manually fit the measurement obtained for the absorbance  $A$  to  $1-R-T$ . This is of particular use in the near infra-red region, where the absorbance is almost zero, and its measurement becomes less accurate. The script `TRA2.m` takes as input the raw data and gives as an output:

  - A file with the corrected (interference fringes free) values of  $T$ ,  $R$ ,  $A$ ;
  - The correction coefficients of  $T$ ,  $R$  and  $A$  together with the MSE of the fit;
- *Calculation of absorption coefficient  $\alpha(\lambda)$* 

A second script `RW2.m` is used to calculate the absorption coefficient  $\alpha = \alpha(\lambda)$  of the sample as a function of the incident wavelength. It is obtained from the interference-free  $A/T$  spectra using the Ritter-Weisser formula. It takes as an input:

  - The corrected values of  $T$ ,  $R$  and  $A$  obtained from `TRA2.m`
  - The thickness and the roughness of the sample obtained from SE measurements
  - The refractive index  $n(\lambda)$  of the sample obtained from SE measurements
  - The refractive index of the substrate and a smoothing coefficient

It gives as an output a plot and a file containing the absorption coefficient.

- *Extraction of optical properties from  $\alpha(\lambda)$* : as deposited a-SiO<sub>x</sub>:H  
`fitAlphaGUI.m` takes as inputs all the parameters needed, according to the model described in 3.2.3, to generate a DOS. Based on the generated DOS, it calculates an  $\alpha(\lambda)$  spectrum according to 3.13. Then, it tries to fit this spectrum and the spectrum obtained through the procedure described in the previous steps. After this first fit the

script suggests new values of the above mentioned parameters, in order to improve the quality of the fit. The process is therefore iterative, and it was repeated until the MSE was sufficiently low ( $<0.02$ ) The output consists in the set of fit parameters which describes the DOS of the a-SiO<sub>x</sub>.

- *Extraction of optical properties from  $\alpha(\lambda)$ : c-Si QDs*  
`fitAlphaGUIQD.m` works similarly to the script described for the analysis of the a-SiO<sub>x</sub> matrix. As inputs parameters are needed, additionally, the characteristics of the embedded QDs, as described in 3.2.3. The output of the script consists in a set of parameters describing the QD'DOS characteristics.

---

# Bibliography

- [1] M. van Seville, R. Vasudevan, R. Lancee, R. van Swaaij, and M. Zeman, "Optical characterization and density of states determination of silicon nanocrystals embedded in amorphous silicon based matrix," *Journal of Physics D: Applied Physics*, vol. 48, no. 32, 2015.
- [2] IEA, "Technology Roadmap," tech. rep., International Energy Agency, IEA2013.
- [3] G. Conibeer, "Third-generation photovoltaics," *Mater. Today*, 2007.
- [4] Syllabus5, *Solar Cells*, ch. Solar Cell Conversion-Efficiency Limits. Open Course Ware - TU Delft, 2013.
- [5] M. Green, E. Cho, Y. Cho, E. Pink, T. Trupke, K. Lin, T. Fangsuwannarak, T. Puzzer, G. Conibeer, and R. Corkish, "All-silicon tandem cells based on "artificial" semiconductor synthesised using silicon quantum dots in a dielectric matrix," in *20th European Photovoltaic Solar Energy Conference*, pp. 6–10, 2005.
- [6] C. de Mello Donega, "Synthesis and properties of colloidal heteronanocrystals," *Chemical Society Reviews*, vol. 40, no. 3, pp. 1512–1546, 2011.
- [7] I.-C. Chen, P.-Y. Lin, T. T. Li, and J.-Y. Chang, "Kinetic study of the thermal crystallization behavior of hydrogenated amorphous silicon prepared by ECRCVD," *ECS Journal of Solid State Science and Technology*, vol. 3, no. 5, 2014.
- [8] *Solar Cells*, ch. Thin-film silicon solar cells, pp. 1–30. Open Course Ware - TU Delft, 2013.
- [9] H. Neitzert, N. Layadi, P. R. I Cabarrocas, R. Vanderhaghen, and M. Kunst, "In situ measurements of changes in the structure and in the excess charge carrier kinetics at the silicon surface during hydrogen and helium plasma exposure," *Journal of Applied Physics*, vol. 78, no. 3, pp. 1438–1445, 1995.
- [10] R. Capaz, L. Assali, L. Kimerling, K. Cho, and J. Joannopoulos, "Mechanism for hydrogen enhanced oxygen diffusion in silicon," *Physical Review B*, vol. 59, no. 7, 1999.

- [11] G. Lucovsky, "Atomic structure and thermal stability of silicon suboxides in bulk thin films and in transition regions at Si/SiO<sub>2</sub> interfaces," *Journal of non-crystalline solids*, vol. 227, pp. 1–14, 1998.
- [12] M. Zacharias and P. Streitenberger, "Crystallization of amorphous superlattices in the limit of ultrathin films with oxide interfaces," *Physical Review B*, vol. 62, no. 12, pp. 83–91, 2000.
- [13] R. E. Smalley, "Grand challenges," 2010. Available: <http://cnst.rice.edu/content.aspx?id=246>, [Accessed 05 August 2015].
- [14] IEA, "Special Report: World Energy Investment Outlook," tech. rep., International Energy Agency, 2014.
- [15] BP, "Bp statistical review of world energy june 2014 about this review," tech. rep., 2014.
- [16] United Nations, "World population to 2300," 2012. Available: <http://www.un.org/esa/population/publications/longrange2/WorldPop2300final.pdf>, [Accessed 20 July 2015].
- [17] *Solar Cells*, ch. Introduction to photovoltaic solar energy, pp. 1–13. Open Course Ware - TU Delft, 2013.
- [18] M. Zerta, P. R. Schmidt, C. Stiller, and L. H., "Alternative world energy outlook (aweo) and the role of hydrogen in a changing energy landscape," *International Journal of Hydrogen Energy*, 2008.
- [19] N. Gronewold, "One-quarter of world's population lacks electricity," 2009. Available: [www.scientificamerican.com](http://www.scientificamerican.com), [Accessed 20 July 2015].
- [20] "International Energy Outlook 2013," tech. rep., U.S. Energy Information Administration, 2013.
- [21] V. K. Singh and L. Giribabu, "Photovoltaic-A Review of the Solar Cell Generation," *Innov. Electron. Commun.*, 2013.
- [22] M. A. Green, K. Emery, Y. Hishikawa, W. Warta, and E. D. Dunlop, "Solar cell efficiency tables (version44)," *Prog. Photovoltaics Res. Appl.*, 2014.
- [23] National Renewable Energy Laboratory, "Best Research-Cell Efficiencies," 2014.
- [24] G. Conibeer, M. Green, E.-C. Cho, D. Konig, Y.-H. Cho, T. Fangsuwannarak, G. Scardera, E. Pink, Y. Huang, and T. Puzzer, "Silicon quantum dot nanostructures for tandem photovoltaic cells," *Thin Solid Films*, vol. 516, no. 20, pp. 6748–6756, 2008.
- [25] X. Chen and P. Yang, "Preparation and photovoltaic properties of silicon quantum dots embedded in a dielectric matrix: a review," *Journal of Materials Science*, 2015.
- [26] Z. Wan, S. Huang, M. A. Green, and G. Conibeer, "Rapid thermal annealing and crystallization mechanisms study of silicon nanocrystal in silicon carbide matrix," *Nano Res Lett*, vol. 6, 2011.

- 
- [27] D. Hiller, S. Gutsch, A. M. Hartel, P. Löper, T. Gebel, and M. Zacharias, “A low thermal impact annealing process for SiO<sub>2</sub>-embedded si nanocrystals with optimized interface quality,” *Journal of Applied Physics*, vol. 115, no. 13, 2014.
- [28] C. Summonte, M. Allegranza, M. Bellettato, F. Liscio, M. Canino, A. Desalvo, J. López-Vidrier, S. Hernandez, L. López-Conesa, and E. S, “Silicon nanocrystals in carbide matrix,” *Solar Energy Materials and Solar Cells*, vol. 128, pp. 138–149, 2014.
- [29] X. Wang, J. Zhang, L. Ding, B. Cheng, W. Ge, J. Yu, and Q. Wang, “Origin and evolution of photoluminescence from Si nanocrystals embedded in a SiO<sub>2</sub> matrix,” *Physical Review B*, vol. 72, no. 19, 2005.
- [30] R. Ha, S. Kim, H. J. Kim, J. C. Lee, J.-S. Bae, and Y. Kim, “Crystallization behavior of silicon quantum dots in a silicon nitride matrix,” *Journal of nanoscience and nanotechnology*, vol. 12, no. 2, pp. 1448–1452, 2012.
- [31] M. Künle, T. Kaltenbach, P. Löper, A. Hartel, S. Janz, O. Eibl, and K.-G. Nickel, “Si-rich a-SiC:H thin films: structural and optical transformations during thermal annealing,” *Thin Solid Films*, vol. 519, no. 1, pp. 151–157, 2010.
- [32] J. Huang, Y. Zeng, W. Wang, Y. Yang, J. Huang, R. Tan, S. Dai, N. Dai, and W. Song, “Reduction of residual stress in SiO<sub>2</sub>-matrix silicon nano-crystal thin films by a combination of rapid thermal annealing and tube-furnace annealing,” *Physica Status Solidi (a)*, vol. 210, no. 3, pp. 528–532, 2013.
- [33] D. E. Ylmaz, C. Bulutay, and T. Çagin, “Analysis of strain fields in silicon nanocrystals,” *Applied Physics Letters*, vol. 94, no. 19, 2009.
- [34] M. Zacharias, J. Heitmann, R. Scholz, U. Kahler, M. Schmidt, and J. Blösing, “Size-controlled highly luminescent silicon nanocrystals: A SiO/SiO<sub>2</sub> superlattice approach,” *Applied Physics letters*, vol. 80, no. 4, pp. 661–663, 2002.
- [35] D. Basa, G. Ambrosone, and U. Coscia, “Microcrystalline to nanocrystalline silicon phase transition in hydrogenated silicon-carbon alloy films,” *Nanotechnology*, vol. 19, no. 41, 2008.
- [36] S. H. Hong, Y. S. Kim, W. Lee, Y. H. Kim, J. Y. Song, J. S. Jang, J. H. Park, S.-H. Choi, and K. J. Kim, “Active doping of b in silicon nanostructures and development of a si quantum dot solar cell,” *Nanotechnology*, vol. 22, no. 42, 2011.
- [37] E.-C. Cho, S. Park, X. Hao, D. Song, G. Conibeer, S.-C. Park, and M. A. Green, “Silicon quantum dot/crystalline silicon solar cells,” *Nanotechnology*, vol. 19, no. 24, 2008.
- [38] S. Yamada, Y. Kurokawa, S. Miyajima, and M. Konagai, “Silicon quantum dot superlattice solar cell structure including silicon nanocrystals in a photogeneration layer,” *Nanoscale research letters*, vol. 9, no. 1, pp. 1–7, 2014.
- [39] D. Song, E.-C. Cho, G. Conibeer, C. Flynn, Y. Huang, and M. A. Green, “Structural, electrical and photovoltaic characterization of Si nanocrystals embedded SiC matrix and Si nanocrystals/c-Si heterojunction devices,” *Solar Energy Materials and Solar Cells*, vol. 92, no. 4, pp. 474–481, 2008.

- [40] D. A. Neamen and B. Pevzner, *Semiconductor physics and devices: basic principles*, vol. 3. McGraw-Hill New York, 2003.
- [41] S. Park, E. Cho, X. Hao, G. Cornibeer, and M. Green, "Study of silicon quantum dot p-n or p-i-n junction devices on c-Si substrate," *Optoelectronic and Microelectronic Materials and Devices*, 2008.
- [42] E. Cho, M. Green, G. Conibeer, D. Song, Y. Cho, G. Scardera, S. Huang, S. Park, X. Hao, and Y. Huang, "Silicon quantum dots in a dielectric matrix for all-silicon tandem solar cells," *Opto Electronics*, vol. 2007, 2007.
- [43] E. G. Barbagiovanni, D. J. Lockwood, P. J. Simpson, and L. V. Goncharova, "Quantum confinement in Si and Ge nanostructures," *Journal of Applied Physics*, vol. 111, no. 3, 2012.
- [44] Y. Wakayama, T. Inokuma, and S. Hasegawa, "Nanoscale structural investigation of Si crystallites grown from silicon suboxide films by thermal annealing," *Journal of Crystal Growth*, vol. 183, no. 1, pp. 124–130, 1998.
- [45] M. V. Sopinsky, N. A. Vlasenko, I. P. Lisovskyy, S. O. Zlobin, Z. F. Tsybrii, and L. I. Veligura, "Formation of Nanocomposites by Oxidizing Annealing of  $\text{SiO}_x$  and  $\text{SiO}_x < \text{Er, F} >$  Films: Ellipsometry and FTIR analysis," *Nanoscale Research Letters*, vol. 10, no. 1, pp. 1–8, 2015.
- [46] B. Hinds, F. Wang, D. Wolfe, C. Hinkle, and G. Lucovsky, "Study of  $\text{SiO}_x$  decomposition kinetics and formation of Si nanocrystals in an  $\text{SiO}_2$  matrix," *Journal of non-crystalline solids*, vol. 227, pp. 507–512, 1998.
- [47] A. Sarikov, V. Litovchenko, I. Lisovskyy, I. Maidanchuk, and S. Zlobin, "Role of oxygen migration in the kinetics of the phase separation of nonstoichiometric silicon oxide films during high-temperature annealing," *Applied Physics Letters*, vol. 91, no. 13, pp. 133109–133109, 2007.
- [48] R. Iverson and R. Reif, "Recrystallization of amorphized polycrystalline silicon films on  $\text{SiO}_2$ : Temperature dependence of the crystallization parameters," *Journal of Applied Physics*, vol. 62, no. 5, pp. 1675–1681, 1987.
- [49] U. N. Nakajima, Kazuo and, *Crystal Growth of Silicon for Solar Cells*. Springer Science & Business Media, 2010.
- [50] K. Ding, U. Aeberhard, W. Beyer, O. Astakhov, F. Köhler, U. Breuer, F. Finger, R. Carius, and U. Rau, "Annealing induced defects in SiC,  $\text{SiO}_x$  single layers, and SiC/ $\text{SiO}_x$  hetero - superlattices," *Physica Status Solidi (a)*, vol. 209, no. 10, pp. 1960–1964, 2012.
- [51] K. Ding, U. Aeberhard, O. Astakhov, U. Breuer, M. Beigmohamadi, S. Suckow, B. Berghoff, W. Beyer, F. Finger, and R. Carius, "Defect passivation by hydrogen reincorporation for silicon quantum dots in SiC/ $\text{SiO}_x$  hetero-superlattice," *Journal of Non-Crystalline Solids*, vol. 358, no. 17, pp. 2145–2149, 2012.
- [52] Polymer Reaction Engineering Laboratory Chemical and Biomolecular Engineering University of Maryland, *STANDARD OPERATING PROCEDURES (Standard Wafer Cleaning Procedure)*, April 2009.

- 
- [53] K.-H. Kim, *Hydrogenated polymorphous silicon: establishing the link between hydrogen microstructure and irreversible solar cell kinetics during light soaking*. PhD thesis, 2012.
- [54] G. B. Tong, M. R. Muhamad, and S. A. Rahman, "Effects of RF power on structural properties of nc-Si: H thin films deposited by layer-by-layer (LbL) deposition technique," *Sains Malaysiana*, vol. 41, no. 8, pp. 993–1000, 2012.
- [55] E. Johnson, L. Kroely, and P. R. i Cabarrocas, "Raman scattering analysis of SiH bond stretching modes in hydrogenated microcrystalline silicon for use in thin-film photovoltaics," *Solar Energy Materials and Solar Cells*, vol. 93, no. 10, pp. 1904–1906, 2009.
- [56] "Solaris 100 - Rapid thermal annealing." Available: <http://ssi-rtp.com/page/products/rtp-solaris-75/>, [Accessed 25 May 2015].
- [57] J. Krc, *Optical modeling and simulation of thin-film photovoltaic devices*. Crc Press, 2013.
- [58] H. Tompkins, "Handbook of ellipsometry (materials science and process technology)," 2006.
- [59] J. Price, P. Hung, T. Rhoad, B. Foran, and A. Diebold, "Spectroscopic ellipsometry characterization of  $\text{Hf}_x\text{Si}_y\text{O}_z$  films using the Cody-Lorentz parameterized model," *Applied physics letters*, vol. 85, no. 10, pp. 1701–1703, 2004.
- [60] E. Smith and G. Dent, *Modern Raman spectroscopy: a practical approach*. John Wiley & Sons, 2013.
- [61] "Raman spectroscopy." Available: <http://www.ine.uh.edu/research/spectroscopy/>, [Accessed 18 May 2015].
- [62] M. de Grunt, "Raman spectroscopy of silicon quantum dots embedded in a silicon carbide matrix," Master's thesis, Delft University of Technology, 2013.
- [63] "Photothermal deflection spectroscopy tool," January 2014. Available: <http://www.nrel.gov/pv/pdil>, [Accessed 19 May 2015].
- [64] Z. Remes, R. Vasudevan, K. Jarolimek, A. H. Smets, and M. Zeman, "The optical spectra of a-Si:H and a-SiC:H thin films measured by the absolute photothermal deflection spectroscopy (PDS)," *Solid State Phenomena*, vol. 213, pp. 19–28, 2014.
- [65] S. Ilahi, F. Saidi, R. Hamila, N. Yacoubi, L. Auvray, and H. Maaref, "Photothermal deflection spectroscopy PDS investigation of optical and thermal properties of BGaAs/-GaAs alloys," *Current Applied Physics*, vol. 13, no. 3, pp. 610–613, 2013.
- [66] J. Poortmans and V. Arkhipov, *Thin film solar cells: fabrication, characterization and applications*, vol. 5. John Wiley & Sons, 2006.
- [67] L. Yi, J. Heitmann, R. Scholz, and M. Zacharias, "Si rings, Si clusters, and Si nanocrystals - different states of ultrathin  $\text{SiO}_x$  layers," *Applied Physics Letters*, vol. 81, no. 22, pp. 4248–4250, 2002.

- [68] L. Ramos, H. C. Weissker, J. Furthmüller, and F. Bechstedt, “Optical properties of Si and Ge nanocrystals: Parameter-free calculations,” *Physica Status Solidi*, vol. 242, no. 15, pp. 3053–3063, 2005.
- [69] “What is XPS? analysis of surfaces and thin films,” 2013. Available: <http://xpssimplified.com/whatisxps.php>, [Accessed 10 June 2015].
- [70] V. Volodin and D. Koshelev, “Quantitative analysis of hydrogen in amorphous silicon using Raman scattering spectroscopy,” *Journal of Raman Spectroscopy*, vol. 44, no. 12, pp. 1760–1764, 2013.
- [71] R. Ruther and J. Livingstone, “Hydrogenated amorphous silicon: Hydrogen content, bonding configurations and morphology in sputter-deposited, in-chamber annealed thin films,” *Thin Solid Films*, vol. 251, no. 1, pp. 30–35, 1994.
- [72] L. Tsybeskov, K. Hirschman, S. Duttagupta, P. Fauchet, M. Zacharias, J. McCaffrey, and D. Lockwood, “Fabrication of nanocrystalline silicon superlattices by controlled thermal recrystallization,” *Physica Status Solidi (a)*, vol. 165, no. 1, pp. 69–77, 1998.
- [73] H. Miyashita and Y. Watabe, “Flatband voltage shift of amorphous silicon nitride metal-insulator-semiconductor diodes,” *Journal of Applied Physics*, vol. 70, no. 4, pp. 2452–2454, 1991.
- [74] “Computational Chemistry Comparison and Benchmark DataBase,” 2013. Available: <http://cccbdb.nist.gov/>, [Accessed 21 May 2015].
- [75] J. Weber, “Defect generation during plasma treatment of semiconductors,” *Physica B: Condensed Matter*, vol. 170, no. 1, pp. 201–217, 1991.
- [76] J. W. Mandeep Singh and M. Konuma, “Evidence for intrinsic point defect generation during hydrogen-plasma treatment of silicon,” *Hydrogen in Semiconductors*, vol. 170, pp. 218–222, 2012.
- [77] W. Magro, D. Ceperley, C. Pierleoni, and B. Bernu, “Molecular dissociation in hot, dense hydrogen,” *Physical Review Letters*, vol. 76, no. 8, 1996.
- [78] J. I. Pankove and N. M. Johnson, *Hydrogen in Semiconductors: Hydrogen in Silicon Volume 34*, vol. 34. Academic Press, 1991.
- [79] B. Sopori, M. Symko, R. Reedy, K. Jones, and R. Matson, “Mechanism (s) of hydrogen diffusion in silicon solar cells during forming gas anneal,” in *Photovoltaic Specialists Conference, 1997., Conference Record of the Twenty-Sixth IEEE*, pp. 25–30, IEEE, 1997.
- [80] S. Estreicher, J. Hastings, and P. Fedders, “Defect-induced dissociation of H<sub>2</sub> in silicon,” *Physical Review B*, vol. 57, no. 20, 1998.
- [81] L. Cai and A. Rohatgi, “Effect of post-pecvd photo-assisted anneal on multicrystalline silicon solar cells,” *Electronic Devices*, 1997.
- [82] *Introduction to Microfabrication*, ch. Vacuum and plasmas, pp. 321–328.
- [83] R. Street, C. Tsai, J. Kakalios, and W. Jackson, “Hydrogen diffusion in amorphous silicon,” *Philosophical Magazine B*, vol. 56, no. 3, pp. 305–320, 1987.

- [84] R. Murray, "Hydrogen enhanced oxygen diffusion," *Physica B: Condensed Matter*, vol. 170, no. 1, pp. 115–123, 1991.
- [85] J. Valentaa and S. Mirabellab, "Introduction to Photovoltaics and Potential Applications of Group IV Nanostructures," *Nanotechnology and Photovoltaic Devices: Light Energy Harvesting with Group IV Nanostructures*, 2015.